ADVANCED STEEL CONSTRUCTION

An International Journal

Volume 14 Number 1

March 2018

CONTENTS

Technical Papers

Website: *http://www.hkisc.org*
ISSN 1816-112X
Science Citation Index Expanded, Materials Science Citation Index and ISI Alerting

Cover: The MGM Mansion Roof in Macau

e-copy of IJASC is free to download at "www.ascjournal.com" in internet and mobile apps.

ADVANCED STEEL CONSTRUCTION

VOL.14, NO.1 (2018)

ADVANCED STEEL CONSTRUCTION

an International Journal

ISSN 1816-112X

Volume 14 Number 1 *March 2018*

ADVANCED STEEL CONSTRUCTION
an international journal

Advanced Steel Construction
an international journal

ISSN 1816-112X

Science Citation Index Expanded, Materials Science Citation Index and ISI Alerting

Cover: MGM Mansion Roof in Macau

e-copy of IJASC is free to download at "www.ascjournal.com" in internet and mobile apps.

General Information
Advanced Steel Construction, an international journal

Aims and scope

The International Journal of Advanced Steel Construction provides a platform for the publication and rapid dissemination of original and up-to-date research and technological developments in steel construction, design and analysis. Scope of research papers published in this journal includes but is not limited to theoretical and experimental research on elements, assemblages, systems, material, design philosophy and codification, standards, fabrication, projects of innovative nature and computer techniques. The journal is specifically tailored to channel the exchange of technological know-how between researchers and practitioners. Contributions from all aspects related to the recent developments of advanced steel construction are welcome.

Instructions to authors

Submission of the manuscript. Authors may submit on-line at **www.hkisc.org**

Asian Pacific , African and organizing editor :	Professor S.L. Chan, Email: ceslchan@polyu.edu.hk
American editor :	Professor W.F. Chen, Email: waifah@hawaii.edu
European editor :	Professor R. Zandonini, Email: riccardo_zandonini@ing.unitn.it

All manuscripts submitted to the journal are recommended to accompany with a list of four potential reviewers suggested by the author(s). This list should include the complete name, address, telephone and fax numbers, email address, and at least five keywords that identify the expertise of each reviewer. This scheme will improve the process of review.

Style of manuscript

General. Author(s) should provide full postal and email addresses and fax number for correspondence. The manuscript including abstract, keywords, references, figures and tables should be in English with pages numbered and typed with double line spacing on single side of A4 or letter-sized paper. The front page of the article should contain:

a) a short title (reflecting the content of the paper);
b) all the name(s) and postal and email addresses of author(s) specifying the author to whom correspondence and proofs should be sent;
c) an abstract of 100-200 words; and
d) 5 to 8 keywords.

The paper must contain an introduction and a conclusion. The length of paper should not exceed 25 journal pages (approximately 15,000 words equivalents).

Tables and figures. Tables and figures including photographs should be typed, numbered consecutively in Arabic numerals and with short titles. They should be referred in the text as Figure 1, Table 2, etc. Originally drawn figures and photographs should be provided in a form suitable for photographic reproduction and reduction in the journal.

Mathematical expressions and units. The Systeme Internationale (SI) should be followed whenever possible. The numbers identifying the displayed mathematical expression should be referred to in the text as Eq. 1, Eq. 2.

References. References to published literature should be referred in the text, in the order of citation with Arabic numerals, by the last name(s) of the author(s) (e.g. Zandonini and Zanon [3]) or if more than three authors (e.g. Zandonini et al. [4]). References should be in English with occasional allowance of 1-2 exceptional references in local languages and reflect the current state-of-technology. Journal titles should be abbreviated in the style of the Word List of Scientific Periodicals. References should be cited in the following style [1, 2, 3].

Journal: [1] Chen, W.F. and Kishi, N., "Semi-rigid Steel Beam-to-column Connections, Data Base and Modelling", Journal of Structural Engineering, ASCE, 1989, Vol. 115, No. 1, pp. 105-119.

Book: [2] Chan, S.L. and Chui, P.P.T., "Non-linear Static and Cyclic Analysis of Semi-rigid Steel Frames", Elsevier Science, 2000.

Proceedings: [3] Zandonini, R. and Zanon, P., "Experimental Analysis of Steel Beams with Semi-rigid Joints", Proceedings of International Conference on Advances in Steel Structures, Hong Kong, 1996, Vol. 1, pp. 356-364.

Proofs. Proof will be sent to the corresponding author to correct any typesetting errors. Alternations to the original manuscript at this stage will not be accepted. Proofs should be returned within 48 hours of receipt on-line.

Copyright. Submission of an article to "Advanced Steel Construction" implies that it presents the original and unpublished work, and not under consideration for publication nor published elsewhere. On acceptance of a manuscript submitted, the copyright thereof is transferred to the publisher by the Transfer of Copyright Agreement and upon the acceptance of publication for the papers, the corresponding author must sign the form for Transfer of Copyright.

Permission. Quoting from this journal is granted provided that the customary acknowledgement is given to the source.

Page charge and Reprints. There will be no page charges if the length of paper is within the limit of 25 journal pages. A total of 30 free offprints will be supplied free of charge to the corresponding author. Purchasing orders for additional offprints can be made on order forms which will be sent to the authors. These instructions can be obtained at the Hong Kong Institute of Steel Construction, Journal website: http://www.hkisc.org

The International Journal of Advanced Steel Construction is published quarterly by learnt society, The Hong Kong Institute of Steel Construction, c/o Department of Civil & Environmental Engineering, The Hong Kong Polytechnic University, Hung Hom, Kowloon, Hong Kong.

Subscription inquiries and change of address. Address all subscription inquiries and correspondence to Member Records, IJASC. Notify an address change as soon as possible. All communications should include both old and new addresses with zip codes and be accompanied by a mailing label from a recent issue. Allow six weeks for all changes to become effective.

The Hong Kong Institute of Steel Construction
HKISC
c/o Department of Civil and Environmental Engineering,
The Hong Kong Polytechnic University,
Hunghom, Kowloon, Hong Kong, China.
Tel: 852- 2766 6047 Fax: 852- 2334 6389
Email: *ceslchan@polyu.edu.hk* Website: *http://www.hkisc.org/*
ISSN 1816-112X
Science Citation Index Expanded, Materials Science Citation Index and ISI Alerting

ISSN 1816-112X

Science Citation Index Expanded, Materials Science Citation Index and ISI Alerting

Advanced Steel Construction
an international journal

VOLUME 14 NUMBER 1 MARCH 2018

Technical Papers

Advanced Steel Construction Vol. 14, No. 1, pp. 1-21 (2018)

FIRE RESISTANCE OF A DAMAGED BUILDING EMPLOYING BUCKLING RESTRAINED BRACED SYSTEM

Elnaz Talebi [1], Mahmood Md Tahir [1,*], Farshad Zahmatkesh [2], Ahmad B.H. Kueh [1]and Aly M. Said [2]

[1] *UTM Construction Research Centre (UTM-CRC), Institute for Smart Infrastructure and Innovative Construction (ISIIC), Faculty of Civil Engineering, Universiti Teknologi Malaysia, 81310 Johor Bahru, Malaysia*
[2] *Department of Architectural Engineering, the Pennsylvania State University, University Park, PA 16802, USA*
**(Corresponding author: mahmoodtahir@utm.my)*

Received: 29 July 2016; Revised: 28 November 2016; Accepted: 14 February 2017

Abstract: This study investigates the influence of buckling restrained brace systems (BRBs) on the overall structural stability against fire following a severe incident, which caused the failure of a column on the first storey of a steel building. A four-storey moment frame fitted with the inverted-V arrangement of braces is modelled, considering a multi-hazard approach. This technique concentrates on a structural plane frame that is designed to meet the progressive collapse criteria according to the U.S. Department of Defense guidelines and assumes that an extreme event damaged a first-storey centre column, before the exposure to an ensuing fire. The performance of BRBs in preventing the global collapse of the structure due to a post-event fire is compared with that of ordinary concentric brace systems (OCBs). The results indicate that BRBs offer a higher global collapse time to the building owing to the greater stiffness they provide to the structural frame. The fire resistance provided by BRBs is restricted to the participation of bracing elements and framing girders afterwards. In the case of OCBs, columns contribute to the structural resistance prior to the full capacity of braces used. To conclude, it is found that BRBs are more capable in maintaining the stability of a damaged building against fire resulting from an extreme event than OCBs.

Keywords: Buckling restrained brace (BRB); Ordinary concentric brace (OCB); Progressive collapse; Damaged building; Fire response.

DOI: 10.18057/IJASC.2018.14.1.1

1. INTRODUCTION

Progressive collapse is a continuous event that initiates by the local damage of structural load-bearing members and results in the disastrous global breakdown of the entire building. There have been several instances of progressive collapse, such as that of the London Ronan Point residential tower block in 1968 and the Oklahoma Alfred P. Murrah Federal Building in 1995. Since the partial collapse of the Ronan Point building in 1968 [1], the structural engineering community has faced significant challenges to prevent such alarming incident. In response to these and similar incidents, structural standards and building codes now include design guidelines and resistance criteria [2-4]. Recently, extensive research has been dedicated to investigating the progressive collapse resistance of various types of structural frames. Many of these studies have shown that seismically designed structural frames are less susceptible to the progressive collapse under the abrupt loss of column caused by severe incidents [5-7]. Kim et al., [8] compared the progressive collapse resistance provided by various steel braced frame systems with that of moment resisting frame (MRF). They showed that appending the braced systems to the structural moment frames enhanced the resistance of a building against progressive collapse, while the bracing systems remained stable after the abrupt column loss. Fu [9] demonstrated that using braced resisting systems with cross arrangement could

noticeably improve the progressive collapse resistance of a multi-storey structure. Mohamed [10] suggested that the large forces generated due to the sudden removal of the column could be efficiently moderated by appending bracing members to the structural frame. Khandelwal et al., [11] demonstrated that altering the type of braced resisting systems from concentric to eccentric could successfully enhance the progressive collapse resistance of the entire structure. Although several studies have discussed the progressive collapse mechanisms of buildings with conventional bracing systems, none has considered the effect of applying improved types of bracing systems such as buckling restrained braces (BRB) on preventing the progressive collapse of structural frames subjected to extreme events.

It is well known that the strength of ordinary concentric braces (OCB) drops rapidly due to early buckling of compressive bracing components, before braces exhaust their capacity. This shortcoming in the response of OCBs has led to the development of buckling restrained braces. The compressive bracing elements in BRBs exhibit superior performance due to their buckling resistant characteristic compared to OCBs [12]. The principal advantages of BRB systems are high energy dissipation ability, high ductility and almost symmetrical hysteretic responses in tension and compression [13]. In terms of constituent components, BRBs are composed of a yielding steel core encased in a concrete-filled steel hollow casing to prevent buckling (Figure 1(a)), non-yielding and buckling-restrained transition parts as well as non-yielding and unrestrained end regions (Figure 1(b)). About 60% to 70% of the entire length of the core is restrained by the casing. In these bracing systems, compression stresses are mainly sustained by the restrained portion of the core. Furthermore, the yield strength of the steel core is much lower than that of steel tube casing. This allows the core to yield in the same manner during tension and compression prior to the casing, thus considerably enhancing the energy dissipation abilities of BRBs in comparison with ordinary bracing systems.

Because of Poisson's ratio effect on the steel core, it expands when it is compressed. To prevent the axial stress transition from the core to the restrainer (concrete filled-in steel tube casing), a certain amount of clearance between the core and concrete is provided to avoid friction (Figure 1(c)). In addition to this gap, a debonding agent is also applied to the surface of the core to minimize the friction between the core and concrete, as shown in Figure 1(a).
Due to the aforementioned advantages of BRBs, the main aim of this study is to evaluate the effectiveness of this system in maintaining the stability of a building damaged by an extreme event and subjected to a resulting fire.

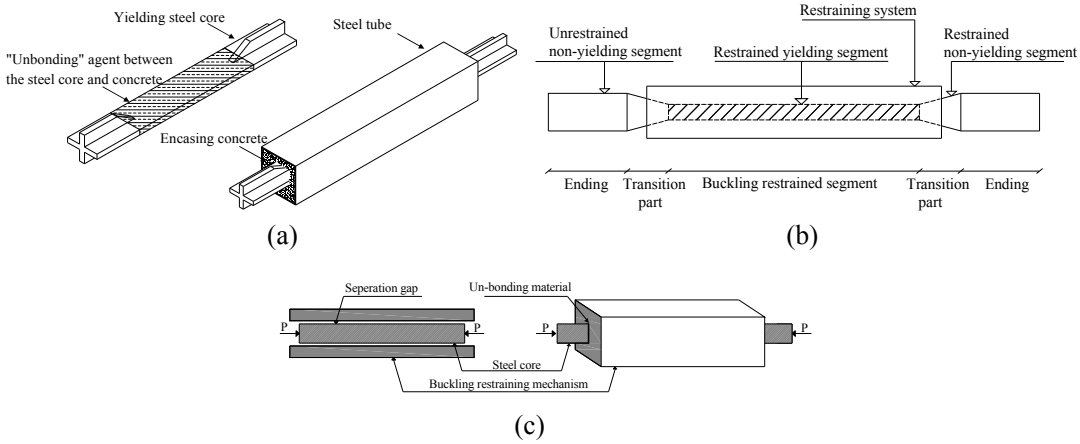

Figure 1. Detail of BRB: (a) General Structure, (b) Steel Core Constituent Segments and (c) Separation Gap at Steel Core-restrainer Interface [14]

Although building guidelines [2-4] have improved the buildings' ability to withstand a collapse disproportionate to the damage suffered during a severe incident, current structural collapses have underlined the need to further improve the progressive collapse resistance of buildings damaged by a serious event then subjected to an ensuing fire. This situation is not clearly addressed in current progressive collapse design provisions. It can be however, crucial if a structure is to experience such incident. The majority of research on progressive collapse resistance of structures focuses on the events that put a building in danger of global collapse without considering a subsequent fire. This phenomenon has seldom been investigated. Della-Corte et al., [15] studied the response of a steel moment resisting frame under fire conditions after it had experienced permanent deformations caused by a seismic activity. Chen and Liew [16] estimated the resistance of columns under fire conditions in a steel building that had been damaged by a blast.

Owing to the limited literature on the aforementioned issue, this paper examines the response of a building damaged by a severe incident and subsequently subjected to an ensuing fire using a multi-hazard approach. For this purpose, a four-storey steel moment frame fitted with BRB elements and designed to resist progressive collapse in accordance with the guidelines given by the U.S. Department of Defense [3] is used as a prototype structure for study. The specified structural steel frame is assumed to be subjected to the sudden loss of the first-storey middle column due to a severe event and is subsequently exposed to a fire resulting from that event. The efficacy of BRBs in preventing the eventual structural collapse due to fire loading is compared with that of ordinary concentric brace systems (OCBs). To perform the analysis, a multi-hazard approach considering two main scenarios is utilized, namely the sudden loss of the first-storey middle column caused by an extreme event and the consequent fire. The detail of the modelling approach as well as the analysis sequence is described next.

2. METHODOLOGY

In order to assess the effect of bracing systems on maintaining the overall stability of a damaged steel building against fire, a multi-hazard approach is considered in this study. In this technique, first, the structure is subjected to a severe event (Stage 1 in Figure 2(a)). This is then followed by a sudden removal of the first-storey middle column, shown as Stage 2 in Figure 2 (b). After the column loss, the load previously carried by this column is redistributed to the adjacent members until the onset of stable plastic deformations as progressive collapse resistance takes place (Figure 2(b)). Finally, a severe fire in the vicinity of the removed column is developed as a result of the extreme event in stage 1 (Stage 3 in Figure 2(c)).

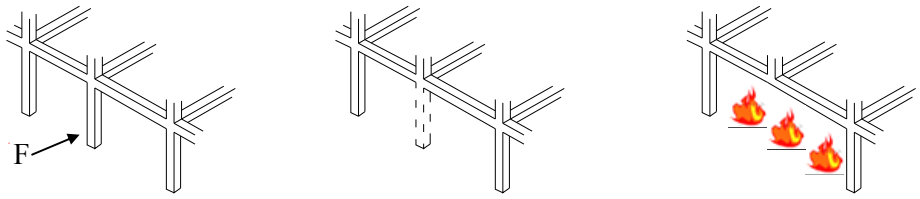

Figure 2. Stages considered in the Multi-hazard Approach as (a) stage 1, (b) stage 2 and (c) stage 3

Considering the sequential events illustrated in Figure 2, the analyses are performed according to the order described below. First, the progressive collapse analysis is performed through a sudden removal of the middle column to ensure that the building conforms to DoD guidelines [3]. In this stage, analysis is threat-independent and the reason for member failure is not taken into account. To simulate the progressive collapse phenomenon, the alternative path method is adopted. Two types of analysis are implemented, namely, the nonlinear static and the dynamic analyses, using the SAP2000 program version 14.0 Advanced [17]. Afterwards, the fire resistance of the damaged structure is evaluated. In this stage, it is presumed that the onset of fire is immediately after the structure reaches a stable permanent deformed shape caused by column loss. To perform the structural fire analysis, a two-dimensional nonlinear plane frame is modelled, using Vulcan program version 10.12.0 [18].

2.1. Progressive Collapse Analysis

The capacity of a structure to sustain gravity loads without collapse through redistributing the internal forces resulting from the abnormal loads defines its progressive collapse resistance. To perform an appropriate analysis for progressive collapse, it is essential to follow the sequence of failure occurrence within the structural elements. Accounting for the dynamic response when applying static analysis, both the GSA [2] and the DoD [3] proposed the application of twofold the load combination as a dynamic amplification factor (Figure 3).

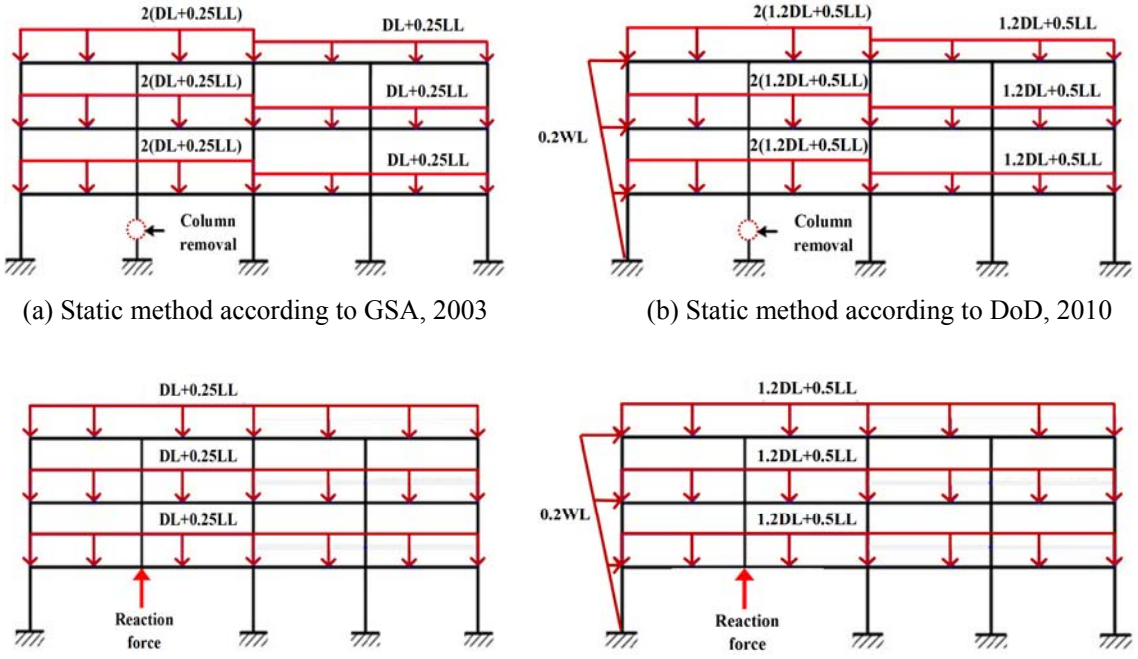

(a) Static method according to GSA, 2003

(b) Static method according to DoD, 2010

(c) Dynamic method according to GSA, 2003

(d) Dynamic method according to DoD, 2010

Figure 3. Load Combinations used for the Progressive Collapse Analyses based on the GSA [2] and the DoD [3] guidelines

The nonlinear static pushdown (vertical pushover) analysis is implemented first, such that the response of the structural frame is verified by progressively enlarging the downward displacement in the top position of the lost column. The dynamic analysis is carried out afterwards, in which the column removal is simulated as follows. First, the reaction forces operating on a column specified for a remove scenario are calculated prior to its elimination.

Next, the column is replaced by the computed forces on the node in the position of the corresponding column. Finally, these reaction forces are concurrently and suddenly brought to the zero value. Practically, this phenomenon can be simulated in the SAP2000 by imposing at the corresponding node an equal set of forces in the opposite direction, as shown in Figure 3.

In order to simulate the quick rate of column removal from an equilibrium condition, the reactions are eradicated after a certain time has elapsed (Figure 4). In the current study, the removal time is considered as 5ms, which connotes a quasi-instant elimination [20].

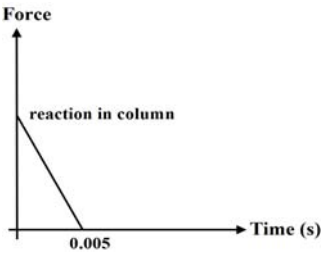

Figure 4. Time Histories of Applied Loads used for Simulation of Column Removal in Dynamic Analysis

2.2 Structural Fire Analysis

The fire resistance of a specified damaged structure is verified using the Vulcan program [18]. In Vulcan, beam-column structural members are modelled by three-noded line elements containing two Gaussian integration points along their length, and these elements are connected to each other at the nodal intersection points [19]. In this FE program, each line element can have different temperatures distributed across its cross-section, which leads to changes in the material properties and thermally induced strains at elevated temperatures. This is done by dividing each element into a matrix of segments. By means of this division, each part can have its own characteristics [19]. In this program, issues such as material thermal expansion and degradations in the stress-strain relationship are taken into account. Also, both material and geometric nonlinearities are considered in this FE program. With this information, Vulcan is adequate for the analysis of structural frames under fire conditions.

3. NUMERICAL FE MODEL

3.1 Problem Description

The effect of BRBs on maintaining the overall stability of structural frames is compared with that of an ordinary concentric braced system (OCBs). For this, a structural moment frame fitted with the inverted-V braces is modelled numerically. This type of bracing configuration has been established to offer an enhanced progressive collapse resistance due to a sudden column loss in comparisons to other bracing arrangements [8]. As shown in Figure 5, the specified structural plane frame has four storeys, each of which is 3.4 m high. There are four bays, each with a 6.0 m span, exposed to a sudden loss of the first-storey centre column (C3-1 in Figure 5), followed by the symmetrical deformation of the structural frame. In Figure 5, the sections are nominated such that each member's name comprises three main letters. The first letter corresponds to the element type, i.e., C for column and Br for braces. The second letter shows the element position while the third letter refers to a storey level, BrL-1 for instance denotes the left brace at the first storey.

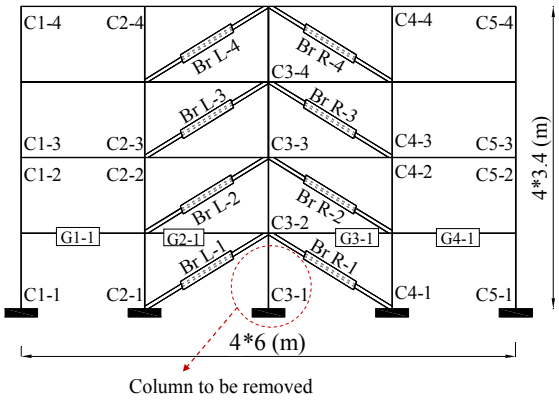

Figure 5. Structural Plane Frame with Inverted-V format of BRB Elements

The beams and columns are made of ASTM A992 steel and their section sizes are as listed in Table 1.

Table 1. Cross-sections of Beams and Columns

Storey	Column section		Beam section
	external	internal	
Ground floor	W5×19	W8×40	W21×57
First floor	W5×19	W8×40	W21×57
Second floor	W4×13	W5×16	W21×57
Third floor	W4×13	W5×16	W21×57

The bracing elements for OCBs are rectangular hollow steel sections (HSS) (Figure 6(a)), made of ASTM A500-46 structural steel. Similarly, HSS are used as the steel tube casing in BRBs, while cores of rectangular sections with a nominal yield strength of 250 N/mm^2 (A36 steel) are inserted within the hollow sections (Figure 6(b)). Concrete used to fill the steel tube (restrainer) is of normal weight type with a density of 2400 kg/m^3. The compression strength and Poisson's ratio of concrete are 35 N/mm^2 and 0.2, respectively. The section sizes used for the braces are as listed in Table 2.

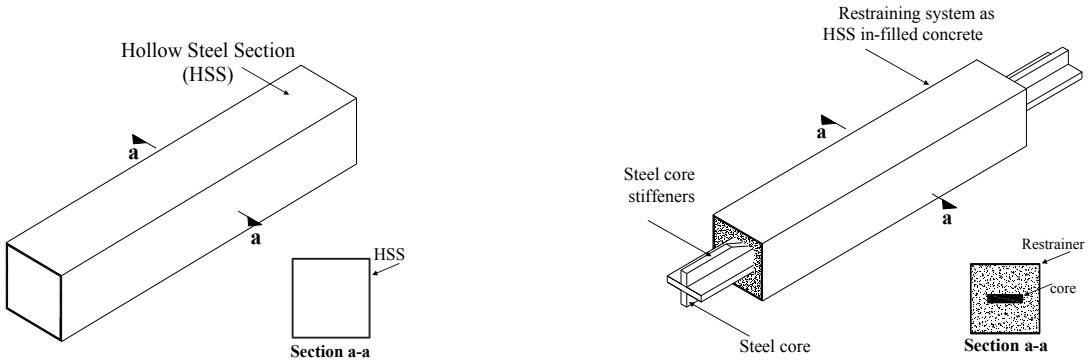

(a) (b)

Figure 6. Overall Scheme and Cross-section of Braces for (a) OCB and (b) BRB Systems

Table 2. Cross-sections of Bracing Elements used for Both Bracing Systems

Storey	BRB section		OCB section
	Steel casing	Steel core (mm)	
Ground floor	HSS4-1/2×4-1/2×0.3125	PL-70×16	HSS4-1/2×4-1/2×0.3125
First floor	HSS4-1/2×4-1/2×0.3125	PL-70×16	HSS4-1/2×4-1/2×0.3125
Second floor	HSS4-1/2×4-1/2×0.3125	PL-70×16	HSS4-1/2×4-1/2×0.3125
Third floor	HSS4-1/2×4-1/2×0.3125	PL-70×16	HSS4-1/2×4-1/2×0.3125

The specified structural plane frame is designed according to the AISC Load and Resistance Factor Design [21] and the Seismic Provisions for Structural Steel Buildings [22]. The design loads of 4.3 kN/m^2 and 2.4 kN/m^2 are assumed for dead and live loadings, respectively, and are uniformly distributed along the length of girders, accounting for the one-way behaviour of floor slabs. The building is designed seismically in accordance with the Minimum Design Loads for Buildings and Other Structures [4]. The parameters for design spectral acceleration, S_s and S_1, are derived as 1.5 and 0.6, respectively, considering the IBC-2006 format [23]. Correspondingly, the site coefficients of 1.0 and 1.5 are obtained for F_a and F_v, respectively, using the response modification factors 6 and 7 for OCBs and BRBs, respectively. According to the AISC Seismic Provisions [22], the strength of bracing connections must be the smallest value of their nominal tensile strength and the maximum load they can sustain. Hence, in this study, the bracing connections are considered to remain elastic throughout the analysis and the plastic hinging is allowed only in braces.

3.2 Modelling of Progressive Collapse Analysis

Finite element (FE) analysis of the specified structural frame is conducted, using the SAP2000 Advanced [17]. Structural elements in the buildings are modelled as an assemblage of finite beam, column and braces. The buckling-restrained braces are modelled implicitly, considering a symmetrical response in tension and compression for defining the plastic hinges within the core elements. To simulate the restraining system in BRB elements, the in- and out-of-plane rotations of the steel core are restrained. The numerical modelling leads to the formation of 228 nodes and 232 frame elements, as shown in Figure 7. For simplicity, the models are considered to be two-dimensional in this study, which may not benefit from the effect of out-of-plane structural elements and the floor systems. To provide the progressive collapse resistance of the structural frame, the beam-to-beam continuity is assumed to be preserved, once the column is removed.

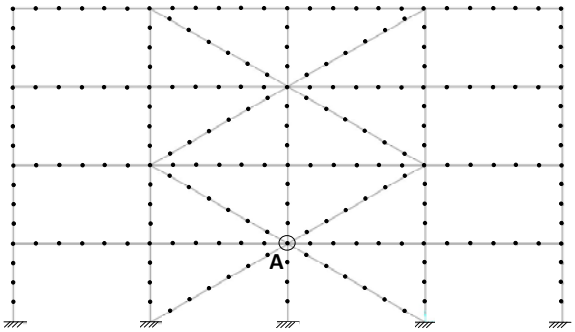

Figure 7. Finite Element Model of Structural Plane Frame in SAP2000 and its Associated Nodes and Elements

In relation to the acceptance criteria for progressive collapse analysis, the GSA guideline [2] provides limitations for structural steel members, based on the maximum ductility and rotation angle of beams, columns and braces. The current study, however, considers the nonlinear force-displacement relations recommended by the Federal Emergency Management Agency (FEMA) [24] instead (Figure 8), because of the more detailed failure criteria presented in FEMA as compared to the GSA guidelines. According to the DoD [3], it is presumed that the entire structural members are at normal temperature throughout the progressive collapse event.

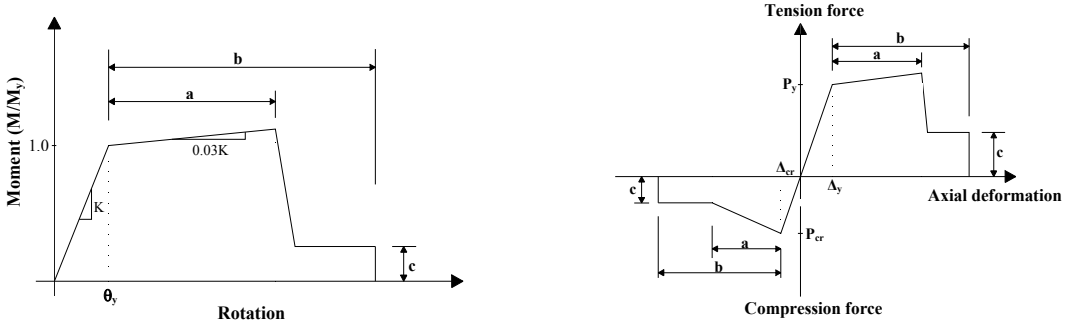

(a) (b)

Figure 8. Force-displacement Relations used for (a) Flexural Members and (b) Braces, according to FEMA 356 [24]

3.2.1 Validation of the progressive collapse analysis model

To ensure the accuracy of the proposed FE model described in Section 3.2 for progressive collapse analysis, a one-storey structural plane frame involving four bays is simulated in the SAP2000 [17], as shown in Figure 9.

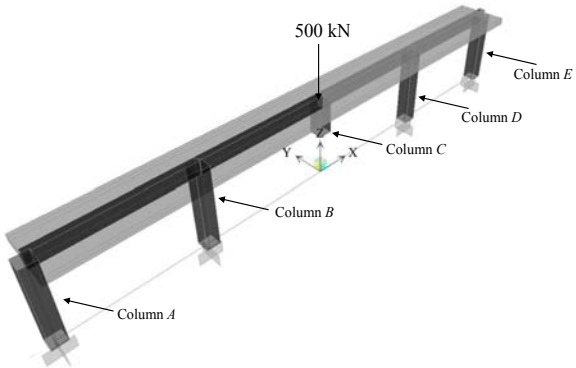

Figure 9. Load and Boundary Condition of the Proposed FE Model for Validation

The validating model duplicates a 1/3-scale testing of a composite plane frame conducted by Guo et al., [25]. The referenced experiment simulated the progressive collapse of a structural frame subjected to a sudden loss of the middle column. The test simulation carried out was based on similar techniques considered for modelling the prototype structure, as mentioned in Section 2 of this paper. In terms of elemental properties, the section sizes and boundary conditions are the same as those considered in the test. A concise description of the section sizes and properties is provided in Table 3.

Table 3. Section Sizes and Properties used in the Validating Model under Progressive Collapse Analysis

Element	Section*		f_y (MPa)		f_u (MPa)		E_s (10^5 MPa)	
(mm)	Flange	Web	Flange	Web	Flange	Web	Flange	Web
Beam	H200×100×5.5×8		269	275	401	411	1.96	2.09
Column	H200×200×8×12		247	276	396	415	2.00	1.98

*The dimensional order is: H-overall depth (d) × flange width (b_f) × web thickness (t_w) × flange thickness (t_f)

For comparison with the referenced experiment by Guo et al. [25], we have taken into account in the validating model the same specifications and settings adopted by them. Reinforced concrete (RC) slabs of 800 mm width with a thickness of 100 mm are used in the models. In relation to the reinforcement ratio, a value of 85% is adopted for meshing the RC slabs. For reinforcing the longitudinal direction, steel bars 12 mm in diameter as well as two layers of transversal bars 8 mm in diameter are used within the slabs. Shear studs 16 mm in diameter are connected to the steel beams, allowing 100 mm spacing between each. In the experiment [25], all the columns are fixed at the bottom except the one chosen for the column loss scenario. In the FE model also the bottoms of columns are defined as fixed supports, analogous to those set in the test. In order to simulate the column loss, a 500 kN static concentric load is applied at the top location of Column C (Figure 9), as implemented in the test.

Figure 10 compares the vertical displacement of Column C results from the numerical solution with those obtained experimentally. To foster more confidence in the proposed model, the vertical displacements of Column C versus horizontal displacement of other intact columns (Columns A, B, D and E in Figure 9) are compared in Figure 11. Altogether, the trends of graphs are closely aligned with very similar values for both approaches, which shows an acceptable agreement between the numerical and experimental simulations (Figs. 10-11).

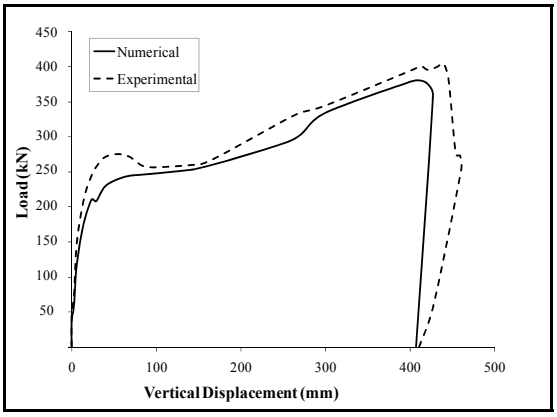

Figure 10. Axial Load versus Vertical Displacement of Column C in the FE model and the Test [25]

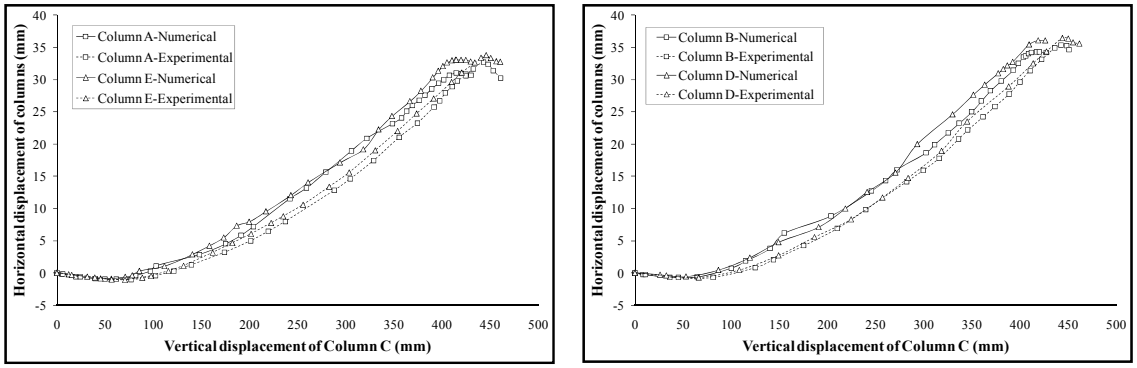

(a) External columns (b) Internal columns

Figure 11. Horizontal Displacement of (a) External and (b) Internal, Intact Columns versus Vertical Displacement of Column C in the FE Model and the Test [25]

The proposed FE model slightly underestimates the displacement of framing columns, as compared with those obtained experimentally. This can be attributed to the identified modelling parameters such as material nonlinearity, which considerably affects the accuracy of numerical results. Besides, since progressive collapse may induce local reverse loading, the accurate depiction of unloading in the constitutive relationships while defining material models can be significant [26]. As we are more concerned with the overall performance of the structure, this model is adequately accurate to perform the progressive collapse analysis.

3.3 Modelling for Structural Fire Analysis

After performing the progressive collapse analysis and ensuring the resistance of structural frame against specified column loss scenario, the resistance of the damaged structure against post-event fire was analysed. Figure 12 shows the scheme of damaged structure exposed to fire loading. The heated columns (C2-1 and C4-1 in Figure 5) are subjected to fire on four sides and the heated girders (G2-1 and G3-1 in Figure 5) are exposed on three sides, assuming their top face is sheltered by floor slabs. It is presumed that all heated elements are exposed to temperature rise uniformly across their sections during heating time.

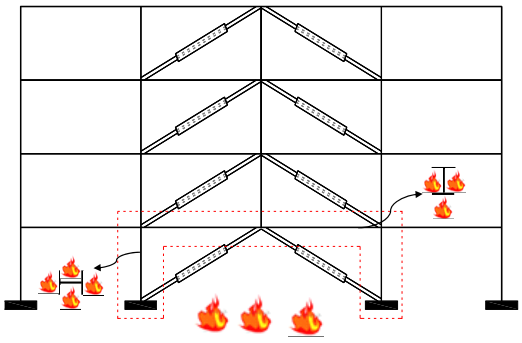

Figure 12. View of Damaged Structural Plane Frame, subjected to the Post-event Fire

As the main aim of this study is to verify the overall influence of BRB systems on the fire resistance of a damaged structure in comparison to OCBs, the bracing elements are assumed to be insulated (remain unheated) throughout the heating time. In this phase of simulation, the model conservatively considers that the whole load redistribution will occur in the parts of the frame above and adjoining the removed column (Figure 12).

The effects of natural post-flashover are ignored by defining the ISO 834 fire curve [27] in the models. Although this curve does not comprise the cooling phase or account for the compartment properties, it is employed as a relatively conservative approximation to track the ultimate failure by exposing the damaged building to long-term duration of elevated temperatures. The structure is assumed to be a typical office building with a total line load of 40 kN/m in fire condition. Structural elements in the buildings are modelled as an assemblage of finite beam-columns, braces and connections. In Vulcan, the beam-columns are represented by three-node line elements with two Gaussian integration points along their length. The buckling-restrained braces are modelled implicitly, using three-node line elements. BRB sections are defined as concrete-filled hollow steel elements with the core inside and the clearance between the steel core and the restrainer is modelled using the gap elements in Vulcan. To simulate the restraining system provided by the concrete and the steel casing on the core in preventing the buckling of BRB elements, the in- and out-of-plane rotations of the steel core are restrained. In Vulcan, temperature-dependent mechanical properties for steel recommended by Eurocode 3 (EC 3) Part 1.2 [28] are adopted, as shown in Figure 13 (a). The average value of the coefficient of thermal expansion for steel material (1.4×10^{-5}/°C), recommended by EC3, is used. Thermal properties of concrete at elevated temperature are extracted from Eurocode 4 (EC 4) Part 1.2 [29], as shown in Figure 13(b). Moisture content of 3% is adopted for the concrete. The effect of creep in the steel at high temperatures is considered implicitly in the stress-strain relations as proposed in EC3. All possible nonlinearities such as geometric nonlinearities are also considered in the model. To account for the influence of floor slabs on temperature distribution within the beams, it is presumed that the temperature of the heated beam at the top flange is 70% of the temperature at its bottom flange and web.

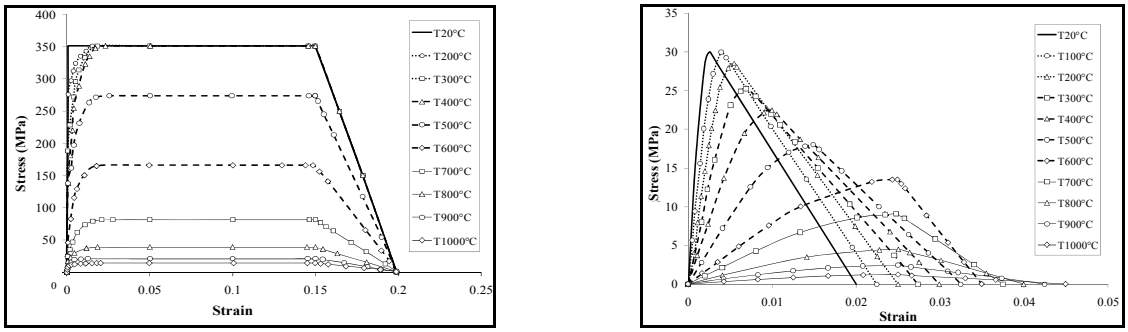

(a) (b)

Figure 13. Stress-strain Relationship of (a) Steel and (b) Concrete, at Elevated Temperature

3.3.1 Validation of the structural fire analysis model

The accuracy of the proposed model for structural-fire analysis (described in Section 3.3) is verified by comparing the FE results with those measured in a test carried out by Rubert and Schaumann [30]. As demonstrated in Figure 14, the model comprises of two structural plane frames, an L-shaped span (Figure 14 (a)) and a one-storey double span frame (Figure 14 (b)). For comparison between the numerical results and the test data, the current study makes the same assumptions as those considered in the experiment [31]. The modelled frames were all uniformly heated, using the standard ISO 834 [27] fire curve. The structural elements were made of IPE80 profiles of I-section.

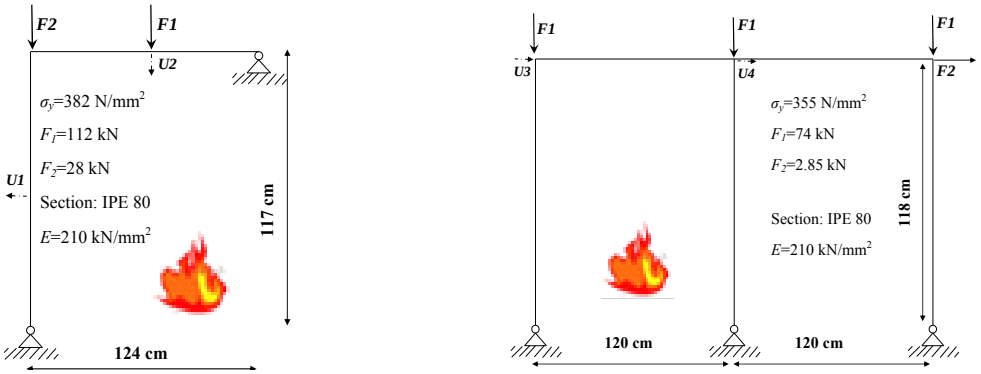

Figure 14. Structural Steel Frames Tested in Fire by Rubert and Schaumann [30]

Figure 15 compares the displacements at different locations within the modelled frames for the FE solution and the test observations. It can be seen that the results generated by the current model are in good agreement with the experimental data. Hence, this model is adequately accurate to perform the structural-fire analysis using the Vulcan program.

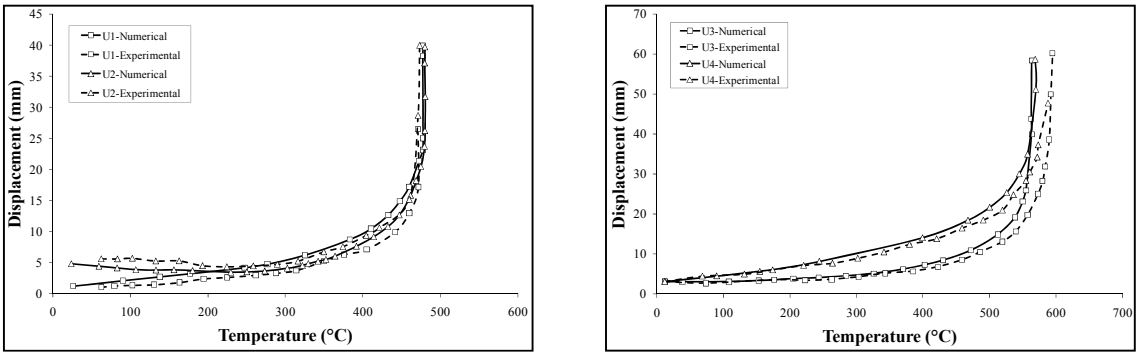

Figure 15. Comparison of Displacement at Different Locations within the Frames between the proposed FE Model and the Test [30] Results

4. RESULTS AND DISCUSSION

4.1 Progressive Collapse Analysis

The study presented in this paper focuses on the first-storey middle column removal shown in Figure 5 as C3-1. The specified scenario stands for one of the most typical and most critical framing column losses. This could be attributed to a higher restraint provided by the neighbouring elements onto the centre column, resulting to the earlier failure of the corresponding column because of the highest axial force experience within it. In order to track the progressive collapse mechanism and to ensure the resistance of the structural frame against progressive collapse under the specified damage scenario, two analyses are performed in the SAP2000 [17]. The results of each analysis are discussed next.

4.1.1 Static pushdown analysis

Nonlinear pushdown (vertical pushover) analysis is performed such that the middle column at the ground level (C3-1 in Figure 5) is removed and the vertical displacement at the top point

location of the corresponding column (Joint A in Figure 7) is increased gradually afterwards. In the pushdown analysis, the maximum strength with a value of less than 1.0 reveals that the structural frame is not strong enough to withstand the 2(DL+0.25LL) load amount proposed by GSA guideline [2]. With respect to this criterion, the pushdown curve is represented in Figure 16 for examining the progressive collapse resistance of a structural frame.

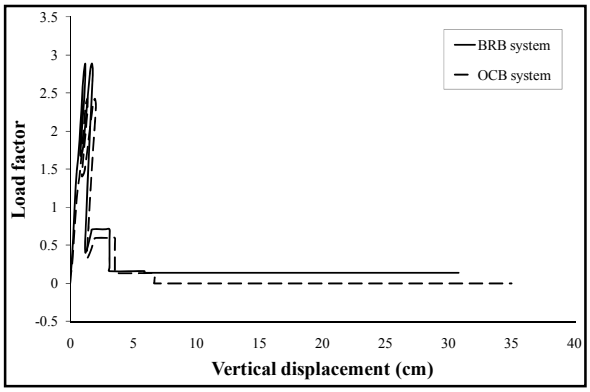

Figure 16. Comparison of Pushdown Curves Versus Vertical Displacement for Both Bracing Systems

Figure 16 shows that the load factor attains a maximum value of 2.78 and 2.45 in BRBs and OCBs, respectively. This is followed by an abrupt reduction in the strength, caused by further increase of vertical displacement after the maximum strength is gained, for both bracing systems.

The variation of axial forces within failed elements for both bracing systems is illustrated in Figure 17, in which the elemental failure sequence is represented by the number order, i.e., 1, 2, 3, etc. In this figure, the member forces are normalized by dividing the compressive member forces by the buckling load, P_{cr}, and tensile member forces by the yielding load, P_y.

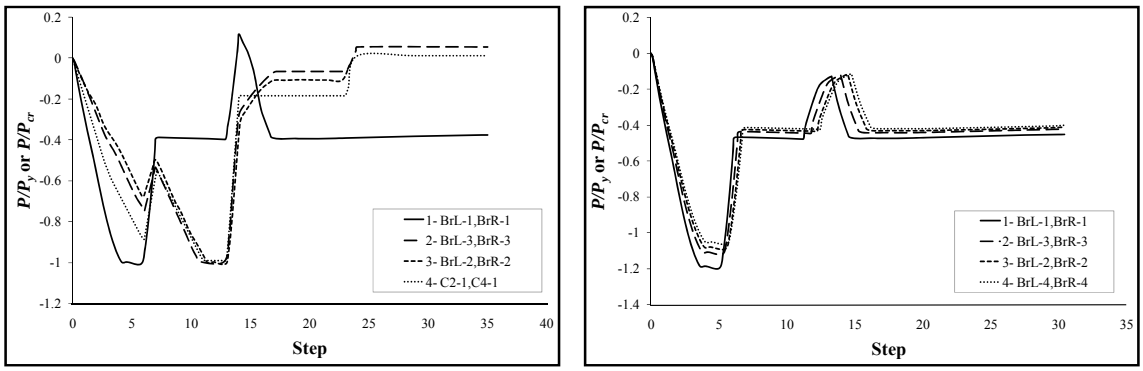

(a) (b)

Figure 17. Variation of Axial Force within Failed Elements in (a) OCB and (b) BRB System

Figures 16-17 reveal that both BRB and OCB systems meet the acceptance criterion according to GSA [2], i.e., maximum strength > 1. Hence, the selected structural frame is capable of resisting the progressive collapse due to the designated column loss scenario. It is worth mentioning that although both bracing systems adequately resist progressive collapse, the resistance provided by BRBs is higher than that of OCBs, owing to the higher stiffness the former provides to the structural frame.

4.1.2 Nonlinear dynamic time history analysis

As mentioned in Section 2.1, the nonlinear dynamic analysis is performed by abruptly eliminating the reactions acting on the lost column (Figure 3 (c-d)). Figure 18 shows the vertical displacement at the top point location of the removed column (Joint A in Figure 7), resulted from the nonlinear dynamic time history analysis. In Figure 18, the horizontal marked lines represent the vertical displacement of the corresponding column resulting from the linear static analyses for the condition whereby the structural frame is subjected to the DL+0.25LL load combination.

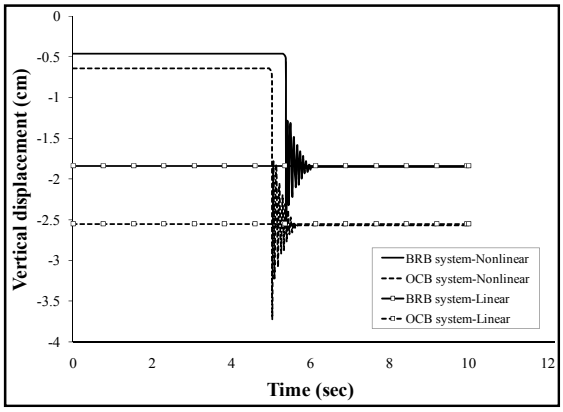

Figure 18. Vertical Displacement at the Top Point Location of Removed Column for Both Bracing Systems

Figure 18 shows that the dynamic response slowly converges to that of the static analysis (without imposing the dynamic amplification factor of two). Evidently, the constant values resulting from the linear elastic responses are almost identical to the corresponding steady dynamic values, for both resistance systems. This means there is no permanent deformation and the structural frame's behaviour remains elastic for both BRB and OCB systems. Accordingly, the structural frame is capable of resisting progressive collapse due to the specified column loss scenario in both BRBs and OCBs. The only difference is that the progressive collapse resistance provided by BRBs is higher than that of ordinary systems. The higher maximum load factors, which resulted from the static push down analyses, with the smaller vertical displacements at Joint A of the Column C3-1 resulting from nonlinear dynamic response for BRBs, offer good evidence of the system better resisting capability. By ensuring the progressive collapse resistance, the damaged building is now ready to be analysed under the post-event fire. The results of structural-fire analysis are discussed next.

4.2 Structural-Fire Analysis

The temperature distribution within the heated beams and columns (shown in Figure 12) against elapsed heating time is represented in Figure 19 based on the modelling approach discussed earlier in Section 3.3. Results show that the average temperatures experienced by the heated columns are higher than those of the heated beams. This can be attributed to the influence of floor slabs, which shield the top face of heated beams from fire.

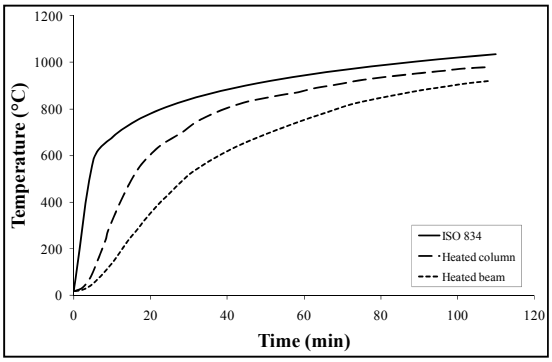

Figure 19. Temperature-time History within the Cross-section of Heated Elements subjected to the ISO 834 Fire Curve

By increasing the heating time in the damaged structure, the top point of the removed column (Point *R*" for OCBs in Figure 20(a)) tends to move downwards and as a direct result, the axial force within the braces and the intact columns (adjacent to the lost column) rises. This process is continued until the column reaches its yield strength, leading to the failure of adjacent members. The final state of failure for the structural frame with both bracing systems is illustrated in Figure 20.

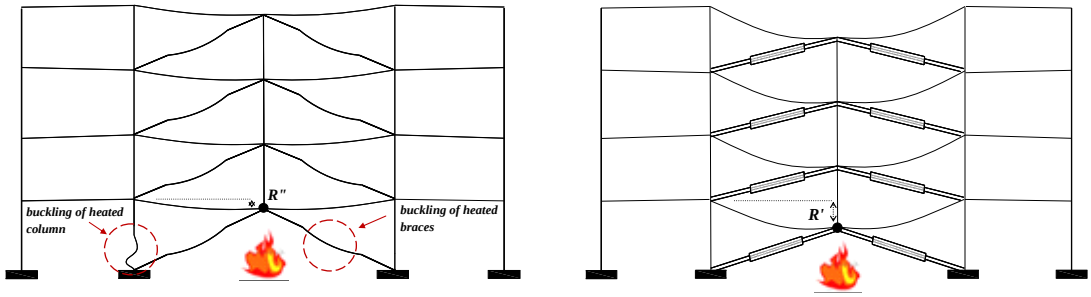

Figure 20. Failure Scheme of a Damaged Structure with (a) OCB and (b) BRB Systems, after Exposure to Post-event Fire

In the damaged structure restrained with the OCB system, the deflection experienced by the heated girders at the location of the removed column (*R*" in Figure 20 (a)) is less than that of the BRB system (*R*' in Fig 20 (b)). This phenomenon corresponds to the failure process of the structural frame with BRB and OCB systems. In terms of the failure scheme of a damaged building exposed to fire, the response of a structure with OCBs is such that the braces on the ground level yield first. This is followed by the buckling of braces on the second and third storeys before they reach their full capacity and leads to the buckling of the heated column on the first storey (Figure 20 (a)). With the buckling of the column, the building with an OCB system loses the majority of its strength and the structural global failure starts. In contrast, the structural frame with a BRB system remains stable, thanks to the buckling-resistant characteristic of braces, which leads to braces solely maintaining the overall stability of the building during fire (Figure 20 (b)). Consequently, it can be seen that at the moment when the damaged structure with OCB has lost most of its strength, the same building with a BRB system is able to resist further girder deflection and higher axial forces induced within the columns and braces due to fire loading.

Figure 21 compares the deflection of heated girders (*G*2-1 and *G*3-1 in Figure 5) at the vicinity of removed column for the structural frame restrained with BRB and OCB systems. Results show that through the weakening of heated girders, the damaged structure experiences a slow increase in deflection until it reaches a value of 323 mm after 76 minutes (Point *A*' in Figure 21) and 397 mm after 72 minutes (Point *A*" in Figure 21) in BRBs and OCBs, respectively. At this point, the deflection curve quickly rises to a value of 393 mm (Point *B*' in Figure 21) in BRBs while there appears no increase for OCBs. This is because the buckling restrained braces append an additional strength to the damaged structure owing to the buckling-resistant behaviour of the braces, as compared to OCBs. As a direct result, for the BRB structural frame the failure starts in the girders after the braces reach their yield strength and fail with no signs of buckling in the framing columns (Figure 20 (b)). In contrast, for OCBs the braces fail before reaching their full capacity, leading to the participation of the first-storey column to resist the post-event fire. Hence, the girder deflection for the damaged building with the ordinary system is similar to that of BRBs, until the fire loaded column fails (Figure 20 (a)) and as a result, there is no further increase in the deflection curve of heated girders for OCBs (Point *A*" in Figure 21).

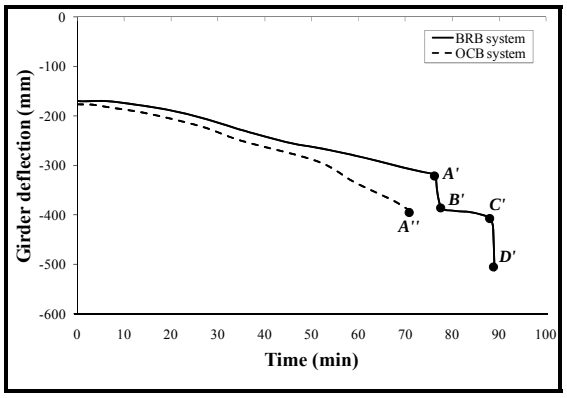

Figure 21. Girder Deflection at the Top Point of Removed Column caused by Temperature Rise

Apparently, the structural frame with BRBs experiences a sharp slope in the heated girder's deflection from Point *A*' to Point *B*' (Figure 21). This quick rise may be attributed to the occurrence of plasticization in the fire loaded girders. The plasticized steel elements begin to unload when they reach the 15% strain and continue unloading until attaining the ultimate strength at 20% strain [30]. At this point, i.e., 20% strain, the structural steel member is unable to carry any further load. For a comprehensive scheme on this phenomenon, the variation of strain against elapsed heating time is shown for the girders within the damaged structure in Figure 22, for both bracing systems.

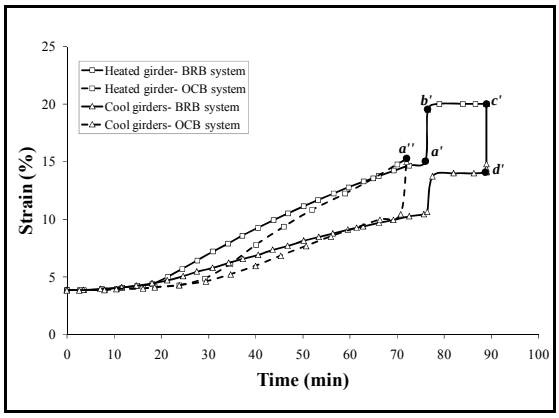

Figure 22. Development of Strain within the Girders of Damaged Structures due to Fire Loading

Obviously, a maximum strain within the heated girders reaches 15% prior to the occurrence of a further rapid rise in the girder's deflection (shown as Points *A*' and *A*" in Figure 21 for BRBs and OCBs, respectively). In terms of 15% strain, it can be seen that the heated girders in the damaged building with BRBs gain the corresponding value after 76 minutes of burning (Point *a*' in Figure 22). Similarly, in the structural frame with OCBs, the fire loaded girders reach 15% strain after 72 minutes (Point *a*" in Figure 22). After the 15% strain is reached, there appears an abrupt increase in the strain until the girder gains an ultimate value of 20% after 86 minutes (Point *b*' in Figure 22) in BRBs. At this point, there is no additional increase in the strain curve of girders for OCBs due to first-storey column failure prior to girders reaching further strain. In BRBs, once the heated girder reaches 20% strain it fails and sheds its load to the cooler girders. The maximum strain experienced by the cooler girders in BRBs is a good example of unloading action in the heated girders, as shown in Figure 22. According to Eurocode 3 [29], at this point there exists an 18% decrease in the stiffness with no reduction in the strength. Once the heated girder transfers its carrying load, the framing girders experience an increase in deflection until the cool girders become overloaded and are unable to sustain any further load. A second sudden increase in the deflection curve (shown as line *C'D'* in Figure 21) shows this phenomenon, which leads to the global failure of the specified frame with BRBs. At this stage, it can be seen that the BRB system maintains the overall stability of the frame for 89 minutes with a maximum deflection of 511 mm experienced in the heated girders (Point *D'* in Figure 21).

With respect to the failure process described hitherto for BRBs, in order to follow the final failure scheme of the OCB system and compare it with BRBs, the response of fire loaded columns in a damaged building should be presented. To this end, the development of vertical displacements within the intact columns adjacent to the removed one (*C*2-1 and *C*4-1 in Figure 5) is demonstrated in Figure 23. Figure 23 shows that both BRBs and OCBs experience a decrease in the axial displacement of the heated columns after an initial increase. This is attributed to the vertical deflection of heated girders, which impose tensile force within the heated columns (that are connected to the girders) and cause an upward movement of the corresponding columns. Apparently, this decrease continues in BRBs with no sudden increase, meaning that there is no sign of column buckling at the time of structural global failure, i.e., 89 minutes. Inversely, for OCBs the vertical displacement increases dramatically up to a value of 67 mm after 72 minutes, which shows that the structural failure starts with the buckling of heated columns at 72 minutes.

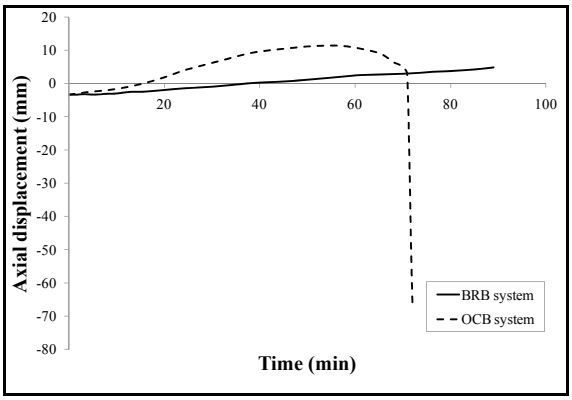

Figure 23. Vertical Displacement Developed within the Fire Loaded Columns (*C*2-1 and *C*4-1) adjacent to the Removed Column

To sum up, the final failure of a damaged structure with OCBs is initiated by the failure of the first-storey heated column (Figure 20 (a)) and that of BRBs by the failure of cool framing girders after the failure of braces and heated girders, respectively. BRB elements are able to absorb the thermally induced axial forces and transfer the loads successfully to the adjacent girders, thus, postpone the columns' buckling. Contrary, the ordinary braces buckle before reaching their full capacity, resulting in buckling of the columns after 72 minutes. BRBs sustain the post-event fire for 89 minutes. This indicates that at the time that a damaged structure with OCB system fails because of the post-event fire, a similar building with BRBs can resist the corresponding event for about 17 minutes more.

5. CONCLUSIONS

In this paper, the effect of the BRB system in maintaining the overall stability of a damaged building against post-event fire in comparison with the OCB system was investigated, using a multi-hazard approach. For this purpose, a two-dimensional plane frame subjected to the sudden removal of a first-storey centre column was subsequently exposed to the standard fire curve. Considering the superior performance of inverted-V arrangement for bracing elements in resisting progressive collapse, this bracing configuration was modelled and compared for both bracing systems. Several important conclusions can be drawn as follows:

(1) In the BRB system, bracing members behave similarly in both tension and compression. Hence, during a column loss scenario they can withstand higher axial forces without the occurrence of buckling in the bracing member. Whereas, in the OCB system, bracing elements are not as effective as expected, owing to the buckling of the braces.

(2) When a localized failure occurs in the first-storey centre column, buckling restrained bracing members are more efficient in transferring the load previously carried by this column to the other stiffer adjacent elements. This makes the BRB system more efficient in maintaining the structural overall stability due to the sudden column loss, as compared with the ordinary bracing elements.

(3) Although both systems withstand the progressive collapse caused by sudden column loss, it is demonstrated that BRB elements are more effective in redistributing the post-event fire loading from heated elements to the other bays, thanks to their buckling-resistant characteristic. Furthermore, it is observed that a structural frame with BRBs can resist greater axial displacements caused by fire loading, in comparison to OCBs.

(4) BRB elements are able to absorb the thermally induced axial forces and transfer the loads successfully to the adjacent girders and prevent the columns' buckling. In contrast, the ordinary braces buckle before reaching full capacity, followed by the buckling of first-storey fire loaded columns.

(5) For a damaged structure restrained with the OCB system, the deflection experienced by the fire loaded girders at the location of the removed column is less than that of BRBs. This is attributed to the participation of girders in resisting the fire loading after BRB elements reach their yield strength. In an ordinary system, the first-storey columns contribute structural resistance after the braces yield, follows by a higher displacement developed within the columns.

(6) Because of the greater stiffness of BRBs, they can resist higher axial forces when exposed to the post-event fire loading. Hence, they increase the global collapse time of the damaged structure and there is a significant difference in the structural failure scheme, as compared to that of OCBs.

(7) The final failure of a damaged structure with OCBs is initiated by the failure of the first-storey fire loaded column, while that of BRBs is initiated by the failure of cool framing girders after the failure of braces and heated girders, respectively.

(8) BRBs sustain the post-event fire for 89 minutes, demonstrating that when a damaged structure with OCB system has failed because of the post-event fire after 72 minutes of heating time, a similar building with BRBs can resist the corresponding event for about an additional 17 minutes.

ACKNOWLEDGEMENTS

The research is financially supported by the Research Management Center (RMC) of Universiti Teknologi Malaysia (UTM) under the post-doctoral fellowship scheme. This support is highly appreciated.

REFERENCES

[1] Pearson, C. and Delatte, N., "Ronan Point Apartment Tower Collapse and Its Effect on Building Codes", J. Perform Constr. Facil. 2005, Vol. 19, No. 2, pp. 172-7.
[2] U.S. General Services Administration (GSA) Guidelines, Progressive Collapse Analysis and Design Guidelines for New Federal Office Buildings and Major Modernizations Projects; 2003.
[3] Dept. of Defense (DoD), Design of Buildings to Resist Progressive Collapse, Unified Facilities Criteria (UFC) 4-023-03, U.S. Dept. of Defense (DoD): Washington, DC; 2010.
[4] ASCE. Minimum Design Loads for Buildings and Other Structures. Standard ASCE/SEI 7-05. Reston, Virginia, USA: American Society of Civil Engineers; 2005.
[5] Khandelwal, K., El-Tawil, S., Sashi, K. and Lew, H.S., "Macromodel-based Simulation of Progressive Collapse: Steel Frame Structures", J. Struct. Eng. 2008, Vol. 134, No. 7, pp. 1070-8.
[6] Kim, J. and Kim, T., "Assessment of Progressive Collapse-resisting Capacity of Steel Moment Frames", J. Constr. Steel Res., 2009, Vol. 65, No. 1, pp. 169-79.

[7] Park, J. and Kim, J., "Fragility Analysis of Steel Moment Frames with Various Seismic Connections subjected to Sudden Loss of a Column", Eng. Struct. 2010, Vol. 32, No. 6, pp. 1547-55.
[8] Kim, J., Lee, Y. and Choi, H., "Progressive Collapse Resisting Capacity of Braced Frames", Struct. Des. Tall Spec. Build, 2011, Vol. 20, No. 2, pp. 257-70.
[9] Fu, F., "3-D Nonlinear Dynamic Progressive Collapse Analysis of Multi-storey Steel Composite Frame Buildings-parametric Study", Eng. Struct., 2010, Vol. 32, No. 12, pp. 3974-80.
[10] Mohamed, O.A., "Assessment of Progressive Collapse Potential in Corner Floor Panels of Reinforced Concrete Buildings", Eng. Struct., 2009, Vol. 31, No. 3, pp. 749-57.
[11] Khandelwal, K., El-Tawil, S. and Sadek, F., "Progressive Collapse Analysis of Seismically Designed Steel Braced Frames", J. Constr. Steel Res., 2009, Vol. 65, No. 3, pp. 699-708.
[12] Xie, Q., "State of the Art of Buckling-restrained Braces in Asia", J. Constr. Steel. Res. 2005, Vol. 61, No. 6, pp. 727-48.
[13] Sahoo, D.R. and Chao, S.H., "Performance-based Plastic Design Method for Buckling Restrained Braced Frames", J. Eng. Struct., 2010, Vol. 32, pp. 2950-58.
[14] Talebi, E., Tahir, M., Zahmatkesh, F. and Kueh, A., "Fire Response of a 3D Multi-Storey Building with Buckling Restrained Braces. Lat Am J. Solids Stru., 2015, Vol. 12, No. 11, pp. 2118-42.
[15] Della-Corte, G., Landolfo, R. and Mazzolani, F.M., "Postearthquake Fire Resistance of Moment Resisting Steel Frames", Fire Saf. J., 2003, Vol. 38, pp. 593-612.
[16] Chen, H. and Liew, J.Y.R., "Explosion and Fire Analysis of Steel Frames using Mixed Element Approach", J. Eng. Mech., 2005, Vol. 131, No. 6, pp. 606-16.
[17] SAP2000. Version 14.0, Analysis Reference Manual, Computers and Structures (CSI), Inc.: Berkeley, CA; 2009.
[18] Vulcan. Vulcan Analysis User's Manual, Version 10.12.0, U.K; 2000.
[19] Huang, Z., Burgess, I.W. and Plank, R., "Three-Dimensional Analysis of Reinforced Concrete Beam-Column Structures in Fire", Eng. Struct., 2009, Vol. 135, pp. 1201-12.
[20] Kokot, S., Anthoine, A., Negro, P. and Solomos, G., "Static and Dynamic Analysis of a Reinforced Concrete Flat Slab Frame Building for Progressive Collapse", Eng. Struct. 2012, Vol. 40, pp. 205-17.
[21] AISC. Load and Resistance Factor Design Specification for Structural Steel Buildings, American Institute of Steel Construction : Chicago, 2005.
[22] AISC. Seismic Provisions for Structural Steel Buildings. American Institute of Steel Construction: Chicago, 2010.
[23] IBC. International Building Code. International Code Council: Falls Church, VA, 2006.
[24] Federal Emergency Management Agency (FEMA). Prestandard and Commentary for the Seismic Rehabilitation of Buildings, FEMA-356: Washington, D.C., 2000.
[25] Guo, L., Gao, S., Fu, F. and Wang, Y., "Experimental Study and Numerical Analysis of Progressive Collapse Resistance of Composite Frames", J. Constr. Steel Res. 2013, Vol. 89, pp. 236-51.
[26] Kwasniewski, L., "Nonlinear Dynamic Simulations of Progressive Collapse for a Multistory Building", Eng. Struct. 2010, Vol. 32, pp. 1223-35.
[27] ISO (International Standards Organization). ISO 834: Fire Resistance Tests, Elements of Building Construction, Switzerland: International Standards Organization, 1980.
[28] EC3. Eurocode 3: Design of Steel Structures-part 1-2: General Rules -Structural Fire Design, British Standards Institution, BS EN 1993-1-2: London, UK, 2005.

[29] EC4. Eurocode 4: Design of Composite Steel and Concrete Structures- Part 1-2: General Rules-structural Fire Design, British Standards Institution, BS EN 1994-1-2: London, UK, 2005.
[30] Rubert, A. and Schaumann, P., "Structural Steel and Plane Frame Assemblies under Fire Action, Fire Saf. J., 1986, Vol. 10, pp. 173-84.

Advanced Steel Construction Vol. 14, No. 1, pp. 22-36 (2018)

FIRE-RESISTANCE STUDY OF RESTRAINED STEEL COLUMNS WITH INITIAL LATERAL DISPLACEMENT

Jin Zhang[1,*], Yi-Xiang Xu[2], Xiao-Jing Yang[1] and Dong-Hao Zhang[1]

[1] *Key Laboratory of Concrete and Pre-stressed Concrete Structures of the Ministry of Education, Southeast University, Nanjing, China*
[2] *Department of Civil Engineering, Strathclyde University, Glasgow, UK*
**(Corresponding author: E-mail: zhangjin0622@139.com)*

Received: 12 June 2016; Revised: 13 February 2017; Accepted: 14 February 2017

ABSTRACT: This study presents an analytical formula based on differential equations of equilibrium to analyse the behaviour of steel columns with initial lateral displacements in fire. The imperfections of the initial flexure of the steel columns are considered. Yielding of the edge fibres at the middle span of a column subjected to elevated temperature is designated as the failure criterion for the fire resistance of the column. After validating the results of the formula using ANSYS, a numerical application is performed to demonstrate the effects of different parameters on the ultimate load bearing capacity. The formula is then used to predict the axial force of axially restrained steel columns based on the displacement coordination condition; then, the axial force is verified by ANSYS. The axial displacement predictions from the proposed method correspond well with those obtained through the finite element method. The critical temperature can also be predicted by calculating the load bearing capacity and axial force at a certain temperature. The results show that the increase of initial lateral displacement and temperature decreases the bearing capacity of the steel column and that the critical temperature decreases with increasing constraint stiffness.

Keywords: Steel column, fire resistance, initial lateral displacement, load bearing capacity, critical temperature

DOI: 10.18057/IJASC.2018.14.1.2

1. INTRODUCTION

Inclining steel columns can have insufficient fire resistance because of their lateral displacement, which can generate additional bending moments in the columns during an earthquake, leading to a higher maximum stress. Therefore, it is critical to investigate the fire resistance of steel members with initial lateral displacements.

A number of publications have described the effect of fire protection losses on the fire resistance of steel columns [1-5]. Unprotected steel structures do not have desirable fire resistance because the temperature of unprotected steel elements increases rapidly in fire due to the high thermal conductivity of steel. Shahria et al. [6] studied the fire performance curves of unprotected HSS steel columns. The moment-rotation behaviour, lateral load-deflection behaviour, stiffness and ductility of the columns at different axial load levels were the main parameters considered in their study. Corte et al. [7-8] studied the effects of structural damage caused by earthquakes on the fire resistance of steel columns and found that the impact of structural damage on fire resistance is more significant if the design of the steel structure only considers the ultimate limit state. Mohammad Hany Yassi [9] described the impact of a post-earthquake fire on the frame structure and proposed two approaches to study the damage caused by a post-earthquake fire. In the first approach, an equivalent static lateral load is applied to the structure to cause lateral deformation, after which the fire load is applied. The second approach is application of time history motion data, which was used to analyse the structure before applying the fire load.

A column is often axially restrained by adjacent members in steel structures, such as slabs, beams, and supports. The restraint has a significant impact on the ultimate load bearing capacity of

columns. At normal temperatures, the axial restraint can improve the ultimate load bearing capacity of the column [10]. Li and Guo [11] showed that restrained steel beams have better fire-resistance capabilities than isolated steel beams. Liu *et al*. [12] investigated the effect of restraints on steel beams during fire experiments. The restraint effect was found to be important for the behaviour of the beam in fire conditions; catenary actions were observed. Studies have also addressed the restraint of a column during a fire. Rodrigues *et al*. [13] showed that neglecting the effect of thermal axial restraints can caused the fire resistance of columns to be overestimated. Huang and Tan [14] proposed a Rankine approach that incorporated both the axial restraint and creep strain for critical temperature prediction of an axially restrained steel column. Li and Guo [15] analysed restrained steel columns during the cooling phase for safety evaluations and repairs of steel structures against fire. Ellobody and Young [16] presented a nonlinear 3-D finite element model investigating the behaviour of concrete-encased steel composite columns at elevated temperatures. Wang and Davies [17] performed tests to determine how bending moments in restrained columns would change and how these changes might affect column failure temperatures.

However, few studies have considered the effects of initial displacement. This paper presents an analytical model based on differential equilibrium equations to predict both the ultimate load bearing capacity of steel columns with initial lateral displacement and the critical temperature of axially restrained steel columns.

2. ULTIMATE LOAD BEARING CAPACITY OF STEEL COLUMNS

2.1 Supported Steel Columns with Both Ends Hinged

Steel columns can laterally move during a fire at either the top or bottom of the column. This paper assumes that the displacement occurs at the top and that the temperature of the entire column is uniform.

Figure 1 shows a mechanical model of a steel column with simply fixed boundary conditions and an initial lateral displacement at its top ends. It is assumed that every column in an actual building has some initial imperfections. The ultimate load bearing capacity for columns with initial imperfections is less than that of perfect columns. The initial flexure of a column can be expressed as

$$y_0 = a_0 \sin(\frac{\pi x}{L}) + \frac{\delta \cdot x}{L} \tag{1}$$

Where L is the length of the column, a_0 is the initial flexure at the mid-span of the column and δ is the initial lateral displacement.

According to the differential equation for equilibrium, if the lateral displacement of the column under the action of a vertical load is represented by *y*, then the following equation can be obtained:

$$E_T I(y - y_0)'' + P(y + e_0 - \delta) = 0 \quad (0 \le x \le L) \tag{2}$$

Where E_T is the elastic modulus of steel at temperature T, e_0 is the load eccentricity distance, and I is the inertia moment of the column.

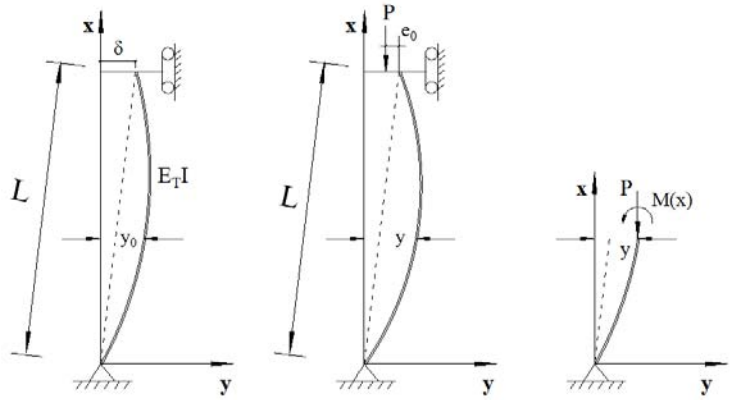

Figure 1. Mechanical Model of a Steel Column with Simply Fixed Ends

Because the displacement at the two ends of the column is fixed, the following boundary conditions can be adopted:

$$y(0)=0,\quad y(L)=\delta \tag{3}$$

For convenience, the following parameters are used:

$$P_{cr}=\pi^2 E_T I / L^2, u=\sqrt{P/P_{cr}} \tag{4}$$

The general solution to Eq. 2 is given by

$$y(x)=C_1\sin\left(\frac{u\pi x}{L}\right)+C_2\cos\left(\frac{u\pi x}{L}\right)+\frac{a_0}{1-u^2}\sin\left(\frac{\pi x}{L}\right)+\left(\delta-e_0\right) \tag{5}$$

where parameters C_1 and C_2 are determined by employing the boundary condition (Eq. 3) as

$$C_1=-\left(\left(e_0-\delta\right)\cos\left(u\pi\right)-e\right)/\sin\left(u\pi\right) \tag{6}$$

$$C_2=e_0-\delta \tag{7}$$

By using the yielding of the edge fibre at the maximum displacement of the column as the failure criterion, the ultimate load bearing capacity of a column with initial lateral displacement should be the solution for the following equation:

$$\frac{P}{A}+\frac{P(\alpha_{\max}-\delta+e_0)}{W}=f_{yT} \tag{8}$$

where A is the area of cross-section of the column, W is the section flexure modulus of the column, f_{yT} is the yield strength of steel at temperature T, and $\alpha_{\max} = y\left(\frac{2L}{3}\right)$.

Eq. 8 is a transcendental equation. Shift the right side of the equation to the left side.

Given the dimension of the steel column at a specified temperature distribution, the ultimate load bearing capacity can be obtained with Eq. 8 via the Newton iterative method.

2.2 Steel Columns with Both Ends Rigidly Supported

The initial flexure of the column can be expressed by

$$y_0 = \frac{1}{2}a_0\left(1\text{-}\cos\frac{2\pi}{L}x\right) + \frac{\delta \cdot x}{L} \tag{9}$$

where L is the length of the column, a_0 is the initial flexure at the mid-span of the column and δ is the initial lateral displacement.

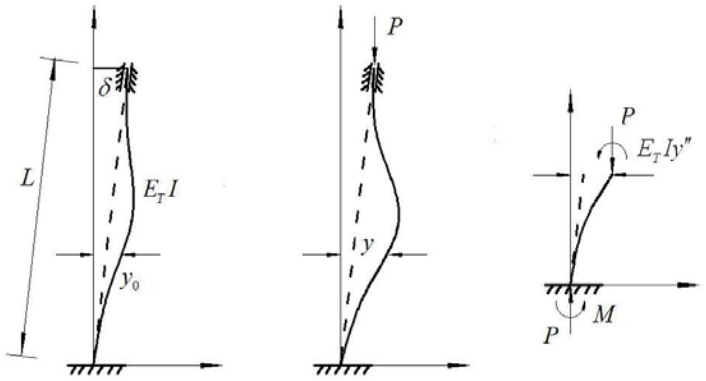

Figure 2. Mechanical Model of a Steel Column with Simple Rigidly Fixed Ends

Figure 2 shows the mechanical model of a steel column with rigidly fixed boundary conditions. According to the differential equation for equilibrium, if the lateral displacement of the column under the action of a vertical load is represented by y, then the following equation can be obtained:

$$E_T I(y - y_0)'' + P(y - \delta) + \mathrm{M} = 0 \quad (0 \le x \le L) \tag{10}$$

The following boundary conditions can be adopted:

$$\begin{cases} y(0) = 0 \\ y(L) = \delta \\ y'(0) = 0 \end{cases} \tag{11}$$

The general solution to Eq. 10 is given by

$$y(x) = C_1 \sin\left(\frac{\sqrt{P}x}{\sqrt{E_T I}}\right) + C_2 \cos\left(\frac{\sqrt{P}x}{\sqrt{E_T I}}\right) + \frac{2E_T I a_0 \pi^2 P}{P\left(PL^2 - 4\pi^2 E_T I\right)} \cos\left(2\frac{\pi x}{L}\right) - \frac{M - \delta P}{P} \tag{12}$$

where parameters C1, C2 and M are determined by employing the boundary condition of Eq. 11 as

$$\begin{aligned} C_1 = -\Bigg(& -2E_T I a_0 \pi^2 P + L^2 MP - 4M\pi^2 E_T I + 2\cos\left(\frac{\sqrt{P}L}{\sqrt{E_T I}}\right) E_T I a_0 \pi^2 P - 4\cos\left(\frac{\sqrt{P}L}{\sqrt{E_T I}}\right) \delta P \pi^2 E_T I + \cos\left(\frac{\sqrt{P}L}{\sqrt{E_T I}}\right) L^2 \delta P^2 \\ & - \cos\left(\frac{\sqrt{P}L}{\sqrt{E_T I}}\right) L^2 MP + 4\cos\left(\frac{\sqrt{P}L}{\sqrt{E_T I}}\right) M\pi^2 E_T I \Bigg) \sin\left(\frac{\sqrt{P}L}{\sqrt{E_T I}}\right)^{-1} P^{-1}\left(-PL^2 + 4\pi^2 E_T I\right)^{-1} \end{aligned} \tag{13}$$

$$C_2 = \frac{\left(2E_T I a_0 \pi^2 P - 4\delta P \pi^2 E_T I + L^2 \delta P^2 - L^2 MP + 4M\pi^2 E_T I\right)}{P\left(-PL^2 + 4\pi^2 E_T I\right)} \tag{14}$$

$$M = -\frac{P\left(-2E_T I a_0 \pi^2 + 2\cos\left(\frac{\sqrt{P}L}{\sqrt{E_T I}}\right) E_T I a_0 \pi^2 - 4\cos\left(\frac{\sqrt{P}L}{\sqrt{E_T I}}\right) \delta \pi^2 E_T I + \cos\left(\frac{\sqrt{P}L}{\sqrt{E_T I}}\right) L^2 \delta P\right)}{PL^2 - 4\pi^2 E_T I - \cos\left(\frac{\sqrt{P}L}{\sqrt{E_T I}}\right) L^2 P + 4\cos\left(\frac{\sqrt{P}L}{\sqrt{E_T I}}\right) \pi^2 E_T I} \tag{15}$$

By using the yielding of the edge fibre at the mid-span of the column as the failure criterion, the ultimate load bearing capacity of the column with initial lateral displacement should be the minimum solutions to the following two equations:

$$\begin{cases} \dfrac{P}{A} + \dfrac{M}{W} = f_{yT} \\ \dfrac{P}{A} + \dfrac{|M - P\alpha_{\max}|}{W} = f_{yT} \end{cases} \tag{16}$$

where A is the cross-sectional area of the column, W is the section flexure modulus of the column, f_{yT} is the yield strength of steel at temperature T, and $\alpha_{\max} = y(\frac{L}{2})$.

Given the dimensions of a steel column at a specific temperature distribution, the ultimate load bearing capacity can be obtained with Eq. 16 by determining the simplest solution.

2.3 Validation of the Deflection Curve via FEM

To verify the equation of the deflection curve proposed in the paper, two FEM models are presented using ANSYS software. The element type used in the analysis is BEAM3, a uniaxial element with compression, tension, and bending capabilities. The element has three degrees of freedom at each node: translations in the nodal x and y directions and rotation about the nodal z-axis. The length of the element is 50 mm.

The mechanical properties of steel at an increased temperature is recommended in the Chinese Technical Code on Fire Safety of Steel Building Structures [18]. Young's modulus at elevated temperatures can be obtained by the following formula:

$$E_{\mathrm{T}} = \chi_{\mathrm{T}} E$$

$$\chi_{\mathrm{T}} = \begin{cases} \dfrac{7T_{\mathrm{s}} - 4780}{6T_{\mathrm{s}} - 4760} & 20°\mathrm{C} \le T_{\mathrm{s}} < 600°\mathrm{C} \\ \dfrac{1000 - T_{\mathrm{s}}}{6T_{\mathrm{s}} - 2800} & 600°\mathrm{C} \le T_{\mathrm{s}} \le 1000°\mathrm{C} \end{cases}$$

where T_s is the temperature of the column, E_T is the elastic modulus of steel at temperature T_s, E is the elastic modulus of steel at room temperature, and χ_T is the reduction coefficient of the elastic modulus at elevated temperature.

The yield strength of steel at elevated temperature can be obtained by the following formula:

$$f_{\mathrm{yT}} = \eta_{\mathrm{T}} f_{\mathrm{y}}$$

$$\eta_T = \begin{cases} 1.0 & 20°\mathrm{C} \le T_{\mathrm{s}} \le 300°\mathrm{C} \\ 1.24\times10^{-8}T_{\mathrm{s}}^3 - 2.096\times10^{-5}T_{\mathrm{s}}^2 & \\ \quad +9.228\times10^{-3}T_{\mathrm{s}} - 0.2168 & 300°\mathrm{C} < T_{\mathrm{s}} < 800°\mathrm{C} \\ 0.5 - T_{\mathrm{s}}/2000 & 800°\mathrm{C} \le T_{\mathrm{s}} \le 1000°\mathrm{C} \end{cases} \tag{17}$$

where f_{yT} is the yield strength of steel at temperature T_s, f_y is the yield strength of steel at room temperature, and η_T is the reduction coefficient of yield strength at elevated temperature.

Model 1 is used to verify the flexure shape of the steel column, the most important parameter in defining the ultimate load capacity of the steel column with initial lateral displacement. In this model, the column section is H300×300×8×16, with L=5 m, ξ=0.001, P=3,000 kN, and *f*y=235 N/mm^2. The temperature of the column with damaged fire protection is 600°C. The results obtained by ANSYS and the proposed approach in this paper are shown in Figure 3; there is general agreement between the FEM and the formula proposed in this paper.

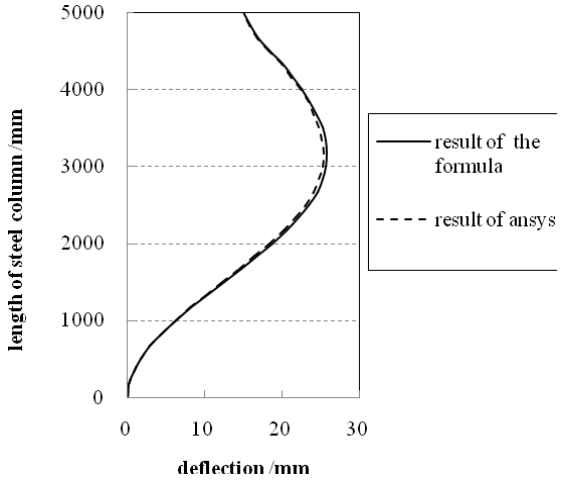

Figure 3. Comparison of the Deflections of the Both-Ends-Hinged Steel Column obtained with ANSYS and the Proposed approach

Model 2 is used to validate the mid-span displacement of the steel column with initial lateral displacement at the top end of the column under different vertical loads P. In this model, the column section is H300×300×8×16, with L=5 m, ξ=0.001, δ=15 mm, and f_y=235 N/mm^2. The temperature of the column is 600°C. The results obtained with ANSYS and the proposed approach in this paper are shown in Figure 4. The mid-span displacement predictions obtained with the method proposed in this paper concur with those obtained by the FEM.

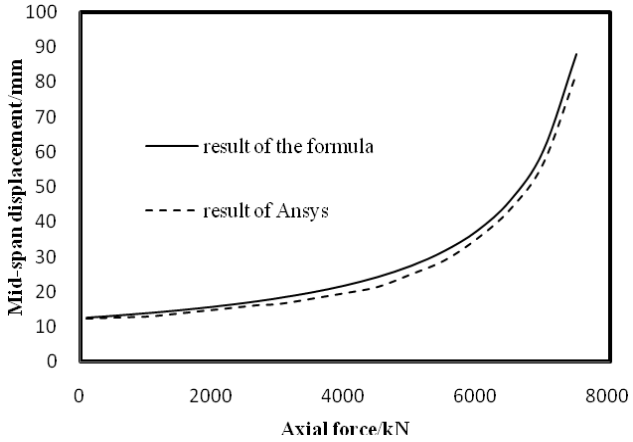

Figure 4. Comparison of the Mid-span Displacements of the Both-ends-hinged-supported Steel Column obtained with ANSYS and the Proposed Approach

2.4 Parametric Analysis

To understand the behaviour of a steel column with initial lateral displacement at the top end during a fire, a column is analysed using the proposed model as an example.

The load bearing capacity coefficient of a steel column with initial lateral displacement is defined as

$$\varphi_T = \frac{P}{f_{y20}A} \tag{18}$$

We can study the variation of the bearing capacity coefficient along with the change in initial lateral displacement, temperature, initial bending, load eccentricity and slenderness by considering a typical steel column with section $H300\times300\times8\times16$.

In this part, we analyse how the initial lateral displacement and temperature affect axially restrained steel columns with both ends having hinged support. Because the initial lateral displacement and temperature are the most relevant parameters for this paper, study of other parameters will be researched in another paper.

The main characteristic parameters of the column are the initial bending rate, ξ=1‰, the load eccentricity, $e_0 = 4\%$, and the length of the column, L=5 m. The curve?curves of the load bearing capacity coefficient versus temperature for different initial lateral displacements is?are plotted in Figure 5.

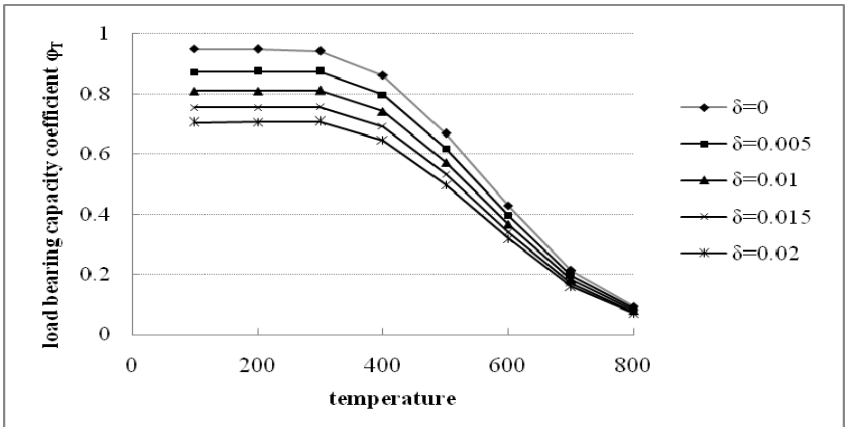

Figure 5. Load Bearing Capacity Coefficient–temperature Curve of the Example Steel Column

Figure 5 illustrates that regardless of the initial lateral displacement, when the temperature is in the range of 100-300°C, the load bearing capacity coefficient remains essentially unchanged; when the temperature exceeds 300°C, the load bearing capacity coefficient decreases notably with increasing temperature. When the temperature reaches 800°C, the bearing capacity coefficient is approximately zero.

3. AXIAL FORCE OF AXIALLY RESTRAINED STEEL COLUMNS AT HIGH TEMPERATURES

3.1 Axial Force of Axially Restrained Steel Columns

If an axially restrained column (e.g., a column in a frame) is heated via a fire, additional axial forces will be produced in the column as a result of thermal expansion; this is schematically illustrated in Figure 6.

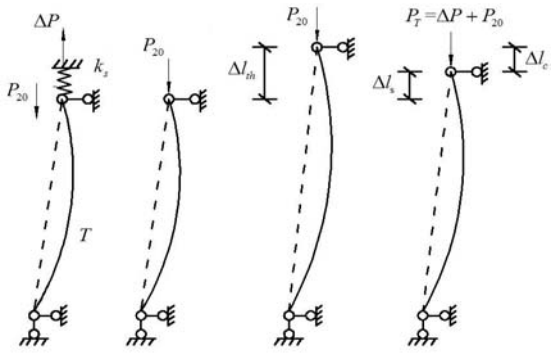

(a) Both ends hinged supported

(b) Both ends rigidly supported

Figure 6. Model of a Restrained Steel Column

As the temperature increases, the overall thermal expansion of the column can be obtained as

$$\Delta l_{th} = \alpha_T (T_1 - T_0) \times L \tag{19}$$

where α_T is the thermal expansion coefficient of the steel columns and T_0 is the normal temperature.

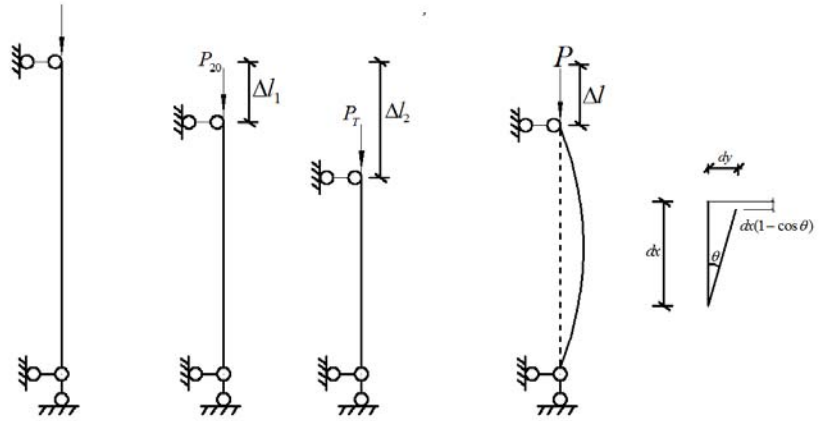

(a) Initial state (b) Compressive state (c) Flexural state

Figure 7. Representation of the Change in the Length of a Column under Compression (b) and bending (c)

At increased temperatures, the column will become shorter because of the decrease in the elastic modulus and the increase in the axial compressive force. In addition, bending will also shorten the length of the column. As illustrated in Figure 7(b), the change in the length of a steel column at two different axial forces and different elastic moduli can be represented as

$$\Delta l_2 - \Delta l_1 = \frac{P_T \times L}{E_T A} - \frac{P_{20} \times L}{EA} \tag{20}$$

As shown in Figure 7(c),

$$\cos\theta = 1 - \frac{1}{2}\theta^2 + \frac{1}{24}\theta^4 + \cdots \approx 1 - \frac{1}{2}\theta^2, \quad \theta = \frac{dy}{dx} = y', \text{ so}$$

$$dx(1-\cos\theta) = (\frac{1}{2})\theta^2 dx = \frac{1}{2}(y')^2 dx \tag{21}$$

Therefore, the change in the length of the column resulting from bending can be represented as

$$\Delta l = \int_0^L (1-\cos\theta)dx \approx \frac{1}{2}\int_0^L (y')^2 dx \tag{22}$$

According to the above formula, the complete shrinkage of the column with initial lateral displacement can be determined by

$$\Delta l_c = \frac{P_T \times L}{E_T A} - \frac{P_{20} \times L}{EA} + \frac{1}{2}\int_0^L [y'(P_T)^2 - y'(P_{20})^2]d_x \tag{23}$$

where P_T is the axial force of the column at increased temperatures and P_{20} is the axial force of the column at room temperature. $y(P_T)$ is the lateral displacement of the column under the action of vertical load P_T. $y(P_{20})$ is the lateral displacement of the column under the action of vertical load P_{20}.

The spring representing the axial restraint will be compressed due to the increase in axial force. The length change of the compressed spring can be given by Hooke's law, i.e.,

$$\Delta l_s = \Delta P / k_s \tag{24}$$

where $\Delta P = P_T - P_{20}$ and k_s is the axial restraint stiffness of the column.

As shown in Figure 7, the following equation can be obtained and employed to determine the axial force in the column at an elevated temperature:

$$\alpha_T (T_1 - 20) \times L = \frac{P_T - P_{20}}{k_s} + \frac{P_T \times L}{E_T A} - \frac{P_{20} \times L}{EA} + \frac{1}{2}\int_0^L [y'(P_T)^2 - y'(P_{20})^2]d_x \tag{25}$$

3.2 Validation of the Axial Displacement via FEM

To verify the equation of axial displacement proposed in the paper, another FEM model (Model 3) is used to validate the axial displacement of the steel columns with increased temperature. The column section is H300×300×8×16, with L=5 m, ξ=0.001 and P_{20}=328 kN. The thermal expansion coefficient is $\alpha=1.4\times10^{-5}$. The spring stiffness is $k_s=0.02\times E_{20}A/L$. Comparisons of the development of the axial displacement obtained using the model proposed in this paper and the FEM method are shown in Figure 8. The axial displacement predictions obtained with the method proposed in this paper correspond well with those obtained by the FEM.

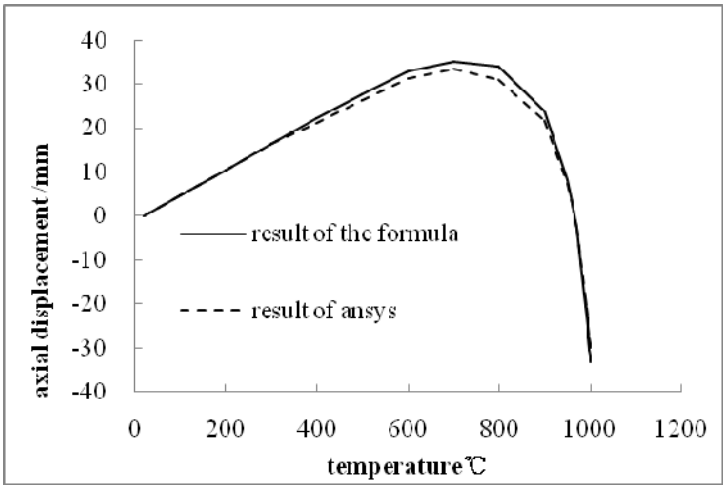

Figure 8. Comparison of the Axial Displacements of a Steel Column with Fixed Ends obtained with ANSYS and the Proposed Approach

3.3 Parametric Analysis

The axially restrained example column with initial lateral displacement is also examined to study the variation of the axial force in the column with increasing temperature. The relationships between the temperature of the column and the axial force in the column with various restraint stiffnesses and load ratios are illustrated in Figure 9; χ is the load ratio and ζ is the axial restraint ratio of the column and are defined as

$$\chi=\frac{P_{20}}{f_{y20}A},\zeta=\frac{k_s}{E_{20}A/L} \tag{26}$$

respectively, where f_{y20} is the yield strength of the steel at a normal temperature.

As shown in Figure 9, the axial force in the column with initial lateral displacement and axial restraint initially increases with increasing temperature. The axial force then decreases to the initial level with increasing temperature, possibly because the steel column has a large flexural deformation when the axial force has been released. When considering the same load ratio, a larger stiffness ratio will cause the axial force to increase further at high temperatures. When considering the same stiffness ratio, a larger load ratio will result in a lower axial force at high temperatures.

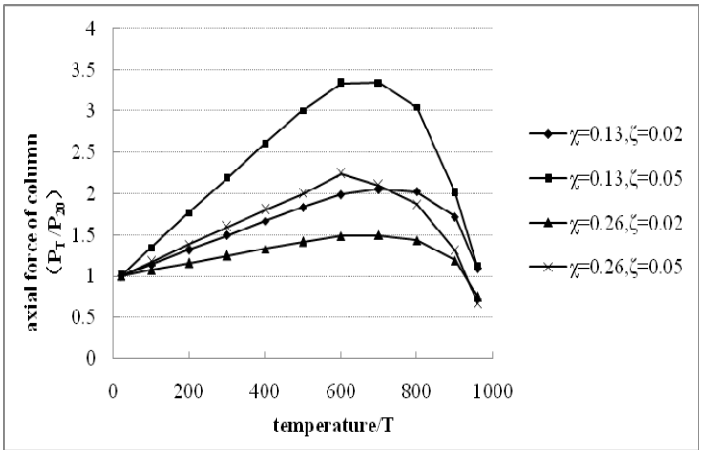

Figure 9. Axial Force in the Steel Column Example

4. CRITICAL TEMPERATURE OF AXIALLY RESTRAINED STEEL COLUMNS

The axial force of steel columns subjected to fire may increase because of the restraint in the thermal elongation. When the axial force reaches the ultimate load bearing capacity in a fire, the column will fail. The critical temperature of the column with initial lateral displacement in a fire is defined as the temperature at which the increasing axial force equals the decreasing ultimate load bearing capacity of the column. For a given steel column, the ultimate load bearing capacity of the column can be calculated by Eq. 8 or Eq. 16. Given a specific restraint stiffness, the axial force of steel columns subjected to a fire can be determined using Eq. 25. The critical temperature of the columns can thus be obtained.

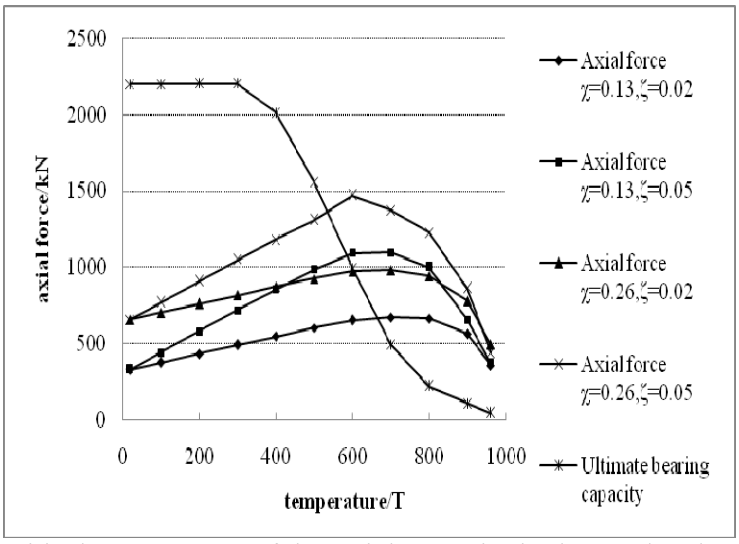

Figure 10. Critical Temperature of the Axial Restraint in the Steel Column Example

Figure 10 shows the critical temperature of both ends of simply hinged supported steel columns with different constraint stiffnesses and load ratios; the figure shows that the critical temperature decreases with increases in the constraint stiffness and load ratio.

5. CONCLUSIONS

Using an experimental approach to predict the fire resistance of a steel column is both time consuming and expensive. As an alternative, theoretical analysis that can be simply performed is a convenient tool for engineers to rapidly evaluate the fire resistance of a column. This paper presented an analytical model to determine the behaviour of restrained steel columns with initial lateral displacement in a fire. The ultimate load bearing capacity and critical temperature of steel columns can be predicted by employing the proposed model. The model can also be used to assess the fire resistance and predict the critical temperature of steel columns with initial lateral displacement.

The following conclusions can be drawn based on the numerical study on a typical steel column with initial lateral displacement:

(1) The load bearing capacity of a steel column with both hinged support sides exposed to a fire decreases linearly at a given temperature with increasing initial lateral displacement. The load bearing capacity will be lower at a higher temperature. The load bearing capacity of a steel column is approximately zero when the temperature reaches 800°C.

(2) The axial force in the axially restrained column with initial lateral displacement initially increases with increasing temperature; once reaching a certain temperature, the axial force may suddenly decrease with increasing temperature.

(3) The critical temperature decreases with an increase in constraint stiffness and the axial force of the steel column at room temperature.

ACKNOWLEDGMENTS

The work presented in this article was supported by the National Natural Science Foundation of China (Grant No. 51178115) and a project funded by the Priority Academic Program Development of Jiangsu Higher Education Institutions.

REFERENCES

[1] Shepherd, P.G. and Burgess, I.W., “On the Buckling of Axially Restrained Steel Columns in Fire”, Engineering Structures, 2011,Vol.33, pp. 2832-2838.

[2] Young, B. and Ellobody, E., “Performance of Axially Restrained Concrete Encased Steel Composite Columns at Elevated Temperatures”, Engineering Structures, 2011, Vol. 33, pp. 245-254.

[3] Li, G.Q. and Zhang, C., “Creep Effect on Buckling of Axially Restrained Steel Columns in Real Fires”, Journal of Constructional Steel Research, 2012, Vol.71, pp.182-188.

[4] Kwon, I.K. and Kwon, Y.B., “Structural Stability of Fire-resistant Steel (FR490) H-section Columns at Elevated Temperatures”, Steel and Composite Structures, 2014, Vol. 17, No.1, pp.105-121.

[5] Wang, W.Y. and Li, G.Q., “Fire-resistance Study of Restrained Steel Columns with Partial Damage to Fire Protection”, Fire Safety Journal, 2009, Vol. 44, pp.1088-1094.

[6] Shahrial, A.M., Muntasir, B.A.H.M., Shahriar, Q., Mahmud, A., Rafi, A.N.M. and Ahmad, R., “Fire Performance Curves for Unprotected HSS Steel Columns”, Steel and Composite Structures, 2013, Vol.15, No.6, pp.705-724.

[7] Della Corte, G., Landolfo, R. and Mazzolani, F.M., "Post-earthquake Fire Resistance of Moment Resisting Steel Frames", Fire Safety Journal, 2003,Vol.38, No.7, pp.593-612.
[8] Della Corte G, De Matteis G, Landolfo R, et al., "Seismic Analysis of MR Steel Frames based on Refined Hysteretic Models of Connections", Journal of Constructional Steel Research, 2002, Vol. 58 No. 10, pp. 1331-1345.
[9] Mohmmad, H.Y., "Post-Earthquake Fire Performance of Building Structures", Concordia University Montreal, Quebec, Canada, 2008.
[10] Ji, L., Zhao, J.H., Zhai, Y. and Li, X.Z., "Effect of Axial Restraint on Fire Resistance Performance of Steel Column", Journal of Architecture and Civil Engineering, 2006, Vol. 23, No.4, pp. 64-69.
[11] Li, G.Q. and Guo, S.X., "Experiment on Restrained Steel Beams subjected to Heating and Cooling", Journal of Constructional Steel Research, 2008, Vol.64, pp.268-274.
[12] Liu, T.C.H., Fahad, M.K. and Davies, J.M., "Experimental Investigation of Behaviour of Axially Restrained Steel Beams in Fire", Journal of Constructional Steel Research, 2002, Vol. 58, pp. 1211-1230.
[13] Rodrigues, J.P.C., Neves, I.C. and Valente, J.C., "Experimental Research on the Critical Temperature of Compressed Steel Elements with Restrained Thermal Elonga- Tion", Fire Safety Journal, 2000, Vol. 35, No. 2, pp. 77-98.
[14] Huang, Z.F. and Tan, K.H., "Analytical Fire Resistance of Axially Restrained Steel Columns", Journal of Structural Engineering, ASCE, 2003, Vol. 129, No. 11, pp.1531-1537.
[15] Li, G.Q. and Guo, S.X., "Analysis of Restrained Heated Steel Beams during Cooling Phase", Steel and Composite Structures, 2009, Vol. 9, No. 3, pp. 191-108.
[16] Ellobody, E. and Young, B., "Investigation of Concrete Encased Steel Composite Columns at Elevated Temperatures", Thin-Walled Structures, 2010, Vol. 48, pp. 597-608.
[17] Wang, Y.C. and Davies, J.M., "Fire Tests of Non-sway Loaded and Rotationally Restrained Steel Column Assemblies", Journal of Constructional Steel Research, 2003, Vol. 59, No.3, pp. 359-383.
[18] Chinese Technical Code on Fire Safety of Steel Building Structures. (CECS200-2006), Beijing (in Chinese), 2006.

Advanced Steel Construction Vol. 14, No. 1, pp. 37-56 (2018)

TRENDS IN THE CODE DESIGN OF STEEL FRAMED STRUCTURES

N.S. Trahair

Emeritus Professor of Civil Engineering
The University of Sydney
(Corresponding author: E-mail: nicholas.trahair@gmail.com)

Received: 3 September 2016; Revised: 13 February 2017; Accepted: 16 February 2017

Abstract: This paper surveys trends in the design of steel framed structures under quasi-static loads with reference to design codes such as the US AISC Specification, the UK BS5950, the Australian AS4100, the European EC3, and the Hong Kong Code of Practice.

The paper provides a brief timeline of the development of steel design codes over the past 80 years, summarises the methods of design now permitted in codes, discusses some of the shortcomings of present codes, and suggests future areas for improvement.

It is concluded that future design codes might allow the use of purpose-built computer programs which can provide accurate predictions of member strength, and might only describe the characteristics of the methods of structural analysis and the member design strengths which may be used. Such a code would have some of the present member strength inaccuracies and shortcomings removed and allow them to be replaced by the use of more accurate advanced analysis computer programs.

Keywords: Analysis, codes, design, frames, steel, structures

DOI: 10.18057/IJASC.2018.14.1.3

1. INTRODUCTION

This paper surveys trends in the design of steel framed structures under quasi-static loads with reference to design codes such as those of the US [1], the UK [2], Australia [3], Europe [4], and Hong Kong [5].

The development of design codes relies heavily on experience and on the theoretical and experimental findings of research studies. The steady and now rapid increase in these has lead to significant expansions in the guidance provided by codes. It is worth noting that an unexpected consequence of these expansions is that it becomes increasingly more onerous to revise and update design codes.

The following sections provide a brief timeline of the development of design codes over the past 80 years, summarises the methods of design now permitted in codes, discusses some of the shortcomings of present design codes, and suggests future areas for improvement.

2. A TIMELINE FOR STEEL DESIGN CODES

Steel design codes in the 1930's were working stress codes in which the member stresses determined by analysing the frame structure under the quasi-static working loads were required to be less than the permissible working stresses set out in the codes. Analysis of all but statically determinate frames (Figure 1) was difficult, because the established methods of indeterminate

analysis were time consuming and error prone for many practical structures. Instead, approximate methods were used such as those which relied on assumed points of contra-flexure to render the structure statically determinate, or the moment distribution method developed by Hardy-Cross. Limited and relatively simple and sometimes empirical approximations were given for the permissible working stresses which made allowances for buckling, initial crookedness, and yielding, and incorporated factors of safety of the order of 2.

Figure 1. A Structure Designed Manually

This situation continued until the 1960's, when plastic analysis and design were permitted. At this time, factors of safety were reduced, and more accurate expressions were used for the permissible working stresses which allowed for a wider range of restraint conditions for beams and columns which fail by buckling. The 1968 predecessor of [3] allowed a method of design by buckling analysis in which the results of analyses for the elastic lateral buckling of beams could be used directly in determining the allowable stresses. Although computers were being used by researchers, they had little impact on designers.

The development of formulations for the permissible working stresses continued until the introduction of limit states design codes in the 1980's and 1990's, in which the analysis and design for strength moved from the working towards the ultimate load level. This required a more careful assessment of stability effects at these higher loads, and more accurate assessments of the strength design capacities of members and connectors.

The 1990 predecessor of [3] contained for the first time a section which distinguished among the different types of analysis that were permitted, including first-order elastic analysis, amplified first-order analysis, second-order elastic analysis, and elastic buckling analysis, as well as plastic analysis. Design methods varied according to the method of analysis used.

The code recognized that designers were increasingly using computer methods of elastic analysis. It also recognized that design strength formulations could become more detailed, because the widespread use of computers would lead to these formulations being programmed, and even linked directly to computer analysis programs.

This predecessor also introduced the concept of advanced analysis, in which the previously separate activities of analysing the structure to determine the member actions and of designing suitable members to resist those actions was replaced by a single analysis of the structure which included all the effects that affect member strength.

Later codes have continued the process of making their member strength formulations more detailed.

3. PRESENT METHODS OF ANALYSIS AND DESIGN

3.1 Methods of Structural Analysis.

In most methods of analyzing frame structures under quasi-static loads, each member is represented as a single line element, and the distribution of forces and moments throughout the frame is determined by using the conditions of static equilibrium and of geometric compatibility between the members at the joints. The way in which this is done depends on whether a frame is statically determinate (in which case the complete distribution of forces and moments can be determined by statics alone), or is statically indeterminate (in which case the compatibility conditions for the deformed frame must also be used before the analysis can be completed).

A statically indeterminate frame can be analysed approximately if a sufficient number of assumptions are made about its behaviour to allow it to be treated as if determinate. One method of doing this is to guess the locations of points of zero bending moment and to assume there are frictionless hinges at a sufficient number of these locations that the member forces and moments can be determined by statics alone.

The accurate analysis of statically indeterminate frames is complicated by the interaction between members: the equilibrium and compatibility conditions and the constitutive relationships must all be used in determining the member forces and moments.

There are a number of different types of analysis which might be made, some of which are discussed in the following sub-sections. These are identified using a set of acronyms which is exemplified by LBA (Linear Buckling Analysis) and GMNIA (Geometrically and Materially Nonlinear Analysis with Imperfections).

3.1.1 First-order elastic analysis (LA)

For some frames, it is common to use a first-order elastic analysis which is based on linear elastic constitutive relationships and which ignores any geometrical non-linearities and associated instability problems (Figure 2). The deformations $\{\Delta_1\}$ determined by such an analysis are related to the applied loads $\{Q\}$ through the linear relationships (Figure 3)

$$[K]\{\Delta_1\}=\{Q\} \tag{1}$$

in which $[K]$ is the stiffness matrix, and so the principle of superposition can be used to simplify the analysis. It is often assumed that axial and shear deformations can be ignored in frames whose actions are predominantly flexural, and that flexural and shear deformations can be ignored in frames whose member forces are predominantly axial.

3.1.2 Elastic buckling analysis (LBA)

However, a first-order elastic analysis will underestimate the forces and moments in and the deformations of a frame when instability effects are present. Some estimate of the importance of these can be obtained by making an elastic buckling analysis of the frame according to

$$\{\Delta_b\}^T [K - \lambda_0 G]\{\Delta_b\} = 0 \tag{2}$$

in which λ_0 is the buckling load factor and $[G]$ is the stability matrix for the initial forces.

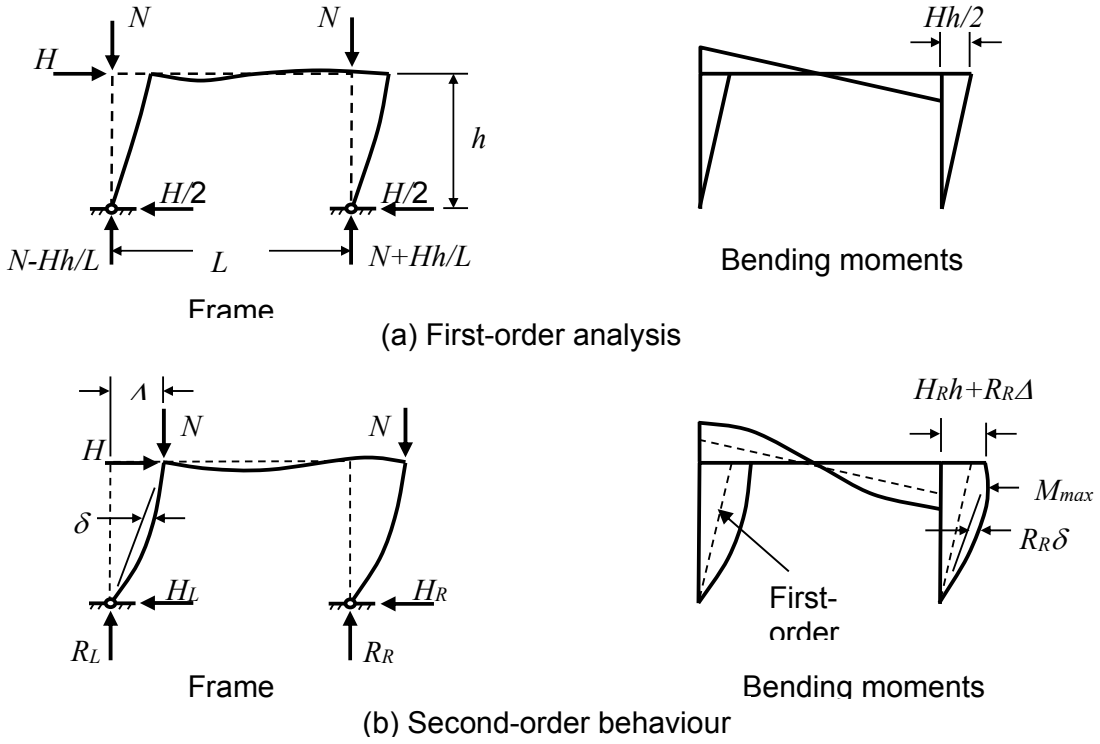

Figure 2. First-order Analysis and Second-order Behaviour

3.1.3 Amplified first-order elastic analysis

More generally, the effects of instability must be allowed for, and as a first approximation the results of an elastic first-order analysis may be amplified by using factors derived from the frame elastic buckling loads (Figure 3), so that

$$\{\Delta_{1a}\} = \{\Delta_1\}/(1\text{-}1/\lambda_0) \tag{3}$$

3.1.4 Second-order elastic analysis (GNA)

A more accurate allowance for the effects of instability may be made by using an elastic second-order elastic analysis (Figures 2, 3), in accordance with

$$[K\text{-}G]\{\Delta_2\}=\{Q\} \tag{4}$$

While some codes [1, 3] allow second-order analyses to be made of the nominal frame (GNA), others [4, 5] require the effects of geometrical imperfections, residual stresses, and spread of plasticity to be allowed for approximately by using equivalent geometrical imperfections $\{\Delta_i\}$ (GNIA). The shape of these is usually taken to be the same as that of the lowest elastic buckling mode $\{\Delta_b\}$ [6], while the magnitude α_i is defined in the code, so that

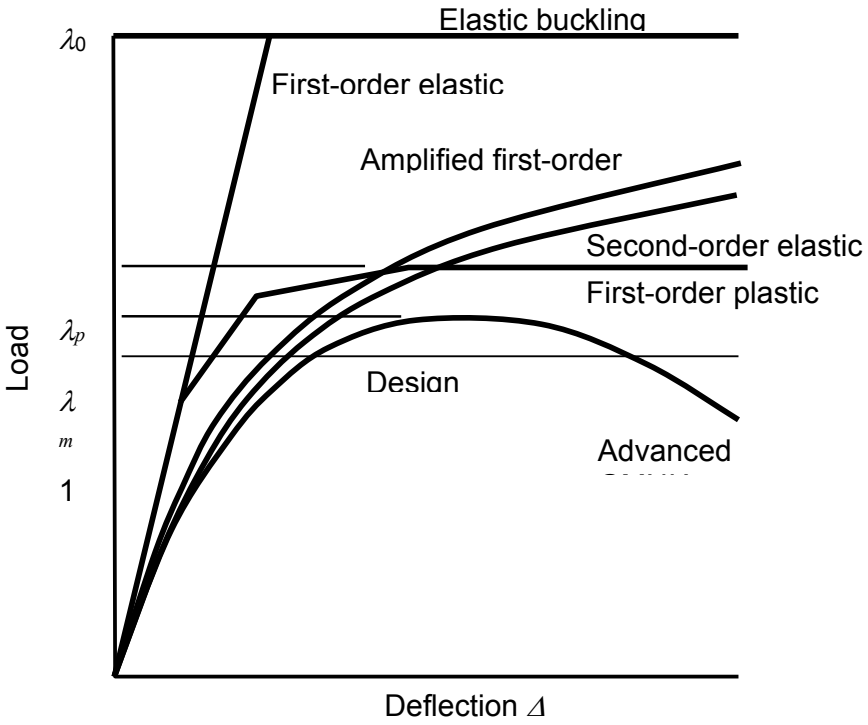

Figure 3. Methods of Analysis

$$\{\Delta_i\}=\alpha_i \{\Delta_b\} \tag{5}$$

It is often convenient to replace these equivalent imperfections by equivalent (or notional) loads

$$\{Q_i\}=[K]\{\Delta_i\} \tag{6}$$

which induce first-order deformations equal to the imperfections, whence

$$[K\text{-}G]\{\Delta_{2i}\}=\{Q+Q_i\} \tag{7}$$

3.1.5 Plastic analysis (MNA)

The analysis of statically indeterminate frames near the ultimate load is further complicated by the decisive influence of the material non-linearities. Many two-dimensional (2D) frames have very small axial forces and instability effects, in which case it is comparatively easy to use a first-order plastic hinge analysis, according to which a sufficient number of plastic hinges must form to transform the frame into a collapse mechanism (Figure 3). The computational efficiency of the plastic hinge method is enhanced when the effects of geometrical non-linearities can be accurately allowed for by using one element per member [7, 8] (GMNA). Some attempts have been made to extend these plastic hinge methods to allow for semi-rigid rather than rigid joints between members [9, 10].

Plastic zone analyses of 2D frames for which local and lateral buckling are prevented may allow for geometric (in-plane instability) and material (yielding) non-linearities, residual stresses, and geometrical imperfections, and account for the spread of the yielded zones through the cross-

sections and along the members of the frames [9 – 11]. However, while this method is extremely accurate, it is computationally comparatively complex, wasteful, and slow. Plastic zone methods have been used to develop benchmark solutions for testing the more efficient but less accurate plastic hinge methods [13 – 17], in which yielding effects are concentrated at a few cross-sections, and residual stress and geometrical imperfection effects are approximated by using reduced stiffnesses.

The plastic hinge method is simpler to use and computationally much more efficient than the plastic zone method. The results of the two methods are similar, except when the bending moment is nearly uniform with a wide spread of plasticity. In most practical cases, the plastic hinge method is considered to be adequate.

3.1.6 Advanced analysis (GMNIA)

In advanced analysis [12, 13, 18], the previously separate activities of analysing the frame to determine the line element member actions and of designing suitable members to resist those actions is replaced by a single analysis of the frame which includes all those effects that affect member strength such as local and lateral buckling, geometrical imperfections, residual stresses, and inelastic behaviour. It is then only necessary for the frame to reach a stable equilibrium position under the design loads (increased by incorporating a frame capacity factor) for it to be deemed satisfactory (Figure 3).

For 2D frames for which local and lateral buckling are prevented, plastic hinge analyses which take account of in-plane stability and equivalent imperfections are equivalent to advanced analyses.

As originally envisaged, advanced analysis of steel frames was expected to be carried out by using line elements to represent the members. More generally, however, advanced analysis may also be carried out by modeling the members as assemblages of plate or shell elements, even though the greatly increased number of elements requires increased computer speeds and storage to be viable.

3.1.7 Quasi advanced analysis for local and out-of-plane buckling

There are a number of quasi advanced methods for the analysis of 2D frames with 2D loading which include the effects of strength reductions due to local and out-of-plane buckling. Quasi advanced methods use 2 stages instead of the single analysis stage of a true advanced analysis. First an advanced in-plane analysis is made of the frame which omits the effects of local and out-of-plane buckling. For the second stage, the local and out-of-plane member strengths are checked by using either the code formulations (which conservatively ignore interactions between members) or more accurate analyses of the buckling strengths, if available.

Quasi advanced analyses are comparatively efficient when only a few line elements per member are needed for the in-plane analysis, since the larger number of elements required for accurate determinations of the local and out-of-plane strengths are avoided.

3.2 Methods of Design

3.2.1 Design by code formulations

Present code methods of design provide formulations of the design strengths which are used to check the adequacy of the members and connections to resist the actions determined by the analysis

of the frame. Of necessity, these are often limited in their application to the most common examples such as members of doubly symmetric cross-section. In some cases, the formulations (for beam-columns) are extremely complicated [4], while in others they are very simple [1].

3.2.2 Design by elastic buckling analysis

Some design codes [2, 3, 5] give advice on the effects of moment distribution, load height, and elastic restraints on the elastic lateral buckling of beams which is sometimes of somewhat doubtful accuracy, especially with respect to the effects of load height, while all codes are limited in the amount of advice on elastic buckling that they can give. This difficulty is avoided in [3], which explicitly allows the alternative method of design by elastic buckling analysis [19] in which accurate values of the elastic buckling moment M_0 are used directly in the design process to determine the nominal design capacity M_d. This allows computer programs such as PRFELB [20, 21] to be used to obtain accurate values of the elastic buckling moment M_0 which account properly for the effects of moment distribution, load height and end restraints.

In [3], the lateral buckling design of beams is founded on a basic beam design curve which reduces the elastic buckling moment M_{0u} of a simply supported beam in uniform bending. This is achieved by using slenderness reduction factors

$$\alpha_s = 0.6\left\{\sqrt{\left[\left(\frac{M_s}{M_{0u}}\right)^2 + 3\right]} - \left(\frac{M_s}{M_{0u}}\right)\right\} \tag{8}$$

in which M_s is the section moment capacity, which were determined using the results of tests on full-scale members with practical values of residual stress and geometric imperfections [19].

In the method of design by elastic buckling analysis, the actual elastic buckling moment M_0 is substituted for the value M_{0u} for a simply supported beam in uniform bending. However this method is conservative because it does not allow for the effects of the moment distribution on inelastic buckling. This is compensated for in [3] by using a moment modification factor

$$\alpha_m = M_{0s} / M_{0u} \tag{9}$$

in which M_{0u} is the elastic buckling moment of a beam which is unrestrained against lateral rotation and loaded at the shear centre. The nominal design capacity is then determined from

$$M_d = \alpha_m \alpha_s M_s \le M_s \tag{10}$$

The method of design by buckling analysis is demonstrated in Figure 4 for the example of the lateral buckling of simply supported beams under moment gradient.

The European code [4] gives no advice on elastic lateral buckling, but requires the direct use of M_0 in the design process. This implicitly requires the use of the method of design by buckling analysis. The method of design by elastic buckling analysis is also required by [4] for the design of compression members, while [3] allows this method to be used for non-uniform compression members.

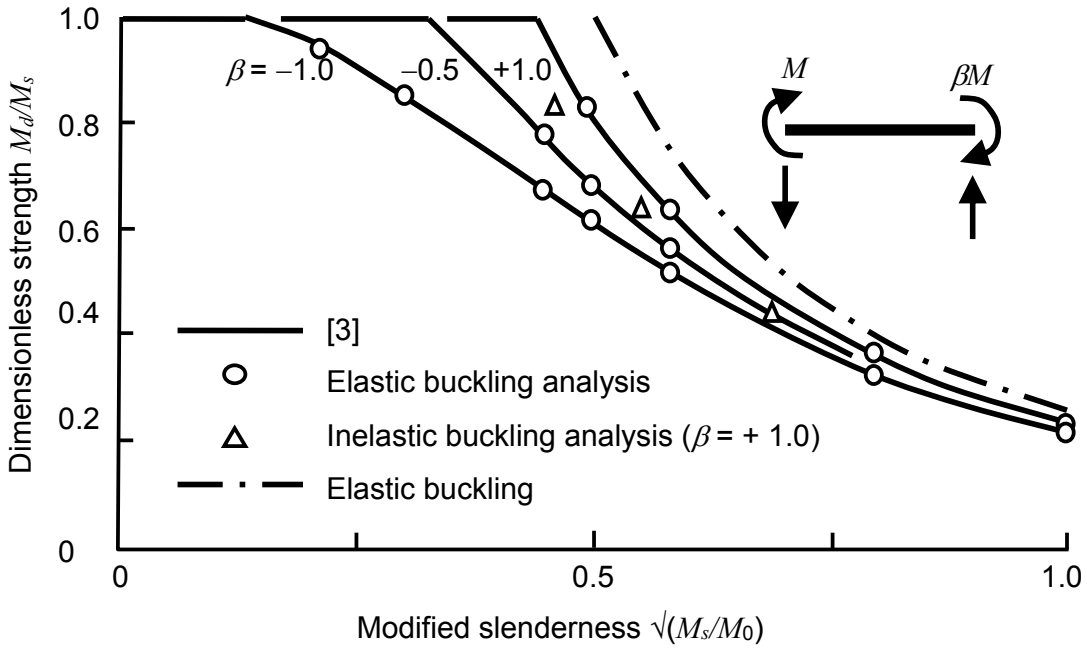

Figure 4. Buckling Strengths of Beams under Moment Gradient

The method of design by elastic buckling analysis is also used as the Direct Strength Method for the design of cold-formed steel members against local buckling, distortional buckling [22], and flexural, torsional and flexural-torsional member buckling in [23, 24].

3.2.3 Out-of-plane design by inelastic buckling analysis

In the code method of out-of-plane design by elastic buckling analysis, the results of an elastic buckling analysis which incorporates the effects of non-uniform bending, load height, and elastic restraints are used in determining slenderness reduction factors, which also make allowance for the effects of residual stresses and geometrical imperfections. However, this method does not allow for the local effects of non-uniform yielding on the inelastic lateral buckling resistance.

The inelastic out-of-plane buckling resistance of a beam under non-uniform bending is significantly affected by local reductions in the out-of-plane stiffnesses in the high moment regions of the beam where yielding takes place. Because the moment distribution varies, so do the stiffnesses, and the beam becomes non-uniform. To analyse this, account must be taken of the distribution of the elastic and inelastic regions both in the cross sections as well as along the beam.

One way to achieve this is to use the method of member strength design by inelastic buckling analysis [25] in which an elastic buckling analysis is carried out which allows for the local effects of non-uniform yielding on the out-of-plane stiffnesses by using reduced moduli γE, γG [26]. The advantage of the method is that finite element buckling analysis programs such as PRFELB [20, 21] may be used directly without empirical adjustments of the results.

This method has been tested against code formulations [3] for the lateral buckling strengths of beams under moment gradient, beams with central concentrated loads acting away from the shear centre, and beams with elastic end restraints [25]. It has also been used for columns, beam-columns [25], frames [7], and cantilevers [28].

It has also been used in conjunction with the [1] formulations for column and beam strengths and brace stiffnesses [29, 30].

Extensive calibrations of this method against advanced analyses of the inelastic buckling strengths of beam, columns, and beam-columns have been made [31 – 34]. It has been anticipated [35] that this method will be incorporated in a future edition of [4].

The reduced elastic moduli γE, γG used in the elastic buckling analysis to determine a reduced buckling moment M_{0r} are derived from the nominal lateral buckling design strengths M_d for simply supported beams in uniform bending, and so include allowances for the effects of yielding, residual stresses and geometrical imperfections. For beams in uniform bending, the resultant reduced moments M_{0r} are equal to the design moments M_d.

The reduced moduli decrease as the bending moment increases (Figure 5), and so when they are applied to beams with non-uniform moment distributions, there are greater reductions in the high moment regions and smaller or no reductions in the low moment regions. The method thus takes account of the effect of the moment distribution on inelastic lateral buckling.

The results of using the method of design by inelastic buckling analysis has been used to determine the nominal [3] design strengths $M_d = M_{0r}$ of simply supported beams under moment gradient are shown in Figure 4.

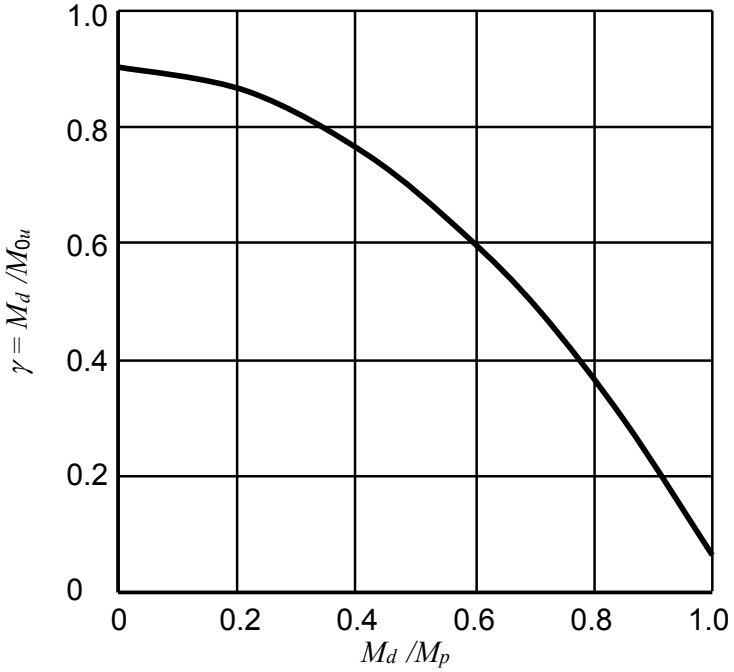

Figure 5. Reduced Elastic Moduli Factors

3.2.4 Design by advanced analysis

When using advanced analysis, the design criterion may be expressed as

$$\lambda_m \geq 1/j_s \tag{11}$$

where λ_m is the maximum value of the load factor at failure (Figure 3) determined by repeated analysis and j_s is the system resistance factor (equivalent to the frame capacity factor) which may be obtained from a reliability analysis of the structural system. In the design situation where the design loads are known ($\lambda = 1$ in Figure 3), this criterion further simplifies to the frame being satisfactory when the advanced analysis shows that the frame is in equilibrium under the load set defined by $\lambda = 1 / j_s$, which obviates the repeated analysis needed to determine λ_m

In the original formulation for design by advanced analysis [3], the analysis is carried out at the design load level ($\lambda = 1$) and the frame is satisfactory if none of the design member section and connection capacities are exceeded. This method provides an approximate alternative to using the system resistance factor j_s.

Research has been conducted in recent years to determine system resistance factors j_s for 2D steel frames with compact cross-sections [36] and cold-formed steel frames with slender cross-sections [37], suggesting that the system resistance factor j_s typically lies in the range 0.8-0.9 depending on the structural system and target reliability. Design by advanced analysis provisions were included in the 2012 revision of the Australian Standard for rack structures [38] and have been implemented in the current draft of the revised Australian Cold-formed Steel Structures Standard [23]. Design by advanced analysis is also permitted in Appendix 1 of the AISC Specification [1], where the system resistance factor j_s is implicitly incorporated by reducing the yield stress F_y and stiffness E by a factor of 0.9. A justification of this approach is given in [39].

4. SHORTCOMINGS IN CODE METHODS OF DESIGN

4.1 Local Buckling Strength

Code rules for local buckling strength are usually based on the behaviour of isolated plates, and while there are some approximations for allowing for the increased strengths that arise when the critical plate elements are restrained by others in the member cross-section, these are of somewhat doubtful accuracy.

4.2 Compression Members

While some code formulations of compression member strength already incorporate the results of elastic buckling analyses, there are many important situations that are not catered for, and so codes are generally inadequate in the advice that they give.

In some codes, the possibility of torsional or flexural-torsional buckling of compression members [40] is not covered directly. For example, cruciforms may fail torsionally, while angles, tees and some channels are susceptible to flexural-torsional buckling. While the method of design by elastic buckling analysis in some codes allows the actual elastic buckling load to be used directly, this may sometimes lead to strength predictions which are overly conservative, as shown in Figure 6 [41].

Compression members are frequently braced eccentrically (Figure 7) or in planes which are inclined to their principal planes, leading to flexural-torsional buckling [42]. The method of design by elastic buckling analysis may also be used in these cases.

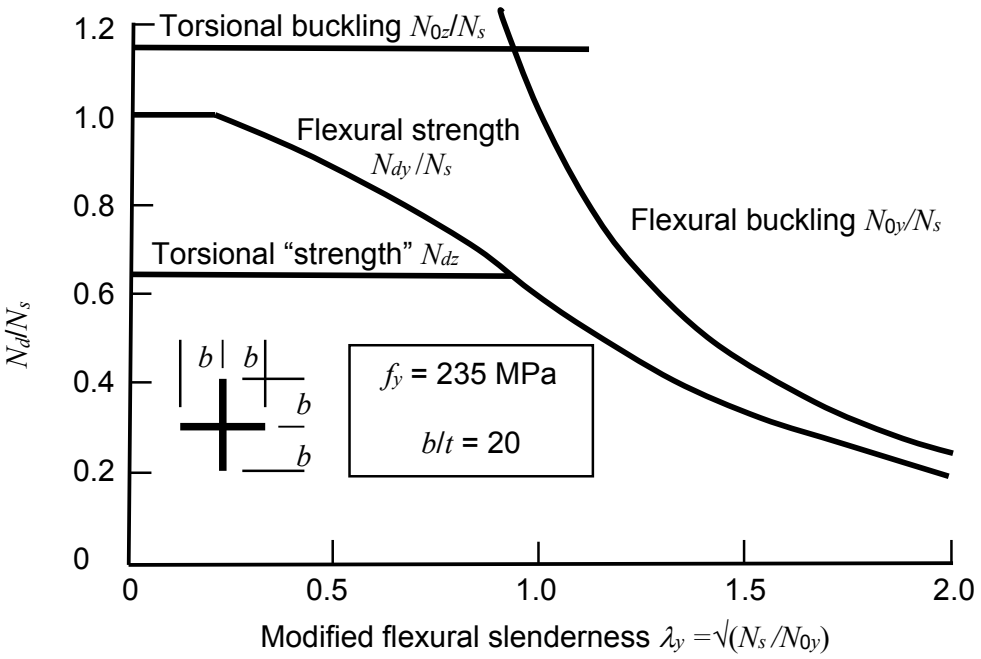

Figure 6. Design of Cruciform Columns [4]

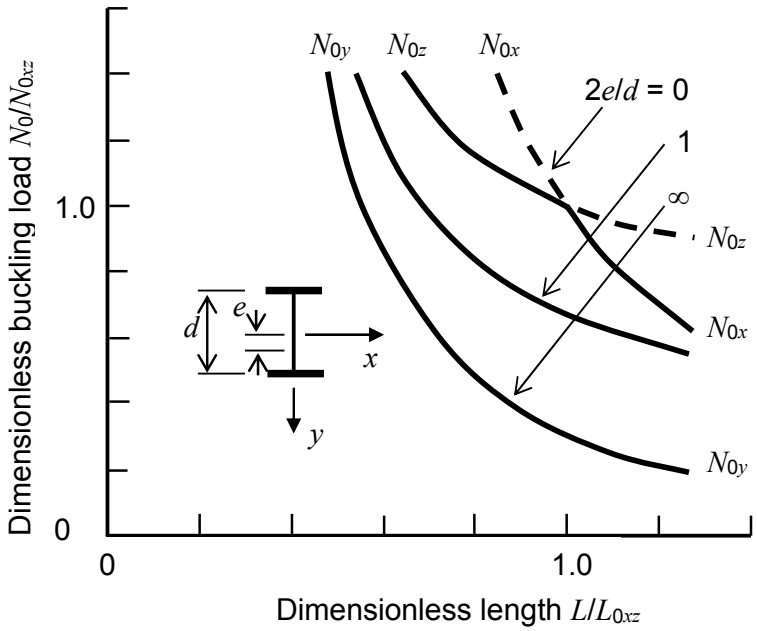

Figure 7. Buckling of Columns with Eccentric Central Restraints

Another shortcoming of some design codes is that they define rigid tolerances on compression member crookedness which prevent the use of overly crooked members (Figure 8), even when they are lightly loaded [43].

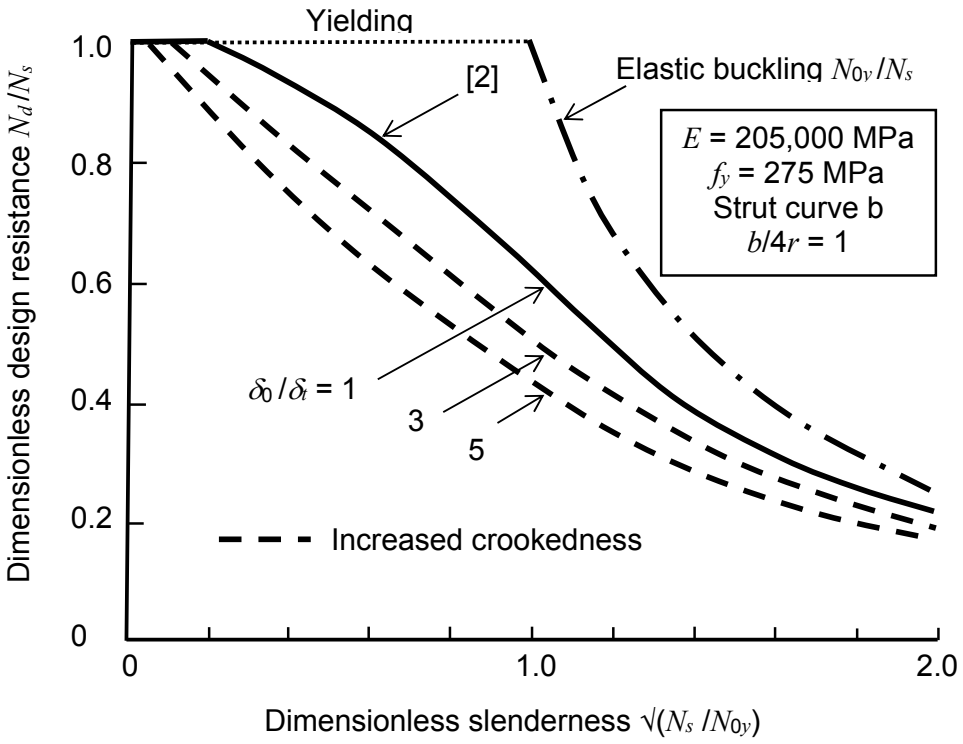

Figure 8. Design Resistances of Out-of-tolerance Columns

4.3 Beams

Guidance given by codes for designing beams against lateral buckling is limited, extremely variable, and mainly based on the behaviour of doubly symmetric I-beams, which may be overly conservative for other beams such as rectangular hollow sections [44, 45], as shown in Figure 9.

There are a number of common effects that modify the strength, including the geometry, the moment distribution, the load height above the shear centre, and elastic restraints [40]. More consistent designs may be achieved by using the method of design by elastic buckling analysis, but this method alone does not allow for the strengthening effects of moment gradient on inelastic buckling (Figure 4). While some codes do make allowance for these, they are often unnecessarily conservative [4].

Guidance given for the design of monosymmetric I-beams under moment gradient is often inaccurate, both in the elastic and the inelastic buckling ranges, as indicated in Figure 10 [46].

The effects of distortion on the strength of beams with slender webs are rarely covered, although the method of design by elastic buckling analysis has been used by substituting the elastic lateral-distortional buckling load for the elastic lateral buckling load. Distortion effects become important in continuous under-slung monorails, where the bottom flange cannot be restrained at intermediate supports, as shown in Figure 11 [47].

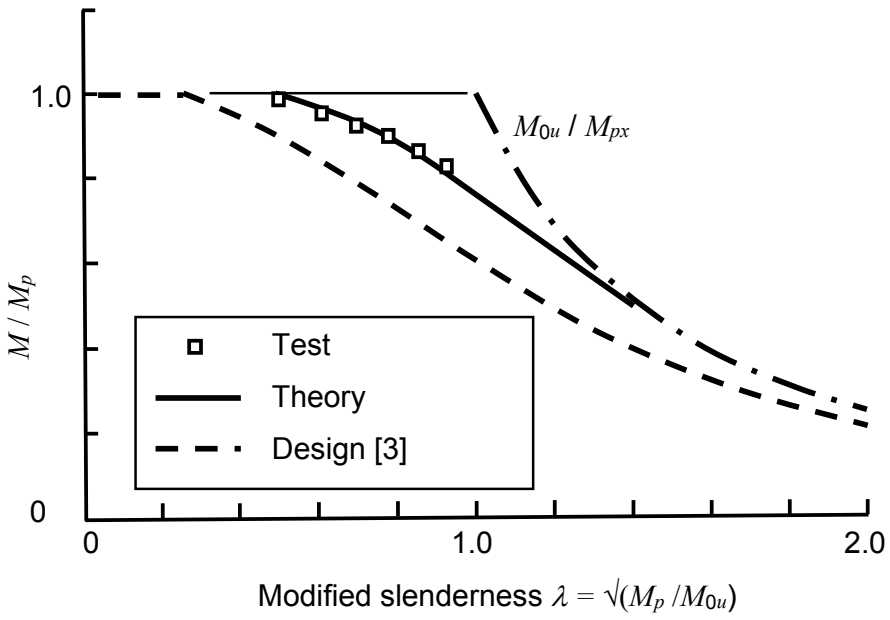

Figure 9. Lateral Buckling Strengths of RHS

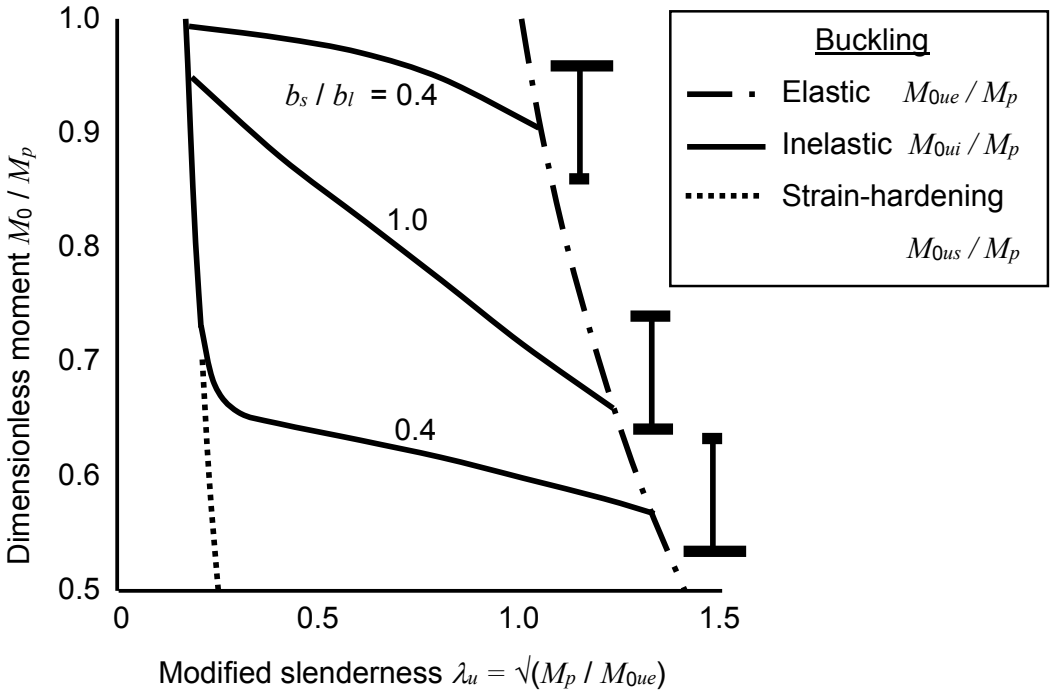

Figure 10. Inelastic buckling of monosymmetric beams – uniform bending

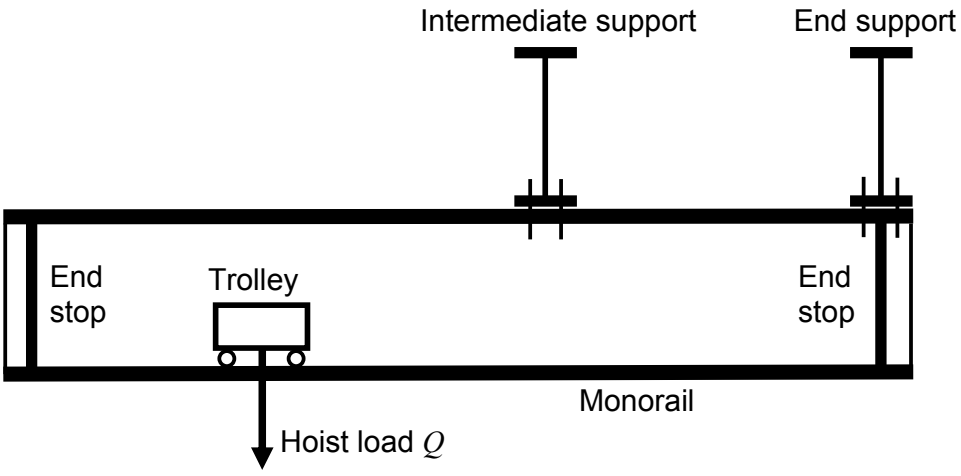

Figure 11. Overhanging Monorail

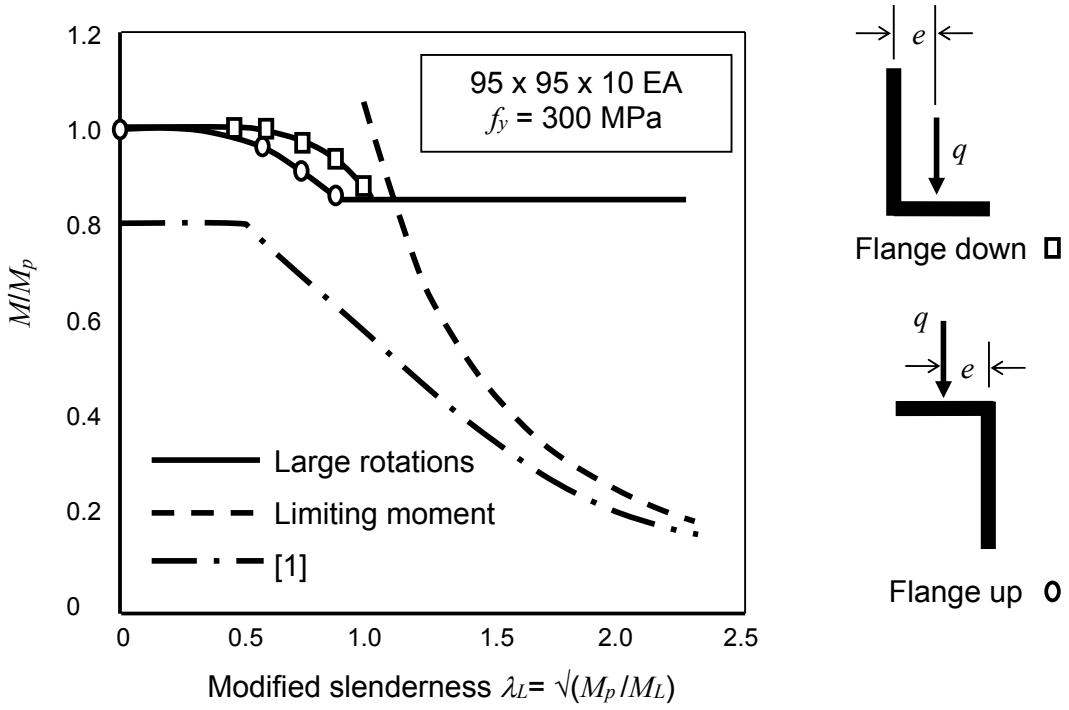

Figure 12. Uniformly Loaded Equal Angle Lintel

Angle section beams are frequently loaded in biaxial bending and torsion, but code rules do not adequately reflect this behaviour, and may give rise to variable strength predictions, as shown in Figure 12 [48].

4.4 Beam-Columns

The variety of different formulations for beam-column strength [1, 4] suggests that there is a corresponding lack of accuracy in their predictions of strength. Some code formulations are excessively complicated, so that manual implementation is tedious and error prone.

4.5 Biaxial Bending and Torsion

Torsion and combined bending and torsion is largely neglected in steel design codes, even though there is a considerable body of knowledge of the former [19], and some research studies [49] of the latter.

4.6 Arches and Curved Girders

The design of arches [50 – 54] and of members curved in plan [55] is not treated in design codes.

5. FUTURE TRENDS

5.1 Computer Hardware

Future analysis and design methods will be greatly influenced by further development of computer hardware and software. The expansion of storage capacity and increase in speed will allow more sophisticated structural analyses to be made of even larger structures, and will facilitate the efficient application of increasingly more complex code advice on member design. Improvements in computer speed and storage are leading to practical methods of advanced analysis for a much wider range of applications than has been the case.

At the same time there will be further developments in user-friendly pre- and post-processors for the input of data and the display of results, while there will be even greater linking of computer programs for analysis, design [56], detailing, shop drawing and manufacture. However, there will be an even stronger need for checking procedures, since data errors will propagate through linked programs (Figure 13).

5.2 Methods of Analysis

5.2.1 Advanced analysis

There have been a number of attempts to extend the method of advanced analysis of 2D frames with 2D loading to include the effects of out-of-plane and local buckling [37].

The accurate prediction of the out-of-plane strength requires the use of a finite element analysis which accounts for elastic buckling, yielding, initial crookedness, and residual stresses. The elements must be comparatively closely spaced with consequent rises in computer storage and speed requirements.

The accurate prediction of local buckling effects must account also for out-of-flatness and for post-buckling behavior. The elements must be even more closely spaced than for out-of-plane strength.

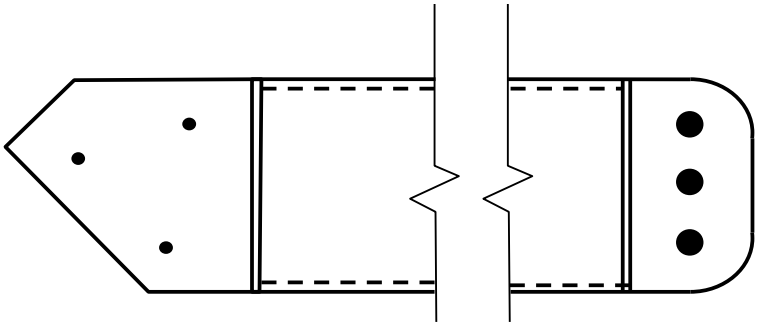

Figure 13. Computer Transmission of Errors

Advanced analysis methods which replace the member line elements with closely spaced plate or shell elements may account for all combined effects on member strength which have been difficult to represent.

5.2.2 Analysis of biaxial bending and torsion.

Methods of analysing biaxial bending and torsion are generally limited to first-order elastic analyses, and many of these omit the strengthening effects of warping torsion in open section members. Further difficulties arise when second-order effects must be allowed for.

5.3 Methods of Design

The accurate prediction of local buckling effects on member strength requires the same use of a finite element analysis as that described above for advanced analysis. Again, the elements must be closely spaced with consequent sharp rises in computer storage and speed requirements.

Torsion and combined bending and torsion are largely neglected in steel design codes, while the design of arches and members curved in plan is not treated.

6. CONCLUSIONS

This paper surveys trends in the design of steel framed structures under quasi-static loads with reference to design codes such as those of the US [1], the UK [2], Australia [3], Europe [4], and Hong Kong [5].

The past 80 years have seen substantial developments in analysis and design, many of which have been empowered by the development and application of computers. Working stress design has been replaced by limit states design, and second-order and advanced methods of analysis and design have been introduced, while code strength formulations have become increasingly detailed as they incorporate more and more research findings.

At present, methods of advanced analysis using line elements in which a single stage of analysis and design replace the separate stages of computer analysis and code strength design are largely restricted to 2D frames with 2D loading for which local and out-of-plane buckling are prevented.

However, the Australian Standard AS4084 [38] for steel storage racks allows design by advanced analysis of rack structures subject to local, distortional and flexural-torsional buckling.

Quasi advanced analyses use advanced analysis of the in-plane behaviour, and code formulations for local and member out-of-plane buckling strengths. In the meantime, the adoption of the method of design by inelastic buckling analysis will allow the comparative inaccuracy of some code out-of-plane strength formulations to be bypassed.

There are a number of design code shortcomings that can be expected to be rectified in the future as more research is carried out. These include the needed for multiple beam curves for different sections such as angles, rectangular hollow sections, and monosymmetric I-sections. Further improvements are needed in the specification of beam-column strength and in the treatment of flexural-torsional buckling of columns. Situations not catered for in design codes include biaxial bending and torsion, and arches and curved girders.

A possible solution to these problems is to allow the use of purpose-built computer programs which can provide accurate predictions of member strength. Thus future design codes might only describe the characteristics of the methods of structural analysis and those of determining the design strengths of structural members which may be used. Such a code would have all the inaccuracies and shortcomings of approximating the member strengths removed and replaced by more accurate member strength computer programs.

This is already partially in place with the present practice of some codes which either allow or require design by elastic buckling analysis. An increased use of advanced finite element programs which use plate or shell elements can be anticipated.

REFERENCES

[1] American Institute of Steel Construction, “Specification for Structural Steel Buildings”, 2010.
[2] British Standards Institution, “BS5950: Part 1:2000, Structural Use of Steelwork in Building, Part 1, Code of Practice for Design in Simple and Continuous Construction: Hot Rolled Sections”, 2000.
[3] Standards Australia, “AS4100, Steel Structures”, 1998.
[4] British Standards Institution, “Eurocode 3: Design of Steel Structures: Part 1.1 General Rules and Rules for Buildings, BS EN 1993-1-1”, 2005.
[5] The Government of the Hong Kong Special Administrative Region, Buildings Department, “GHKSAR, Code of Practice for the Structural Use of Steel”, 2011.
[6] Kindmann, R. and Kraus, M., “Steel Structures Design Using FEM, Ernest and Sohn”, 2011.
[7] Chan, S.L. and Zhou, Z.H., “Second-order Elastic Analysis of Frames using Single Imperfect Element per Member”, Journal of Structural Engineering, ASCE, 1995, Vol. 121, No. 6, pp. 939-45.
[8] Chan, S.L. and Zhou, Z.H., “Nonlinear Integrated Design and Analysis of Skeletal Structures”, Engineering Structures, 2000, Vol. 22, No. 3, pp. 246-57.
[9] Chan, S.L., “Inelastic Post-buckling Analysis of Tubular Beam-columns and Frames”, Journal of Engineering Structures, 1989, Vol. 11, pp. 23-30.
[10] Nethercot, D.A., “Frame Design Incorporating Semi-rigid Effects”, Steel Construction (South Africa), 1994, Vol. 18, No. 6, pp. 24-7.

[11] Ho, W.M.G. and Chan, S.L., "An Accurate and Efficient Method for Large Deflection Analysis of Frames with Semi-rigid Connections", Journal of Constructional Steel Research, 1993, Vol. 26, pp. 171-191.
[12] Clarke, M.J., "Plastic-zone Analysis of Frames", Advanced Analysis of Steel Frames : Theory, Software, and Applications, Chen, WF, and Toma, S, eds, CRC Press, 1994, Chapter 6, pp. 259-319.
[13] White, D.W. and Chen, W.F. (editors), "Plastic Hinge Based Methods for Advanced Analysis and Design of Steel Frames", Structural Stability Research Council, 1993.
[14] Liew, J.Y.R., Chen, H., and Chen, W.F., "Second-order Refined Plastic Hinge Analysis of Frame Design. Parts I and II", Journal of Structural Engineering, ASCE, 1993, Vol. 119, No. 11, pp. 3196-3216, 3217-3237.
[15] Yau, C.Y. and Chan, S.L., "Inelastic and Stability Analysis of Flexibly Connected Steel Frames by the Springs-in-series Model", Journal of Structural Engineering, ASCE, 1994, Vol. 120, No. 10, pp. 2803-2819.
[16] Chan, S.L. and Chui, P.P.T., "Non-linear Static and Cyclic Analysis of Semi-Rigid Steel Frames", Elsevier Science, 2000.
[17] Liew, J.Y.R., Chen, H., Shanmugam, N.E. and Chen, W.F., "Improved Non-linear Plastic Hinge Analysis of Space Frame Structures", Engineering Structures, 2000, Vol. 22, No. 10, pp. 1324-38.
[18] Chen, W.F. and Kim, S.E., "LRFD Steel Design Using Advanced Analysis", CRC Press, 1997.
[19] Trahair, N.S., Bradford, M.A., Nethercot, D.A. and Gardner, L., "The Behaviour and Design of Steel Structures to EC3", Taylor and Francis, 2008.
[20] Papangelis, J.P., Trahair, N.S. and Hancock, G.J., "Computer Analysis of Elastic Flexural-Torsional Buckling", Journal of the Singapore Structural Steel Society, 1993, Vol. 4, No.1, pp. 59-67.
[21] Papangelis, J.P., Trahair, N.S. and Hancock, G.J., "Elastic Flexural-torsional Buckling of Structures by Computer", Computers and Structures, 1998, Vol. 68, pp. 125-137.
[22] Hancock, G.J., Kwon, Y.B. and Bernard, E.S., "Strength Design Curves for Thin-Walled Sections Undergoing Distortional Buckling", Journal of Constructional Steel Research, 1994, Vol. 31, 2-3, pp. 169-86.
[23] Standards Australia, "SA/NZS AS4600, Cold-Formed Steel Structures, 2005.
[24] American Iron and Steel Institute, "AISI S100-07 W/S2-10 - North American Specification For The Design Of Cold-Formed Steel Structural Members", 2007.
[25] Trahair, N.S. and Hancock, G.J., "Steel Member Strength by Inelastic Lateral Buckling", Journal of Structural Engineering, ASCE, 2004, Vol. 130, No. 1, pp. 64 – 69.
[26] Trahair, N.S. and Chan, S.L, "Out-of-plane Advanced Analysis of Steel Structures", Engineering Structures, 2003, Vol. 25, No. 13, pp. 1627 - 1637.
[27] Trahair, N.S, "Buckling Analysis Design of Steel Frames", Journal of Constructional Steel Research, 2009, Vol. 65, No. 7, pp. 1459-63.
[28] Trahair, N.S, "Steel Cantilever Strength by Inelastic Lateral Buckling", Journal of Constructional Steel Research, 2010, Vol. 66, Nos. 8-9, pp. 993-9.
[29] Togay, O., Jeong, W.Y., Bishop, C.D. and White, D.W., "Towards a More Comprehensive Approach for Design Using Buckling Analysis", Proceedings, Annual Stability Conference, SSRC, 2015.
[30] White, D.W, Jeong, W.Y. and Togay, O., "Comprehensive Stability Design of Steel Members and Systems via Inelastic Buckling Analysis", Proceedings, 8th International Symposium on Steel Structures, 2015.
[31] Kucukler, M., Gardner, L. and Macorini, L., "A Stiffness Reduction Method for the in-plane Design of Structural Steel Elements", Engineering Structures, 2014, Vol.73, pp. 72–84.

[32] Kucukler, M., Gardner, L. and Macorini, L., "Lateral–torsional Buckling Assessment of Steel Beams through a Stiffness Reduction Method", Journal of Constructional Steel Research, 2015, Vol. 109, pp. 87–100.
[33] Kucukler, M., Gardner, L. and Macorini, L., "Flexural-torsional Buckling Assessment of Steel Beam-columns through a Stiffness Reduction Method", Engineering Structures, 2015, Vol. 101, pp. 662-676.
[34] Kucukler, M., Gardner, L. and Macorini, L., "In-plane Design of Steel Frames through a Stiffness Reduction Method", Journal of Constructional Steel Research, 2015.
[35] Gardner, L., "Design of Steel Structures to Eurocode 3 and Alternative Approaches", Proceedings, International Symposium on Advances in Steel and Composite Structures, 2015, pp. 39-51.
[36] Shayan, S., "System Reliability-Based Design Of 2D Steel Frames By Advanced Analysis", PhD Thesis, School of Civil Engineering, University of Sydney, 2014.
[37] Cardoso, F.S., "System Reliability-Based Criteria for Designing Cold-Formed Steel Structures By Advanced Analysis", PhD Thesis, School of Civil Engineering, University of Sydney, 2016.
[38] Standards Australia, "AS4084, Steel Storage Racking", 2012.
[39] Zhang, H. and Rasmussen, K.J.R., "System-Based Design For Steel Scaffold Structures Using Advanced Analysis", Journal of Constructional Steel Research, 2013, Vol. 89, pp. 1–8.
[40] Trahair, N.S., "Flexural-Torsional Buckling of Structures", E and F N Spon, 1993.
[41] Trahair, N.S., "Strength design of cruciform steel columns", Engineering Structures, 2012, Vol. 34, pp. 307-313
[42] Trahair, N.S. and Rasmussen, K.J.R., "Flexural-torsional Buckling of Columns with Oblique Eccentric Restraints", Journal of Structural Engineering, ASCE, 2005, Vol. 131, No. 11, pp. 1731 – 7.
[43] Trahair, N.S. and Kayvani, K., "Capacities of Steel Columns with Excessive Crookedness", The Structural Engineer, 2006, Vol. 84, No. 4, pp. 37-41.
[44] Zhao, X.-L., Hancock, G.J. and Trahair, N.S., "Lateral Buckling Tests of Cold-formed RHS Beams", Journal of Structural Engineering, ASCE, 1995, Vol. 121, No. 11, pp. 1565 - 1573.
[45] Pi, Y.L. and Trahair, N.S., "Lateral Buckling Strengths of Cold-formed Rectangular Hollow Sections", Thin-Walled Structures, 1995, Vol. 22, No. 2, pp. 71-95.
[46] Trahair, N.S., "Inelastic Buckling Design of Monosymmetric I-beams", Engineering Structures, 2012, Vol. 34, pp. 564-71.
[47] Trahair, N.S., "Distortional Buckling of Overhanging Monorails", Engineering Structures, 2010, Vol. 32, pp. 982-7.
[48] Trahair, N.S., "Design of Steel Single Angle Lintels", Journal of Structural Engineering, ASCE, 2009, Vol. 135, No. 5, pp. 539-45.
[49] Pi, Y.L. and Trahair, N.S., "Inelastic Bending and Torsion of Steel I-beams", Journal of Structural Engineering, ASCE, 1994, Vol. 120, No. 12, pp. 3397-3417.
[50] Trahair, N.S. and Papangelis, J.P., "Flexural-Torsional Buckling of Monosymmetric Arches", Journal of Structural Engineering, ASCE, 1987, Vol. 113, No. 10, pp. 2271-2288.
[51] Pi, Y.L. and Trahair, N.S., "In-plane Buckling and Design of Steel Arches", Journal of Structural Engineering, ASCE, 1999, Vol. 125, No. 11, pp. 1291-1298.
[52] Papangelis, J.P. and Trahair, N.S., "Buckling of Monosymmetric Arches Under Point Loads", Engineering Structures, 1988, Vol. 10, No. 4, pp. 257-264.
[53] Pi, Y.L. and Trahair, N.S., "Inelastic Lateral Buckling Strength and Design of Steel Arches", Engineering Structures, 2000, Vol. 22, No. 8, pp. 993-1005.
[54] Pi, Y.L., Bradford, M.A., Trahair, N.S. and Chen, Y.Y., "A Further Study of Flexural-torsional Buckling of Elastic Arches", International Journal of Structural Stability and Dynamics, 2005, Vol. 5, No. 2, pp. 163-183.

[55] Pi, Y.L., Bradford, M.A. and Trahair, N.S., "Inelastic Analysis and Behaviour of Steel I-beams Curved in Plan", Journal of Structural Engineering, ASCE, 1999, Vol. 126, No. 7, pp. 772-9.

[56] Papangelis, J.P. and Trahair, N.S., "Integrated Computer Analysis and Design of Steel Structures", Proceedings, 5th International Conference on Civil and Structural Engineering Computing, 1993, pp. 45-54.

Advanced Steel Construction Vol. 14, No. 1, pp. 57-72 (2018)

EXPERIMENTAL STUDY ON THE PERFORMANCE OF SLANT END-PLATE CONNECTIONS AT ELEVATED TEMPERATURE

Farshad Zahmatkesh[1,*], Mohd. H. Osman[2], Elnaz Talebi[3],
Ahmad Kueh[3] and Mahmood Tahir[3]

[1]Pennsylvania Housing Research Centre (PHRC), Department of Architectural Engineering, Pennsylvania State University, University Park, PA, 16801, USA
[2] UTM Forensic Engineering Centre, Faculty of Civil Engineering, Universiti Teknologi Malaysia, 81310 UTM Johor Bahru, Johor, Malaysia
[3]Construction Research Centre (CRC), Faculty of Civil Engineering, Universiti Teknologi Malaysia, 81310 UTM Johor Bahru, Johor, Malaysia
**(Corresponding author: E-mail: fa_zahmatkesh@yahoo.com)*

Received: 24 January 2016; Revised:23 March 2017; Accepted: 25 March 2017

ABSTRACT: Axially restrained steel beams exhibit lower structural efficiency when they are subjected to elevated temperature. Thermal expansion is one of the most hazardous conditions such beams could experience throughout their service life. In this regard, using an adequately performing connection can enhance the thermal performance of the beams. This paper, therefore, evaluates experimentally the performance of slant end-plate as a proposed connection for dissipating thermal expansion experienced by the steel beam. In this study, several experimental tests were carried out on two different specimens in terms of scaling and gravity loads to prove the hypothesis and results obtained from a present analytical study. The evaluation of tests and analytical results showed that both outcomes are consistent with each other with comparison ratios between 0.96 and 1.09. In addition, the experimental tests, as well as analytical outcomes, have proven that the slant end-plate connection can successfully reduce the additional thermally induced axial forces via the upward crawling mechanism.

Keywords: Slant end-plate connection, elevated temperature, gravity load, experimental test, analytical model

DOI: 10.18057/IJASC.2018.14.1.4

1. INTRODUCTION

Thermal effects are well-known as among the most harmful loading types any steel structure can experience throughout its service life. With ever-developing large cities and limited space available for buildings, it is inevitable that structures grow in an upward fashion. As a result, the risk of thermal hazard increases as well. Thus far, it is well documented that thermal loading has a significant influence on steel structural components. Elevated temperature can induce an extra axial force in structural members. One most common thermal effect identified in steel structures is the reduction in compressive strength due to increase in temperature. Rodrigues et al. [1] found that the thermal failure of a structural element occurs in two major stages: linear and nonlinear. They posited that the first stage constitutes the initiation mechanism of failure, involving the yielding of members before the inelastic regime and the reduction of Young's modulus. Mourão and Silva [2] investigated the expansion of steel beams caused by uniformly elevated temperatures and illustrated that in an axially restrained beam, the end supports resist against thermal expansion. Wong [3] demonstrated that the strength of a steel beam at room temperature is acceptable for design regardless of the existence of axially restrained boundary conditions or otherwise.

The search for an economical resistance method to improve the performance of steel structures in the presence of elevated temperature remains a challenging task that captures the interest of structural engineers. Research on steel structures with the confinement of axial expansion in restrained beams has been quite intensive since the early 2000s. Commonly employed engineering solutions, which address temperature-related concerns, take the form of section area increment, provision of lateral supports [4], cooling action by air-conditioning and watering [5], and thermal breaks [6].

A considerable amount of literature has been published on the structural response of steel beams under initially induced thermal axial forces [7-9]. In addition, a number of studies have investigated end-plate connections at elevated temperatures [10-15]. However, there is so far no adequate evidence showing the existence of a reliable structural method to reduce the axial force in restrained beams subjected to elevated temperature. In the present work, we propose to explore further by experimental means slanted end-plate connections as a structural solution to protect beam and connections against primary failure in the presence of elevated temperature. The fundamental development in terms of an analytical model for such a connection when subjected to a non-symmetric gravity load and a temperature increase has been formulated by Zahmatkesh et al. [16]. They demonstrated that a temperature increase in a steel beam with conventional connections induces a huge additional axial force that decreases the beam ability to bear external gravity loads. Besides, this study shows that by changing the connection to that of the slanting type, this additional axial force can be dissipated efficiently.

2. VERTICAL AND SLANT END-PLATE CONNECTIONS CHARACTERISTICS AT ELEVATED TEMPERATURE

The popularity of end-plate connections is largely owed to their simplicity in fabrication and installation. Figure 1 shows the typical conventional (vertical) and slant end-plate connections. In general, these connections consist of end-plates that are welded to the ends of a beam in the workshop and then bolted to the flange of columns on site. They can be utilised with slanted beams and are able to tolerate moderate offsets in the beam to column joints. The current study has focused on the slant end-plate connection as a proposed thermal resistance connection. The slant end-plate connection is similar to conventional end-plate connections, differing only in the inclination angle of the end-plate as shown in Figure 1. In the currently investigated experimental tests, the angle of slanting of the end-plate is set to 45^{o}, as it is a practical angle for installing bolts into the holes at the top and bottom of the end-plate.

In elevated temperature conditions, when a steel beam is heated, it tends to expand. Therefore, if the supports resist this expansion, an additional axial force is generated in the beam. Usually, the thermal elongation (ΔL) of the steel beams is very small in the elastic range of material. Zahmatkesh et al. [17] demonstrated that the use of slant end-plates instead of conventional (vertical) connections can lead to a dissipation of the generated thermal axial force. Equations 1 to 4 determine the value of axial force (P) in an axially restrained steel beam with slant end-plate connections under various loading conditions.

Under symmetric gravity load and before elevated temperature:

$$P_i = \frac{WL}{2}\cot(\theta + \phi) \qquad (1)$$

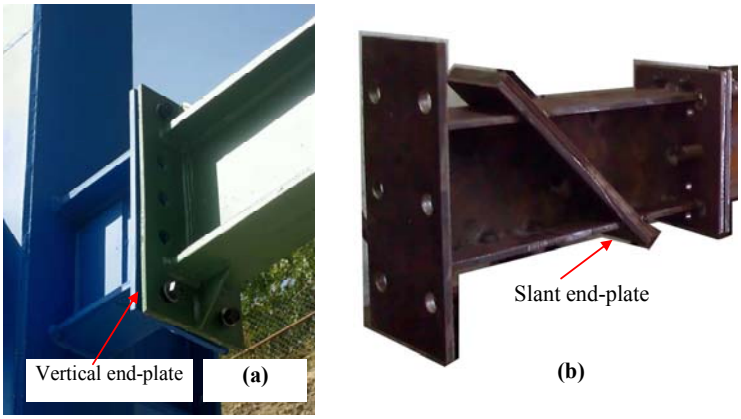

Figure 1. Typical (a) Vertical and (b) Slant Bolted End-plate Connections

Under non-symmetric gravity load, before sliding and before elevated temperature:

$$P_i = (aWL)\cot(\theta + \phi) \qquad (2)$$

Under non-symmetric gravity load, after sliding and before elevated temperature:

$$P_i = \frac{WL\left(\cos^2\theta - \sin^2\phi\right)}{\sin 2\theta} \qquad (3)$$

After elevated temperature for both cases of gravity loads:

$$P_{t\,(m)} = \frac{WL}{2}\cot(\theta - \phi) \qquad (4)$$

where W is the linear uniform gravity load along the length of steel beam (L), a is the slanting angle, ϕ is the friction angle between slant end-plates based on the Coulomb model, and a is the distance of the resultant of non-symmetric gravity load to support. The thermal force dissipation mechanism involves an upward crawling of the connections inclined surfaces at the end of the steel beam as a result of expansion. The behaviour of a restrained steel beam with vertical and slant end-plate connections under temperature increase are shown in Figures 2 and 3, respectively. As shown in Figure 2, after an increase in temperature, the conventional (vertical) connections resist against expansion of the beam and it is buckled because the beam could not tolerate an extra axial load (P_{cr}). On the other hand, Figure 3 illustrates that, after an elevation in temperature, two inclined supports induce thermal axial force into the steel beam through member expansion. However, the two slanted surfaces allow the beam to dissipate the thermal axial force and expansion by linear crawling on the two inclined plates. Although there is a vertical motion tolerance between the surfaces in the conventional (vertical) end-plate connections, it is unable to absorb the overall thermal expansion at the two ends of the beam in the horizontal direction. This is because the direction of thermal expansion is perpendicular to the direction of the moving surface. In the slant end-plate connection, there is a slanting tolerance between the surfaces to absorb the thermal elongation of the beam using the crawling mechanism over the slanting faces. Therefore, the direction of horizontal expansion can be projected to the slanting plane of the connection.

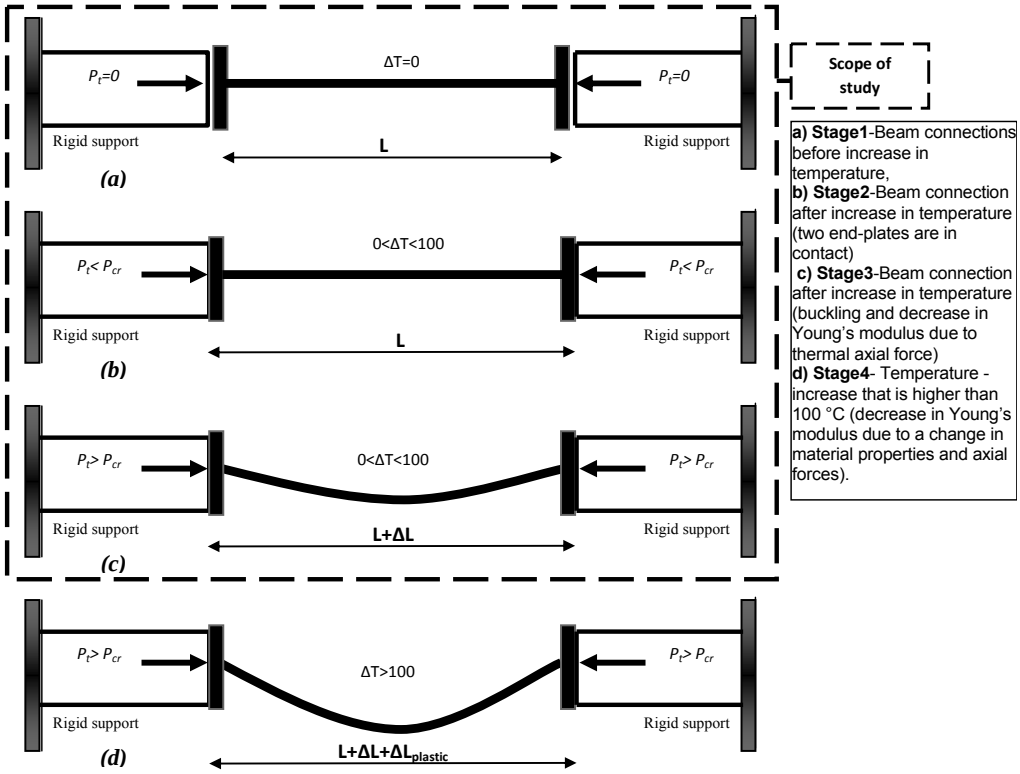

Figure 2. Beam with Vertical Bolted End-plate Connection subjected to Temperature Increase

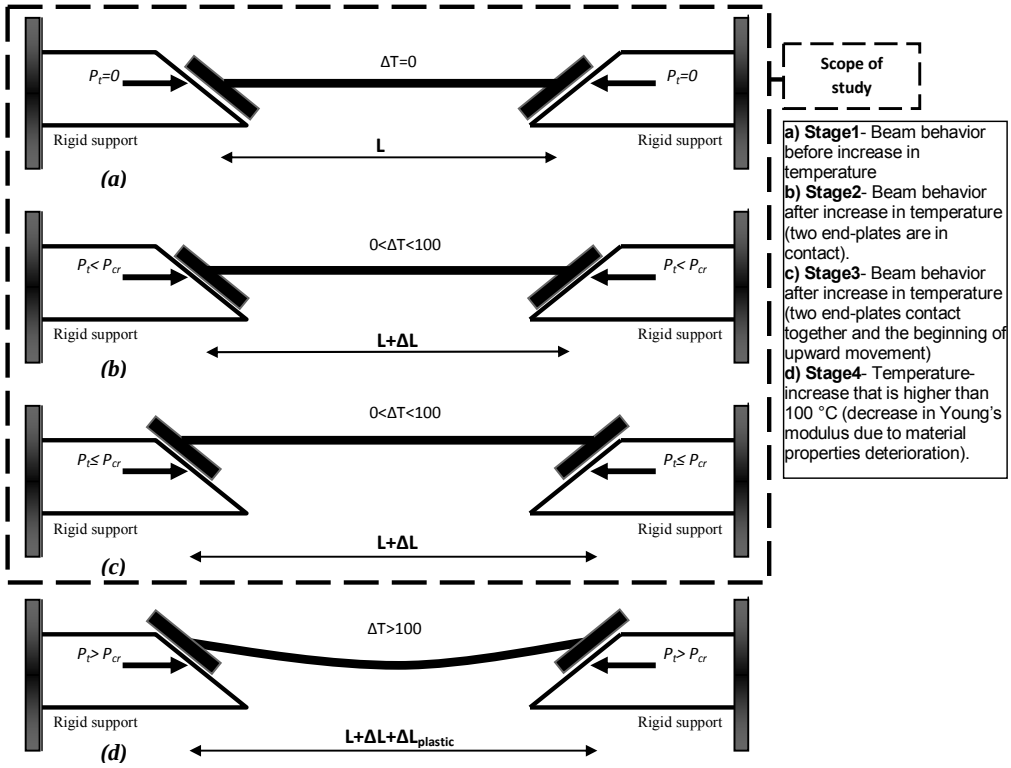

Figure 3. Beam with Slant Bolted End-plate Connection subjected to Temperature Increase

3. EXPERIMENTAL STUDY

To validate the results of the analytical method used by Zahmatkesh et al. [17], two cases were of interest: i) small-scale and ii) full-scale specimens. Table 1 lists the material properties of steel beams used in this study.

Table 1. Material Properties of Steel Beam

Material type	Yield stress [MPa]	Ultimate stress [MPa]	Density [kg / m^3]	Young's modulus [GPa]	Linear coefficient of thermal expansion	Poisson's ratio
St37	240	370	7850	200	1.5e-5	0.3

3.1 Small-Scale Specimen

3.1.1 Symmetric gravity load test

The structural responses computed by the analytical approach were first compared with the experimental tests on the small-scale specimen. Experimental data were taken from the small-scale steel beam tests carried out at the Structure Lab of the Universiti Teknologi Malaysia (UTM). The geometrical details of the considered structure are shown in Figure 4. The section of the specimen was of H shape with a thickness of 1.5 mm. The columns height and the beam length were 235 mm and 450 mm, respectively (the middle beam was 350 mm long). Figure 5 shows the composition of components used for the small-scale specimen test. The structural members of this specimen consist of five separate parts: the beam specimen with inclined ends supported by a corbel beam at each end and two columns. These five parts were assembled with normal bolts and nuts. To conduct the tests, the beam was detached as a separate component from the supporting frame, resembling those of the analytical assumptions [17].

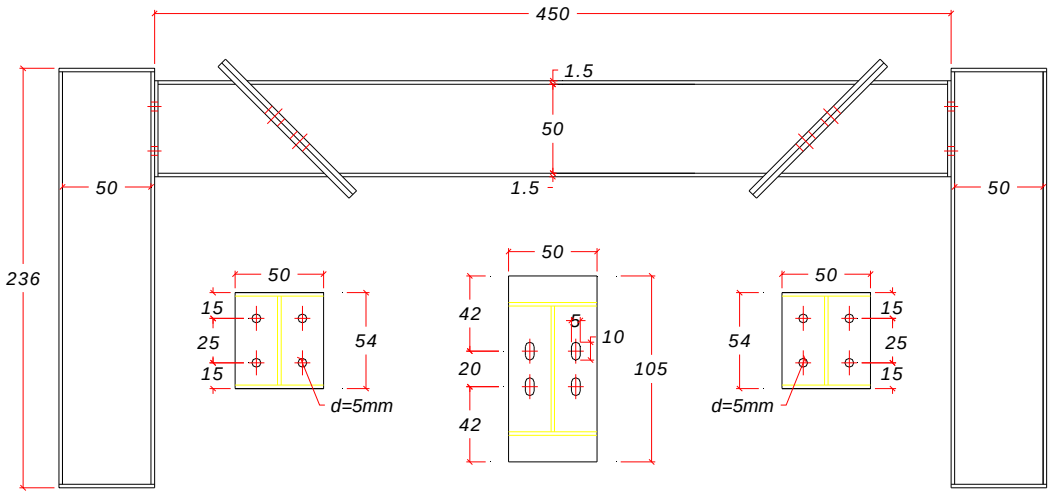

Figure 4. Geometrical Details of the Steel Beam with Slant End-plate Connection for Experimental Study (Small-scale Specimen). All Units are in mm

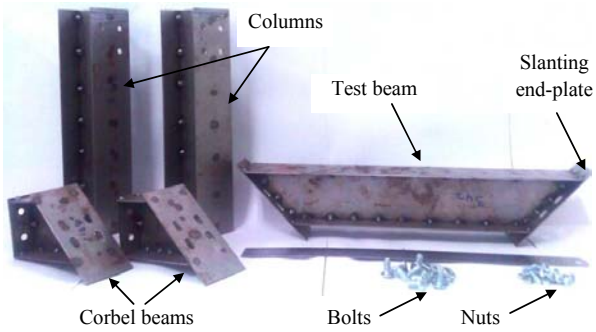

Figure 5. Parts of a Steel Frame with Slant End-plate Connection (Small-scale Specimen)

In line with the primary assumptions, the axially restrained steel beam was connected to the end supports by a slider system. As a result, oversize holes with clearance for bolts movement were considered for free sliding of the beam on the inclined end-supports, as in the primary assumptions. For this reason, four oval shape holes (slot) have been provided for free sliding of the beam on the slanted supports. The tightened normal bolts had been restricted for plane displacement but they were free for sliding on the inclined supports. Conforming to the analytical equations, the friction factor, μ_s, between two faces of the slant end-plate connection was required. Figure 6 shows a basic friction test set-up for determining the friction factor between the inclined steel plates. The self-weight of the beam was 6.67 N with a connection slanting angle of 45° ($\theta = 45°$). As shown in Figure 6 a 39.22 N weight had been placed at the end of the left side beam in the vertical direction. To measure the sliding force, a load cell with 5 kN capacity had been located at the side of the beam. A data logger (UCAM-70A) had been used to measure the corresponding axial force. The static friction coefficient was found to be 0.37 ($\mu_s = tan\ \varphi$) from the test.

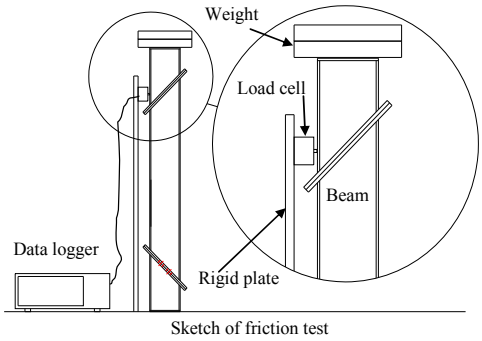

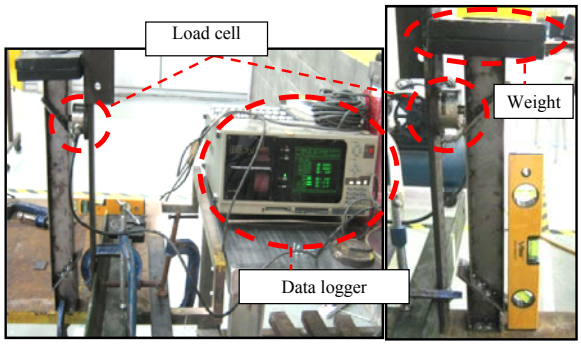

Figure 6. Friction test for finding the static friction coefficient (μ_s) between two faces of slant end-plate connection (small-scale specimen)

After determining the friction coefficient, the small-scale specimens were tested at room and elevated temperatures conditions. The tests were designed with the aim of verifying the performance of the slant connection as well as the analytical method. Figure 7 shows the test set-up for the small-scale specimen. In the conducted tests, the values of axial force in the beam due to elevated temperature and seven symmetric gravity load intensities (6.67 N, 26.29 N, 45.91 N, 65.53 N, 85.15 N, 104.77 N and 124.39 N) were recorded.

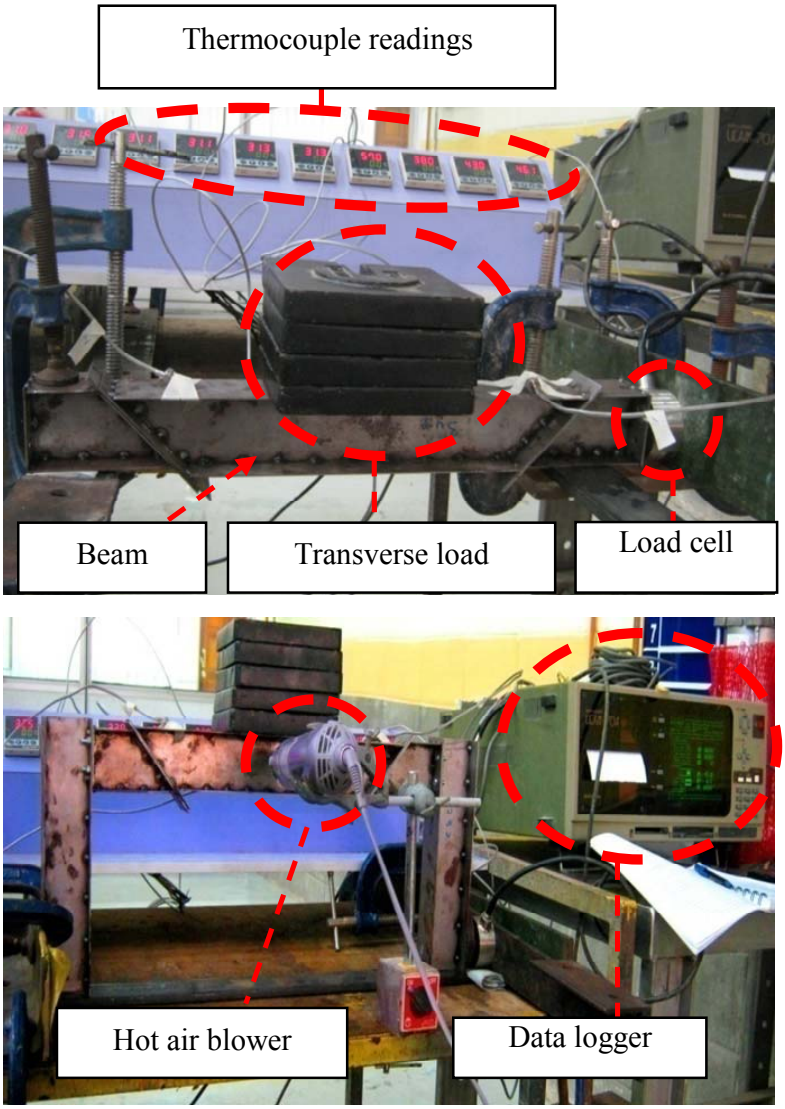

Figure 7. Test set-up for Small-scale Specimen under Symmetric Gravity Load

Similar to the friction test, the axial force was recorded with the data logger and a load cell located at the end of the beam. To keep the temperature under 100° or within elastic zone [18], 10 thermocouples were attached along the beam with the heat source coming from a hot air blower placed in the middle of the beam. Note that only some key outcomes of the analytical method are considered for comparison with the experimental responses. Figure 8 shows the relationships between gravity loads and axial forces (P_i and P_t) in the beam for two case studies, before and after elevated temperatures. It is evidenced that the analytical models

conform acceptably to the outcomes produced by experiments, both before and after temperature increase, thus reflecting the consistency of both methods.

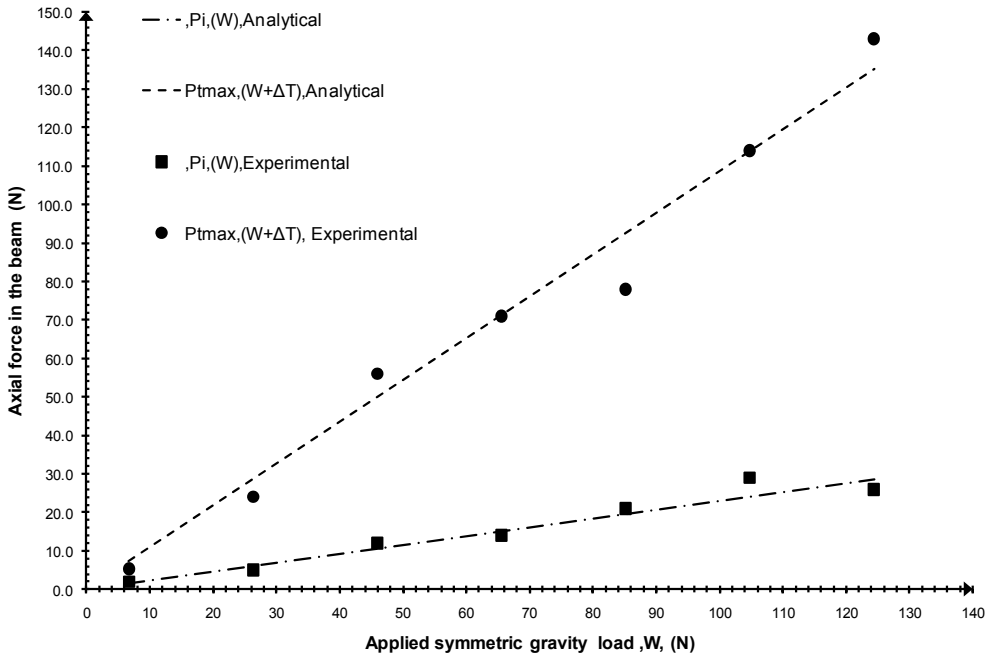

Figure 8. Relationship between Symmetric Gravity Load and induced Axial Force in the Beam in Small-scale Specimen (friction factor, $\mu_s = tan\ \Phi = 0.37$, $\theta = 45°$)

3.1.2 Non-symmetric gravity load test

In the second stage, the small-scale specimen was tested under non-symmetric gravity loads. In the non-symmetric load case study, the distance between slant support and the resultant vector of gravity load is *a.L* where *L* is the length of the beam (Figure 9). Based on Equation (5) [19], the values of *a* factor can be determined for both before and after sliding cases. The obtained *a* factors for the cases before and after sliding were 0.688 and 0.878, respectively.

$$a \le \frac{\cot(\theta - \phi)}{\cot\left(\theta + \phi\right) + \cot(\theta - \phi)} \qquad \text{Equilibrium condition before sliding} \quad (5)$$

The beam was tested for several incrementally applied non-symmetric gravity loads with three sub-cases: before (two cases) and after elevated temperatures. Figure 9 shows the test set-up for both cases, i.e., before and after sliding. During the test, the axial force was recorded with a force sensor located at the end of the beam that was connected to an interface kit system (model 8/8) attached to a computer. The distances from the centre of mass of gravity load to the right support were 0.688*L* and 0.878*L,* respectively.

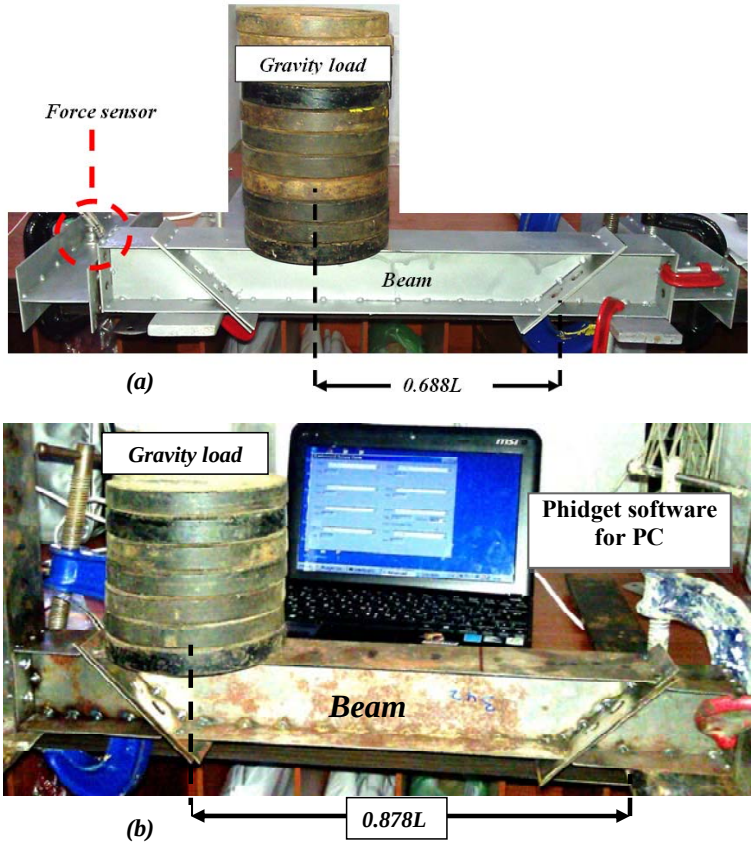

Figure 9. Test Set-up at Room Temperature for Two Case Studies
a) before sliding, a = 0.688 and b) after sliding, a = 0.878

In the case of after elevated temperature, a 10-channel thermocouple set was used for measuring the applied temperature with the heat source coming from a hot air blower placed in the middle of the beam. The aim was the same, i.e., to measure the axial force in the beam for incremental load magnitudes. In compliance with the experiment, the results obtained from the analytical approach (the small-scale specimen modelling) were used for comparison. Figure 10 shows the relationships between applied non-symmetric gravity loads and axial forces in the small-scale specimens for all cases of sliding and temperature conditions. The trend exhibited by the experimental test is reasonably similar to that of the analytical method. It is apparent that in both methods, the axial force in the beam increased with the non-symmetric gravity load.

As shown in Figure 10, after the initiation of primary sliding on the inclined surface, an increase in temperature did not change the axial force. Because of limitations imposed on the experimental study, only some of the important features were chosen for testing (for example, it would have been somewhat laborious to change the friction factor to cover all cases). Results indicate that the model agrees well with the experimental findings, both with and without temperature change.

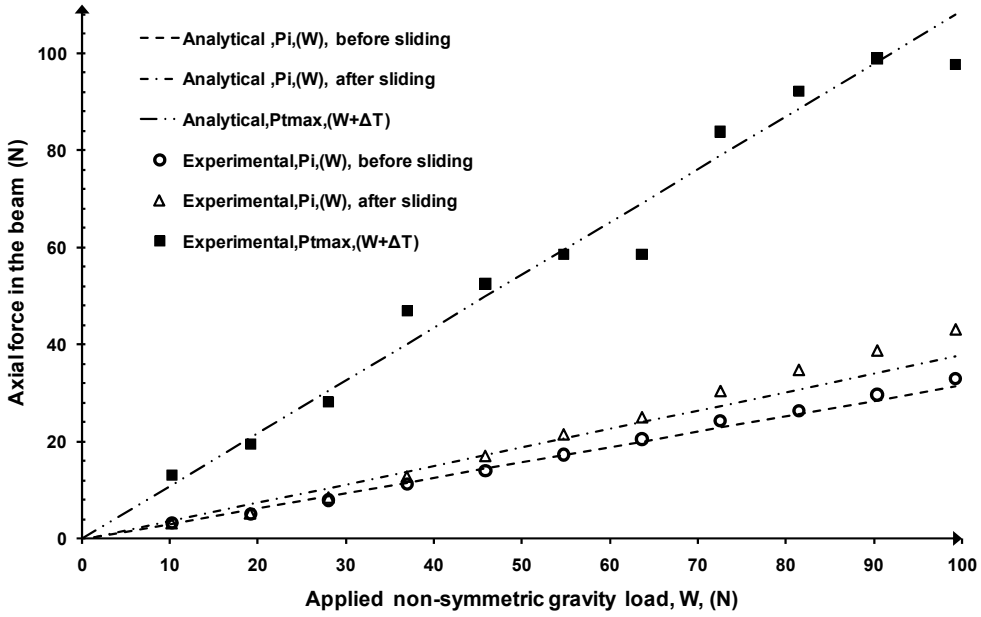

Figure 10. Relationship between Non-symmetric Gravity Load and Axial Force in the Small-scale Specimen (friction factor, $\mu s = \tan \varphi = 0.37$, $\theta = 45°$)

3.2 Full-Scale Specimen

3.2.1 Symmetric gravity load test

Next, the thermal performance of a full-scale specimen with slant end-plate connections was investigated by experimental tests where the direction of supports slanting angle had been fixed at 45°. Again, the structural responses computed by the analytical method were used for comparison. The geometrical details of the structure are shown in Figure 11. As shown in this figure, the main and side beams were of I sections with a thickness of 6 mm for webs and 8 mm for flanges. The length of the beam was 1800 mm. Figure 12 shows the composition of components used for the full-scale specimen test. The structural components of this specimen consist of five separate parts: the test beam with slanting ends and two short side beams. These five parts were assembled by normal bolts and nuts.

For the tests, the side beams and middle beam were attached as a connected member of the whole specimen, similarly to the analytical assumptions. According to the analytical hypothesis, the axially restrained steel beam is connected by a sliding connection system. Therefore, slot holes were considered in the specimen for free sliding of the beam on the inclined supports.

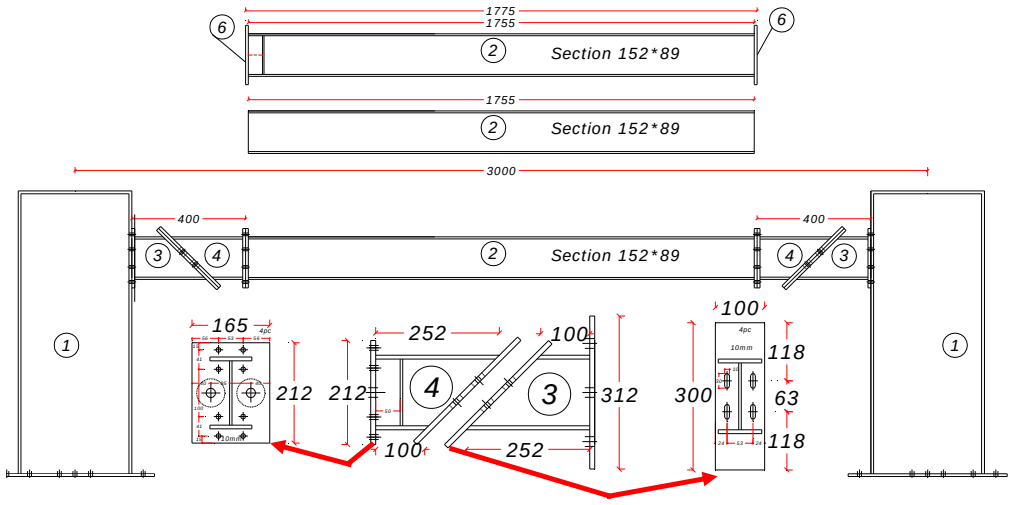

Figure 11. Geometrical details of the Steel Beam with Slant End-plate Connection for Experimental Study (Full-scale Specimen). All Units are in mm

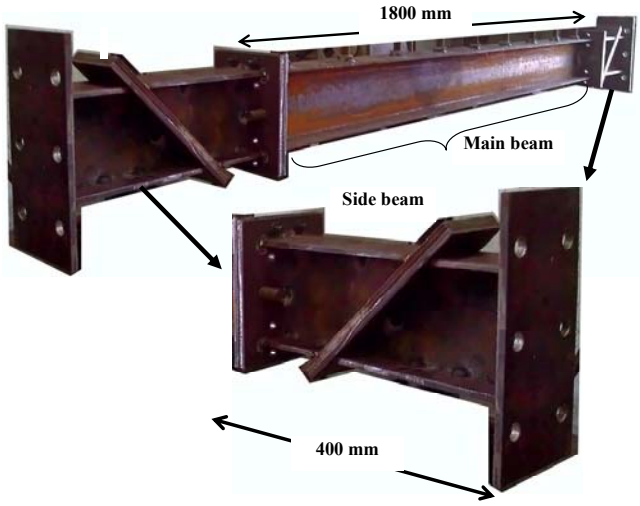

Figure 12. Parts of the Steel Beam with 45° Slant End-plate Connection (Full-scale Specimen)

For the current test, the friction factor, μ_s, between two plates of the slant connection was also needed. Therefore, the friction test was again carried out to determine the friction coefficient of connections. Figure 13 presents the setting of the friction test based on the Coulomb friction concept on the inclined surface. The self-weight of the side beam was 0.08826 kN with a connection slanting angle of 45° ($\theta = 45°$). The overall weight on top of the side beam was obtained as 0.14164 kN. As shown in Figure 13, a load cell of 1 kN capacity had been located at the right side of the beam to measure the value of the sliding force. An automated digital data logger (Phidget 4 bridge- interface kit) was used to measure the corresponding axial force. The friction test measured a magnitude of 0.42 ($\mu_s = tan\ \varphi$) for the static friction coefficient of the inclined surfaces. After finding the friction coefficient, the components of the full-scale specimen were installed between two rigid columns that provided fixed-end supports, similar to the analytical assumption. The test was carried out at two different temperatures, before and after elevated temperatures. In the idealised models in the analytical and numerical methods, the value of the elevated temperature was considered uniform.

Therefore, in the experimental tests, a steady-state heating trend was employed. The heat application was carried out for a few minutes to ensure the uniformity of temperature throughout the beam.

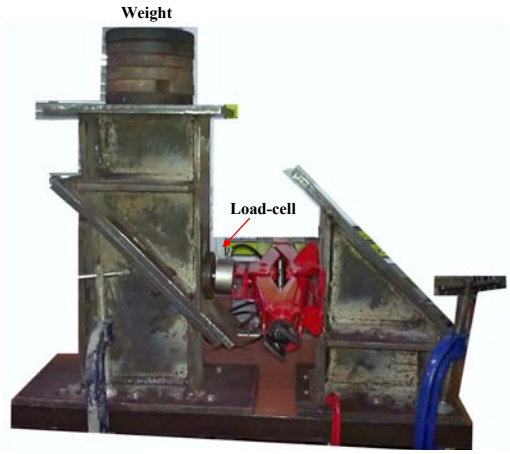

Figure 13. Friction Test to Determine the Static Friction Factor (μ_s) between the Two Faces of Slant End-plate Connection (Full-scale Specimen)

A series of tests were conducted to verify the analytical outcomes. Figure 14 shows one of the typical cases. As shown in this figure, the axial forces were measured by a 5 kN (capacity) load cell located at the side beam. The measured values were recorded by a digital data logger board (Phidget 4 Bridge) that was linked to a computer. For the heating system, an electrical heating element was installed on the web so that the required temperature can be controlled by a control box. To keep the temperature within 100 °C or elastic zone [18] , one thermocouple set was attached to the main beam. The thermal sensor of this set was connected to a digital screen board in the control box so that the maximum temperature for the heating system can be imposed. The performance of the steel beam was investigated under 13 symmetric gravity load intensities (0.215 kN, 0.382 kN, 0.549 kN, 0.828 kN, 1.043 kN, 1.195 kN, 1.303 kN, 1.503 kN 1.703 kN, 1.903 kN, 2.003 kN, 2.103 kN and 2.203 kN). The results from the experimental studies were compared at certain loadings with the analytical models. Figure 15 shows the relationships between applied loads and axial forces in the beam at two different thermal conditions: before and after elevated temperatures. It is evidenced that the analytical models conform acceptably to the results produced by experiments, both before and after temperature increase.

3.2.2 Non-symmetric gravity load test

In the non-symmetric case study, the beam specimen was tested under a group of weights for two different load distributions in terms of resultant gravity load location on the beam. With the analytical equation (Equation 5) the values of a can be determined for both before and after sliding cases for the full-scale specimen: these values were obtained as 0.65 and 0.8, respectively. Similarly, the beam was tested for several incrementally applied non-symmetric gravity loads with three sub-cases: before (two cases) and after elevated temperature. During the test, the axial force was recorded with a force sensor located at the end of the side beam and an interface kit system (model 8/8) attached to a computer. The aim was the same, i.e., to measure axial force in the beam for incremental load magnitudes. For the current tests, the distances from the centre of mass of non-symmetric gravity load to the right support were $0.65L$ and $0.8L$ for the cases of before and after sliding, respectively. The beam of a full-scale

specimen was tested at room and elevated temperatures. A thermocouple set was used to measure the applied temperature. The heat source from an electrical element was placed in the middle of the beam web. The experimental results were compared with the analytical results. Figure 16 illustrates a comparison between the analytical and experimental methods based on the relationships between applied non-symmetric gravity loads and the axial forces in the steel beam, for various sliding and thermal conditions.

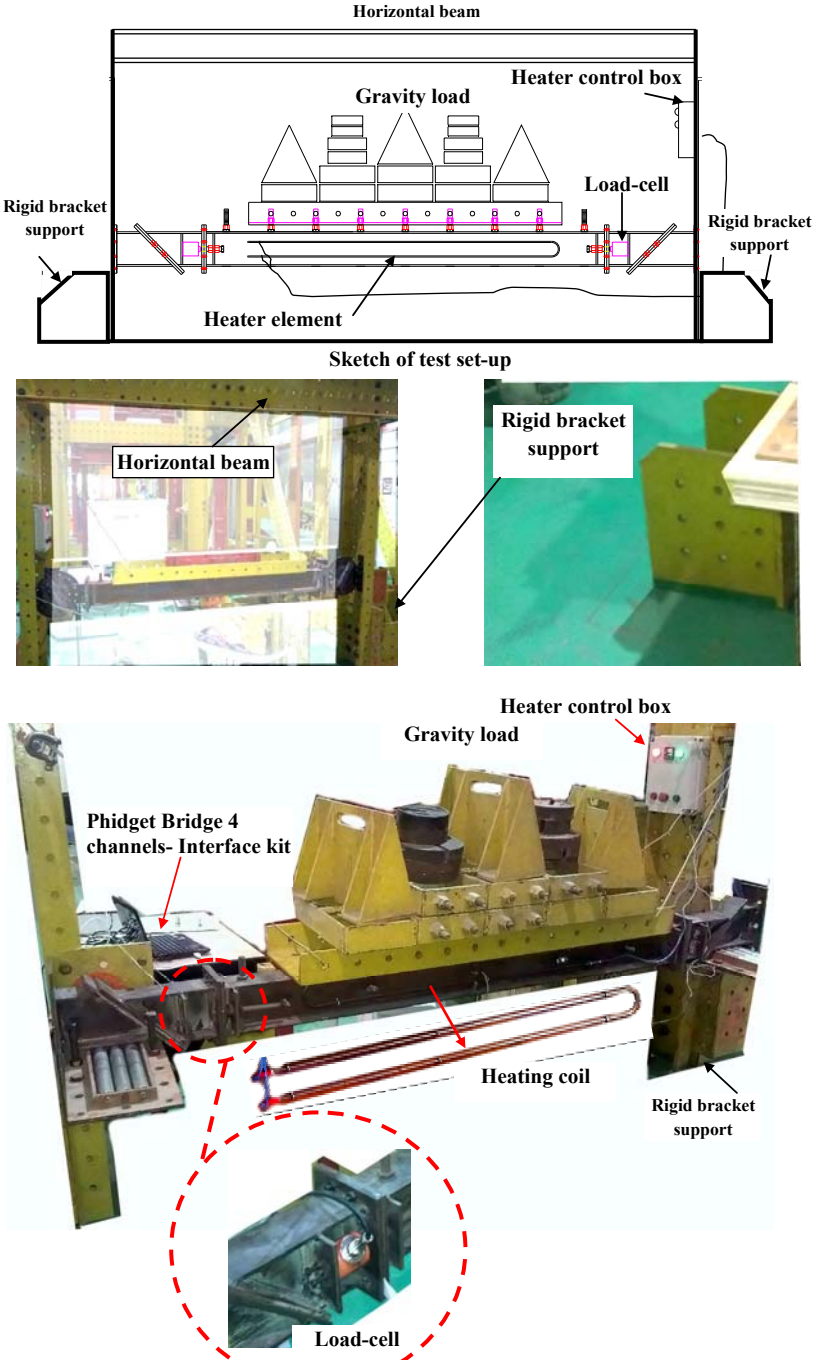

Figure 14. Test Set-up for full-scale Specimen with θ = 45° under Symmetric Gravity Load

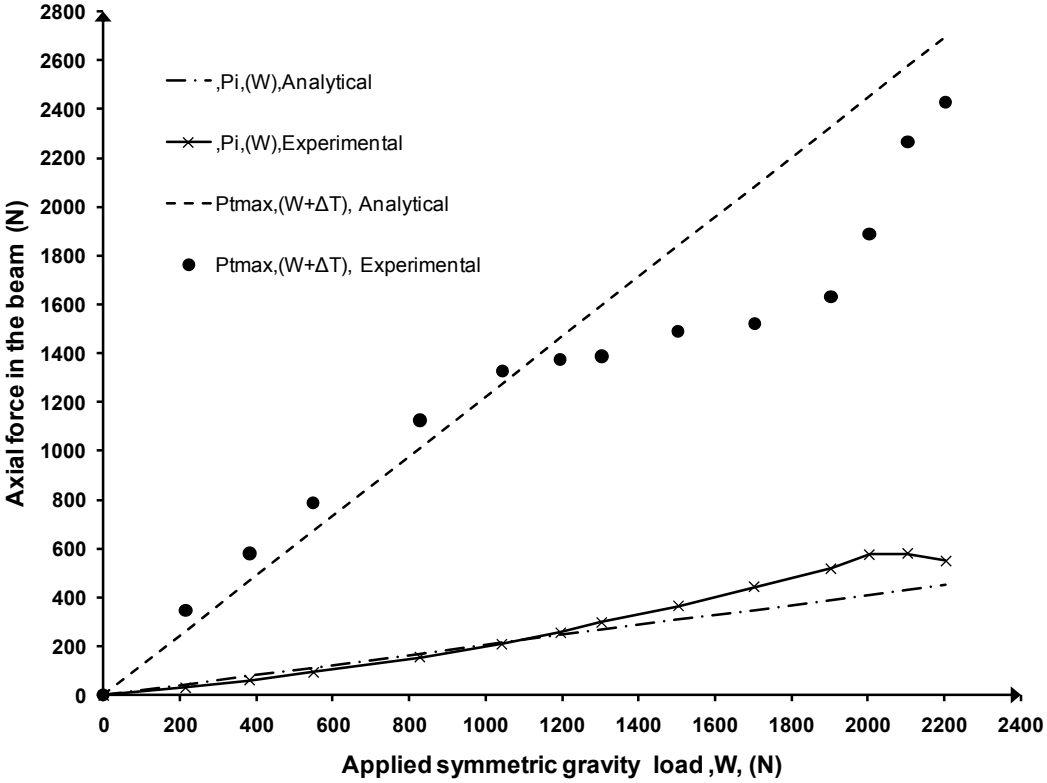

Figure 15. The Relationship between Symmetric Gravity Load and Axial Force in the Beam for Full-scale Specimen (friction factor, $\mu_s = tan\ \Phi = 0.42$, $\theta = 45°$)

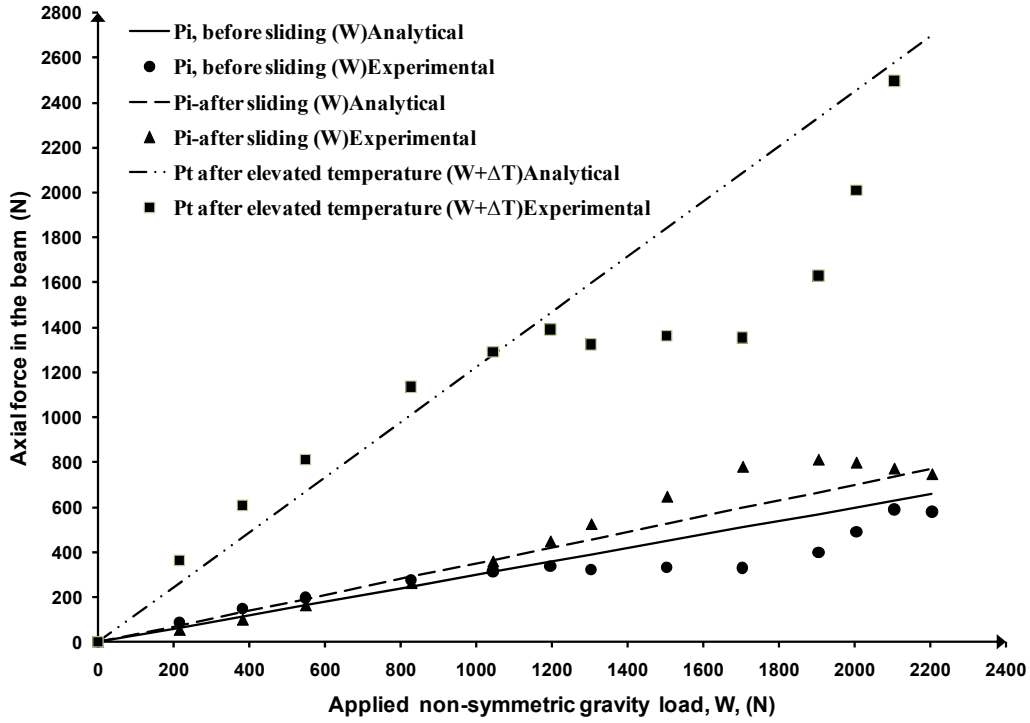

Figure 16. Relationship between Non-symmetric Load and Axial Force in the Full-scale Specimen (friction factor, $\mu_s = tan\ \varphi = 0.42$, $\theta = 45°$)

In the experimental study, two specimens with different sizes were designed to verify the primary hypothesis on the performance of the proposed connection. On the other hand, structural behaviour was simulated and examined by an analytical approach. Equation 6 is adopted to determine the comparison ratio of analytical to test results where P is the measured axial force under various boundary conditions such as P_i or P_t and n is the number of tests under various gravity loads.

$$R_{average-ratio} = \sum_{i=1}^{n} \frac{\left(\frac{P_{i(Analytical)}}{P_{i(test)}} \right)}{n} \quad (6)$$

The comparison ratio for the small-scale specimen is 0.97 under symmetric gravity load only. However, after an increase in temperature, this ratio is computed as 1.08. Under non-symmetric gravity load, the ratio ranges from 1.00 to 1.02. From the full-scale specimen, the comparison ratios are between 0.96 and 1.09.

4. CONCLUSION

In this research, a series of experimental tests was conducted for steel beams with a 45° slanting angle of end-plate connection to validate the results obtained from the analytical approach, where two sets of specimens were fabricated for tests: a small-scale and a real-scale physical models.

The test results were in consistency with those of analytical for both the small-scale and real-scale specimens within an acceptable range of agreement. Therefore, the models can predict satisfactorily the behaviour of a steel beam with slant end-plate connections in various boundary conditions.

It is concluded that the axial load-bearing capacity of a steel beam under symmetric gravity load is higher than that under non-symmetric load at room temperature. On the other hand, the axial load-bearing capacity of this beam is identical under elevated temperature conditions for both symmetric and non-symmetric gravity loads.

ACKNOWLEDGEMENTS

The research was financially supported by the School of Graduate Studies (SPS), Universiti Teknologi Malaysia (PY/2012/00977).

REFERENCES

[1] Rodrigues, J.P.C., Cabrita Neves, I. and Valente, J.C., "Experimental Research on the Critical Temperature of Compressed Steel Elements with Restrained Thermal Elongation", Fire Safety Journal, 2000, Vol. 35, No. 2, pp. 77-98.

[2] Mourão, H.D.R. and E Silva, V.P., "On the Behaviour of Single-span Steel Beams under Uniform Heating", Journal of the Brazilian Society of Mechanical Sciences and Engineering, 2007, Vol. 29, No. 1, pp. 115-122.

[3] Wong, M.B., Modelling of Axial Restraints for Limiting Temperature Calculation of Steel Members in Fire", Journal of Constructional Steel Research, 2005, Vol. 61, No. 5, pp. 675-687.
[4] Usmani, A.S., Rotter, J.M., Lamont, S., Sanad, A.M. and Gillie, M., "Fundamental Principles of Structural Behaviour under Thermal Effects", Fire Safety Journal, 2001, Vol. 36, No. 8, pp. 721-744.
[5] Bailey, C.G., Burgess, I.W. and Plank, R.J., "Analyses of the Effects of Cooling and Fire Spread on Steel-framed Buildings", Fire Safety Journal, 1996, Vol. 26, No. 4, pp. 273-293.
[6] Larson, S.C. and Van Geem, M.G., "Structural Thermal Break Systems for Buildings: Feasibility Study: Final Report, in Other Information: Portions of this Document are Illegible in Microfiche Products", Original Copy Available until Stock is Exhausted, 1987, pp. Medium: X, Size: Pages: 102.
[7] Bradford, M., "Elastic Analysis of Straight Members at Elevated Temperatures. Advances in Structural Engineering, 2006, Vol. 9, No. 5, pp. 611-618.
[8] Takagi, J. and Deierlein, G.G., "Strength Design Criteria for Steel Members at Elevated Temperatures", Journal of Constructional Steel Research, 2007, Vol. 63, No. 8, pp. 1036-1050.
[9] Yuan, Z., Tan, K.H. and Ting, S.K., "Testing of Composite Steel Top-and-seat-and-web Angle Joints at Ambient and Elevated Temperatures, Part 1: Ambient Tests", Engineering Structures, 2011, Vol. 33, No. 10, pp. 2727-2743.
[10] Sarraj, M., Burgess, I., Davison, J. and Plank, R., "Finite Element Modelling of Steel Fin Plate Connections in Fire", Fire Safety Journal, 2007, Vol. 42, No. 6, pp. 408-415.
[11] Mao, C., Chiou, Y.-J., Hsiao, P.-A. and Ho, M.-C., "Fire Response of Steel Semi-rigid Beam–column Moment Connections", Journal of Constructional Steel Research, 2009, Vol. 65, No. 6, pp. 1290-1303.
[12] Yu, H., Burgess, I., Davison, J. and Plank, R., "Experimental and Numerical Investigations of the Behavior of Flush End Plate Connections at Elevated Temperatures", Journal of Structural Engineering, 2010, Vol. 137, No. 1, pp. 80-87.
[13] Díaz, C., Martí, P., Victoria, M. and Querin, O.M., "Review on the Modelling of Joint Behaviour in Steel Frames", Journal of Constructional Steel Research, 2011, Vol. 67, No. 5, pp. 741-758.
[14] Lin, S., Huang, Z. and Fan, M., "Modelling of End-Plate Connections in Fire, in Design, Fabrication and Economy of Metal Structures. 2013, Springer. pp. 321-326.
[15] Lin, S., Huang, Z. and Fan, M., "Modelling Partial End-plate Connections under Fire Conditions", Journal of Constructional Steel Research, 2014, Vol. 99, pp. 18-34.
[16] Zahmatkesh, F., Osman, M.H. and Talebi, E., "Thermal Behaviour of Beams with Slant End-Plate Connection Subjected to Nonsymmetric Gravity Load", The Scientific World Journal, 2014. 2014.
[17] Zahmatkesh, F., Osman, M.H., Talebi, E. and Kueh, A.B.H., "Analytical Study of Slant End-plate Connection subjected to Elevated Temperatures", Steel and Composite Structures, 2014, Vol. 17, No. 1, pp. 47-67.
[18] EC3, Eurocode 3 (EC3), BS EN 1993-1-2: Design of Steel Structures, Part 1-2: General Rules-Structural Fire Design. . 2005, British Standards Institution London, UK.
[19] Zahmatkesh, F., Osman, M.H., Talebi, E. and Kueh, A.B.H., "Direct Stiffness Model of Slant Connection under Thermal and Non-symmetric Gravity Load", Journal of Constructional Steel Research, 2014, Vol. 102, No. 0, pp. 24-43.

EXPERIMENTAL STUDY ON EVOLUTION OF RESIDUAL STRESS IN WELDED BOX-SECTIONS AFTER HIGH TEMPERATURE EXPOSURE

Weiyong Wang[1,*], Shiqi Qin[2], Venkatesh Kodur[3] and Yuhang Wang[4]

1. Professor, School of Civil Engineering, Chongqing University, Key Laboratory of New Technology for Construction of Cities in Mountain Area (Ministry of Education), Chongqing, China
**(Corresponding author: E-mail: wywang@cqu.edu.cn)*
2. Graduate student, School of Civil Engineering, Chongqing University, Chongqing, China
3. Professor, Department of Civil and Environmental Engineering, Michigan State University, East Lansing, MI, 48824, USA.
4. Professor, School of Civil Engineering, Chongqing University, Chongqing, China

Received: 20 August 2016; Revised: 18 May 2017; Accepted: 4 June 2017

ABSTRACT: Presence of residual stresses can significantly influence the stiffness and fatigue life of steel structures. The extent of residual stress that develops in welded box-shaped sections at room temperature is extensively studied. However, there is limited data on the development of residual stresses after fire exposure. Such fire exposure has great influence on the residual stress distribution due to temperature induced plastic deformation and creep strains in steel. In order to provide benchmark data for the theoretical models and post-fire design recommendations, this paper presents results from an experimental investigation on the post-fire residual stresses in welded box-shaped sections. The tests are carried out by sectioning method, and two types of commonly used steels, mild Q235 steel with a nominal yield stress of 235MPa and high strength Q460 steel with a nominal yield stress of 460MPa are considered. The residual stresses were evaluated after exposing the specimens to 200℃, 400℃, 600℃ and 800℃and cooling down to room temperature. Data from the tests clear show that the residual stresses decrease significantly with increase in specimen temperature. Further, results from the tests are utilized to propose simplified relations for temperature induced residual stresses in welded box-section of Q235 and Q460 steels.

Keywords: Residual stress, mild Q235 steel, high strength Q460 steel, high temperature, box-section

DOI: 10.18057/IJASC.2018.14.1.5

1. INTRODUCTION

Steels used in construction applications are classified into different categories based on chemical composition, tensile strength properties, and fabrication process as carbon steels, low-alloy steels, heat-treated carbon steels, and high strength steels. Recent years have seen an increasing demand for high strength steels in construction applications due to superior properties of these steels, namely; high yield strength, good welding ability and corrosion resistance. Of these high strength steels, Q460 (with nominal yield strength of 460MPa) steel welded box-sections, as well as mild Q235 (with nominal yield strength of 235MPa) steel welded box-sections, are widely used as compression elements in steel structures.

A structural steel member is most often not stress free initially, but is under built-in residual stresses induced during its manufacturing or welding process. Residual stresses in steel sections are stresses which exist due to uneven cooling or due to cold forming during fabrication process. These residual stresses are defined as internal stresses in an externally unloaded member and are therefore in internal equilibrium at cross-section, leading to instability condition in a structure. The presence of such residual stress can cause premature yielding and loss of stiffness. In practice, for critical welded steel member, post-weld heat treatment is often used and it is a stress relieving process whereby residual stresses are reduced by heating the whole structure to 550–650 °C for a preset

time depending upon the plate thickness. The main aim of post-weld heat treatment is to relieve the residual stresses induced by the welding process.

For simulating the response of a structural member, proper residual stress distribution is to be incorporated in order to evaluate accurate response. The residual stress distribution in a welded box-section is characterized by tensile residual stresses (+) at the weld ends and compression (-) at the middle of webs and flanges. The typical distributions of compressive and tensile residual stresses at ambient temperature are illustrated in Figure 1. The magnitude of the residual stresses in these welded box-shapes not only depends on the filler weld size and welding speed, but also depends on the steel type and thickness of steel plates.

In the last few decades, there have been numerous studies on the magnitude and distribution pattern of residual stresses in welded mild carbon steel sections [1]. Since the stress–strain curves and high-temperature properties [2] of high strength steel (HSS, yield strength≥460 MPa) are different from that of mild carbon steel, it is hypothesized that the residual stresses in a HSS section to be different from that in a mild carbon steel section.

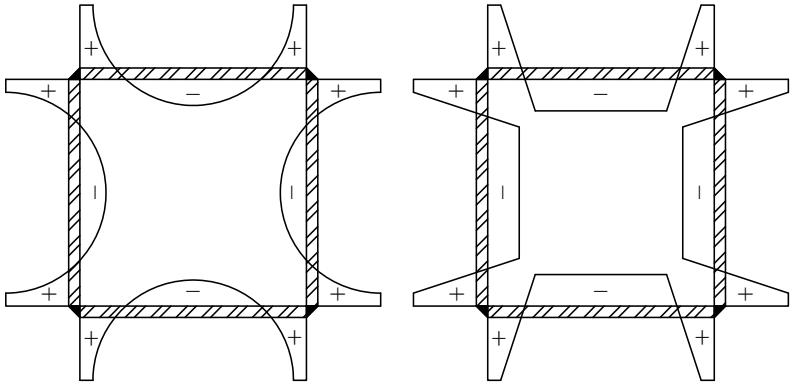

(a) Parabola curve distribution (b) Linear distribution

Figure 1. Typical Residual Stress Pattern in Welded Box Sections

In recent few years, the residual stress in welded high strength steel box section has called more attention to the researchers. In 2012, Wang and Li [3] measured the residual stresses of three welded flame-cut box-section columns with a nominal yield strength of 460 MPa by both sectioning and hole-drilling methods. In 2013, Ban et al. [4] also tested the residual stresses of welded flame-cut box-section columns with a nominal yield strength of 460 MPa by sectioning method. In 2015, Li et al. [5] measured the residual stress in welded high strength Q690 steel box sections, and proposed a distribution pattern. Ma et al. [6] investigated the residual stresses both in longitudinal and transverse directions on three hollow sections using wire-cutting method. In 2016, Khan et al. [7] investigated the induced residual stress distributions in square welded sections fabricated from 690 MPa high strength steel plates with single and multiple weld passes.

All the above reported studies have focused on the residual stress of welded box-shaped sections at ambient conditions, and there is limited research on post-fire induced residual stresses besides the one conducted on H-shaped sections by authors as a preliminary study on post-fire residual stress [8]. Results from this preliminary study showed that the welded H-shaped sections after high temperature exposure exhibit different residual stress distribution due to temperature induced plastic and creep deformations in steel. Further the residual stresses also influence the load carrying capacity of steel members after fire exposure. In order to accurately evaluate the post fire residual capacity of steel members, the magnitude of residual stress in steel sections is to be known. For this

purpose, a comprehensive study on the residual stress distribution in welded box-shaped sections after high temperature exposure was undertaken. As part of this study, a series of tests were carried out to measure post fire residual stress after exposure to various temperatures in welded box-shaped sections, made of Q235 steel and Q460 steel. Using this residual stress data, two residual stress distribution models are proposed for evaluating temperature induced residual stresses in mild Q235 steel and high strength Q460 steel box-sections.

2. MATERIAL PROPERTIES

Two steels commonly used in construction, mild Q235 steel and high strength Q460 steel, were selected for fabricating welded box-shaped section. In order to determine the mechanical properties of these steels at room temperature, tensile strength test were carried out by utilizing a typical tensile strength testing machine. Tension coupons were cut from the same parent plates, with nominal thicknesses of 8 mm, from which the residual stress test specimens are fabricated. The cutting direction was perpendicular to the rolling direction according to GB/T 2975-1998 [9]. An extensometer was fixed at the mid-length of each tension coupon to obtain longitudinal strains for accurate determination of elastic modulus. The linear variable displacement transducer (LVDT) inside the universal testing machine also recorded the displacement between the two clamps after the extensometer was removed when the strain reached 5%. The tension coupons were tested in accordance with GB/T 228-2002 procedure [10].

Table 1 shows test results for 8 tension coupons, where f_y is the yield stress, f_u is the ultimate tensile stress, Δ is the percentage of elongation after fracture and E is the Young's modulus. The stress–strain curve is generated utilizing extensometer data and the LVDT data and is plotted in Figure 2. It can be seen that the Q460 steel, does not exhibit same level of ductility and strain hardening as that of mild carbon Q235 steel. These different properties are likely to result in the difference of residual stresses between welded mild steel sections and high strength steel sections. The reduction factors for elastic modulus after exposure to different temperatures were derived based on recommendations documented in Ref. [11]-[12].

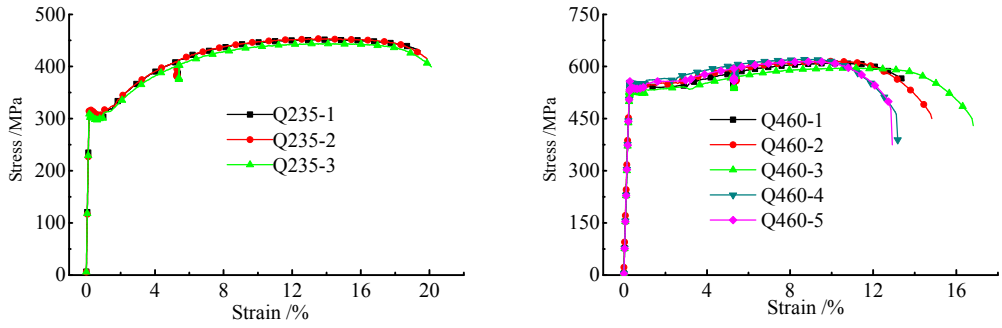

(a) Q235 steel (b) Q460 steel

Figure 2. Stress-strain Curves of Q235 Steel and Q460 Steel

Table 1. Mechanical Properties of Q235 Steel and Q460 Steel

Coupon No.	f_y /MPa	f_u /MPa	Δ /%	E /GPa
Q235-1	300.5	451.5	19.5	204.125
Q235-2	314.8	453.2	19.9	203.974
Q235-3	303.6	444.0	20.1	203.829
Mean value	306.3	449.6	19.8	203.976
Q460-1	539.3	609.5	13.5	208.792
Q460-2	534.6	615.1	14.8	207.189
Q460-3	527.2	595.8	16.8	206.509
Q460-4	551.6	620.1	13.2	210.379
Q460-5	537.7	614.9	12.9	209.843
Mean value	538.1	611.1	14.2	208.542

3. TEST PROGRAM

A comprehensive test program was designed to undertake residual stress measurements after exposing welded box-shape section to high temperature conditions. The tests were carried out in two stages, namely, heating and cooling stage, on stub columns in an electric furnace, and then measurement of residual stress in specimens after post-temperature exposure condition, as well as at ambient temperature, by means of sectioning method.

3.1 Method of Measurement

Both destructive and non-destructive methods are adopted for determining residual stresses in structural members. X-ray, neutron or electron diffraction, ultrasonic methods and magnetic methods are grouped under non-destructive methods [13]. Sectioning method, grouped under destructive method, and commonly used for measuring residual stresses in structural steel members, was adopted to measure residual stresses in the current study.

3.2 Test Specimens

The residual stress distribution in stub columns fabricated with welded box-section is investigated in this study. The dimension of steel box sections used for tests are □200 mm× 200 mm × 8 mm× 8 mm, and the columns were fabricated with mild Q235 steel and high strength Q460 steel. The filled weld leg is of 8 mm thickness. For the welding, manual metal arc welding was used, and the shielding gasses were of CO_2. The voltage of the welding gun was 25V, the amps were 230A and the welding velocity was about 35 cm/min. The filler wire type for welding was JM-60, with yield strength of 545MPa, and elongation after fracture at 25%. The welding procedure as per Chinese standard JGJ81-2002 [15] was followed. The columns were of 1000 mm length and were cold-sawed into three segments in order to minimize end effects on residual stress results. Only the middle segment, with a length of 280 mm, was used to measure the residual stress (as shown in Figure 3a). A total of 10 specimens were prepared for tests (shown in Figure 3b). Two specimens were tested at room temperature (labeled as □235-20 and □460-20) and the remaining eight specimens (labeled as □235-200, □235-400, □235-600, □235-800, □460-200，□460-400，□460-600 and □460-800) were tested after exposure to four target temperatures, namely 200℃, 400℃, 600℃ and 800℃. A unique label identification system is adopted for the specimens. For example, □235-400, where □ denotes the section shape, the next three digits represent steel nominal yield strength in N/mm^2, and the following three digits refer to the target temperature.

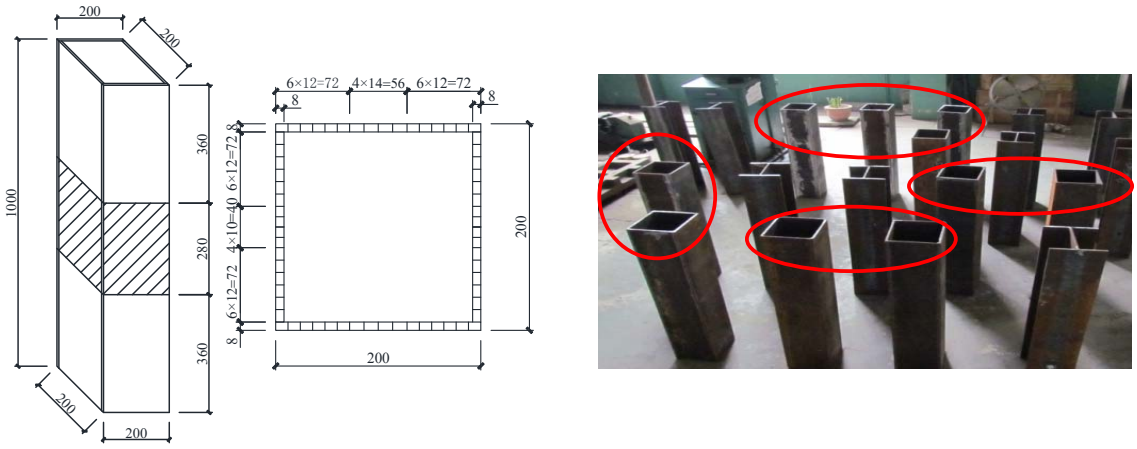

(a) Dimensions of specimen (b) View of specimens prior to testing

Figure 3. Dimension and Photo of Test Specimens

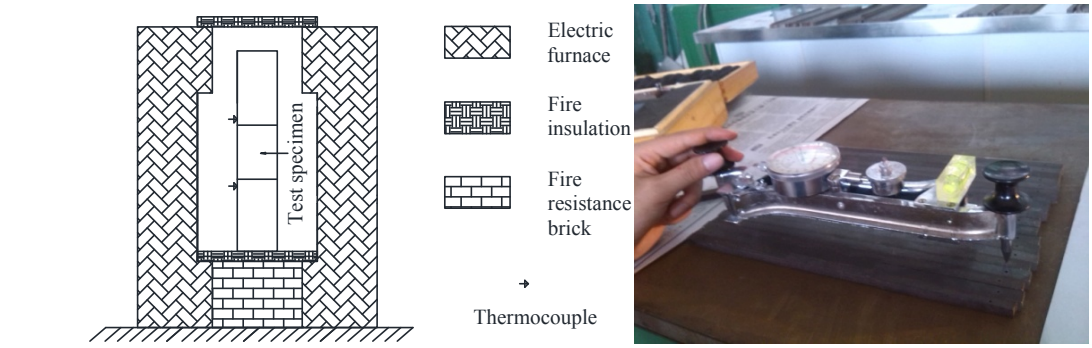

(a) Furnace and layout of specimen (b) Hand-held strain gauge for measuring strains

Figure 4. Test set-up for High Temperature Exposure and Measurement

3.3 Test Set-Up

The test set-up comprised of an electric furnace (as shown in Figure 4a), a wire-cutting machine and a hand-held strain gauge (as shown in Figure 4b). The electric furnace consists of a cylindrical chamber with a maximum heating length of 1500 mm, and is capable of generating temperatures up to 1,100 ℃ at a pre-specified rate of temperature rise. Two built-in thermocouples are mounted inside the specimen to measure temperatures at upper and lower zone of middle segment of specimens and the average readings of these two thermocouples is taken as the specimen temperature.

3.4 Test Procedure

The following procedures were adopted for undertaking tests on specimens.

(1) Fire exposure

An electric furnace was utilized to heat the specimen to a specified target temperature as described above. In an actual fire incident, the time-temperature growth in a steel member, both during the heating and cooling stages of a fire, can be highly variable. In this study, however, only one time-temperature exposure was considered, in which the section is heated to a target temperature

and then cools down naturally in air. The time-temperature curves, the specimens were subjected to during the heating phase and cooling phase is plotted in Figure 5.

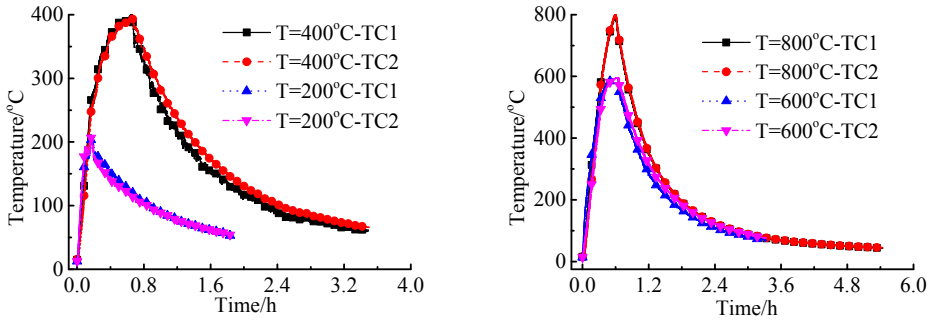

(a) Target temperature of 200-400℃ (b) Target temperature of 600-800℃

Figure 5. Temperature-time Curve of Specimen during Fire Exposure

(2) Gauge holes drilling

Before drilling gauge holes, the specimens were cleaned to remove any rust deposited on the surface of steel by polishing the surface (shown in Figure 6a). After cleaning, cutting lines were drawn on the surface to mark the boundary of strips and a sign is marked on each strip. The dimension of each trip is shown in Figure 3a. In order to compensate any influence of temperature variation on the measured strain, a reference bar was fabricated to consider the strain induced by temperature variation. Finally, gauge holes were drilled on the sectioned segment with a strain gauge length of 250 mm.

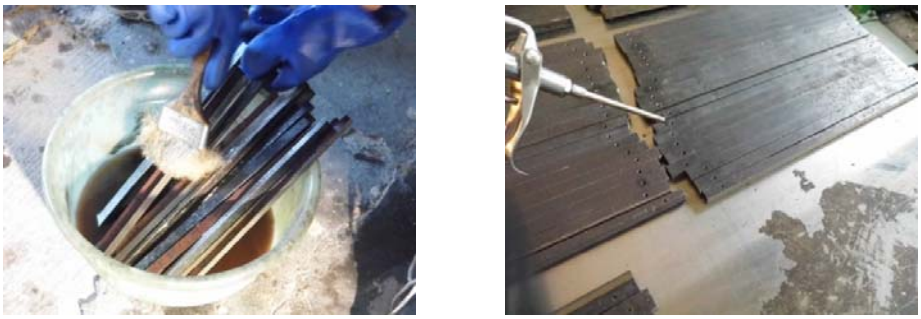

(a) Dust cleaning on strips (b) Gauge hole cleaning

Figure 6. Photos of Specimen Strips Cleaning

(3) Gauge length measurement

Any dust accumulated on the gauge holes was cleaned (shown in Figure 6b), and then the length of standard strips, temperature compensating strips and the distance between gauge holes were measured. Average of three measurements was taken as the finial value. Utilizing the difference of standard trip and temperature compensating segment and sectioned strips, the length of temperature compensating segment and gauge holes was calculated. When the difference of three measurements exceeded 0.015 mm, the measurements were abandoned and re-measurements were taken. Otherwise, the average value of three measurements was taken as the gauge length of temperature compensating segment (L_{T1}) and sectioned trips (L_1).

(4) Cutting of strips

The column was cut into three segments along the lines on the surface of the column, and then the sectioning segment was cut into many strips. Finally, the coolant on the surface and gauge holes of strips was cleaned.

(5) Gauge length measurement after sectioning

Similar to the procedure used in step (2), the distance between two gauge holes on each strip and the length of temperature compensating segment was measured again to obtain the new length after the residual stresses release and temperature change. The average value of three measurements was taken to be the gauge length of temperature compensating segment (L_{T2}) and sectioned trips (L_2).

(6) Residual stress calculations
Based on the measured results in step (2) and (4), the strain of temperature compensating segment was obtained as $\varepsilon_T = (L_{T2} - L_{T1}) / L_{T1}$; and the strain in strip was calculated as $\varepsilon = (L_2 - L_1) / L_1$. The bending deformation in the strip was modified using the following equation:

$$\bar{\varepsilon} = \varepsilon + (f/l)^2 / (6(f/l)^4 + 1) \quad (1)$$

where f is deflection in strips at mid-span and l is length of the strip.

The strain generated by residual stress release was obtained by subtracting temperature compensating strain from the total strain of strip, as $\varepsilon_r = \bar{\varepsilon} - \varepsilon_T$. According to Hooke's law, the residual stress on each trip was obtained as $\sigma_r = E\varepsilon_r$.

4. TEST RESULTS AND COMPARISON

Data generated from above tests was utilized to develop residual stress distribution of box-shaped steel sections made of Q235 steel and Q460 steel, after exposure to various temperatures.

4.1 Test Results

The difference in the length of each strip measured before and after sectioning was utilized to evaluate the residual stress as the product of released strain and elastic modulus and the resulting stresses is plotted in Figure 7, both for mild Q235 steel and for Q460 steel specimens. It can be seen from the figure that the residual stress in Q460 steel section is higher than that in Q235 steel at room temperature or after exposure to a given temperature. This can be mainly attributed to the fact that the mechanical properties of these two steels are different and higher the nominal yield strength of steel is, the higher the residual stress that develops. In addition, with increase in exposure temperature, the magnitude of residual stress decreases, irrespective of type of steel (Q235 or Q460).

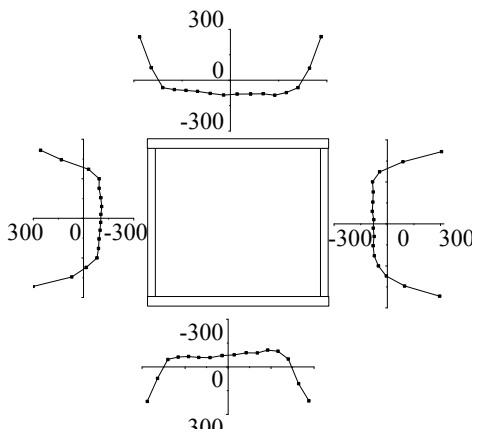

(a) At room temperature (Q235 steel)

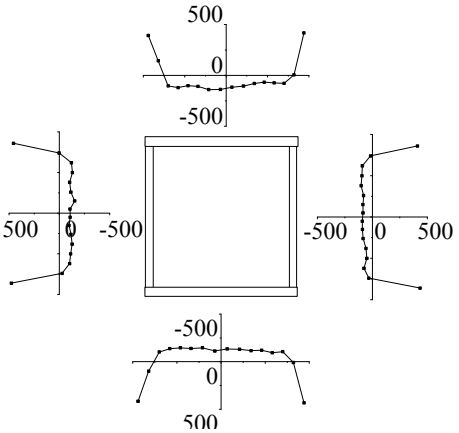

(b) At room temperature (Q460 steel)

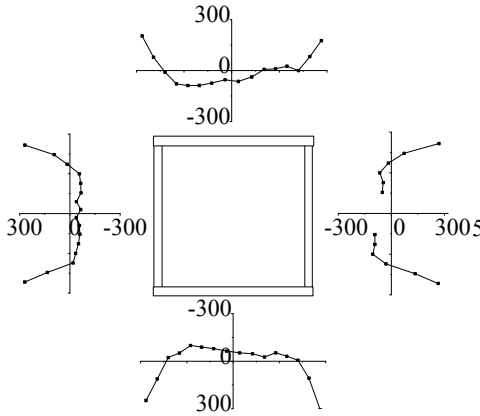

(c) After exposed to 200℃ (Q235 steel)

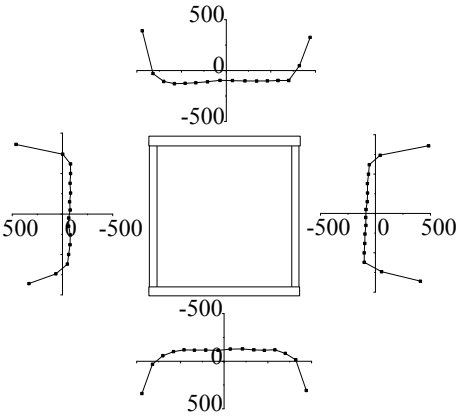

(d) After exposed to 200℃ (Q460 steel)

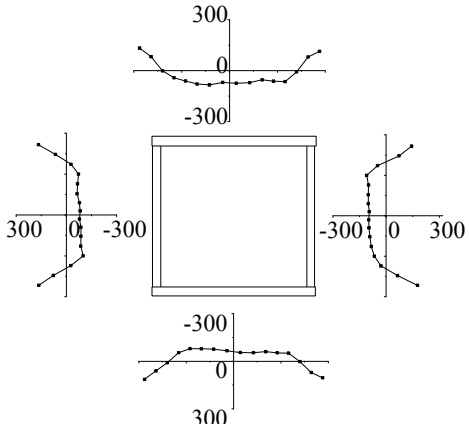

(e) After exposed to 400℃ (Q235 steel)

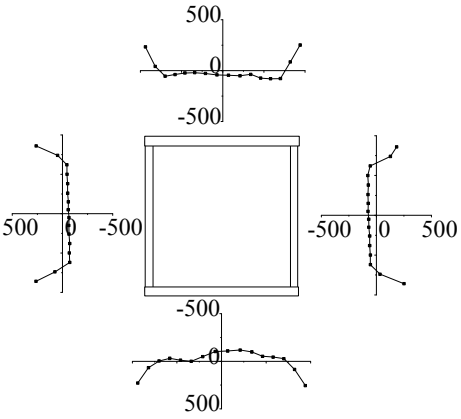

(f) After exposed to 400℃ (Q460 steel)

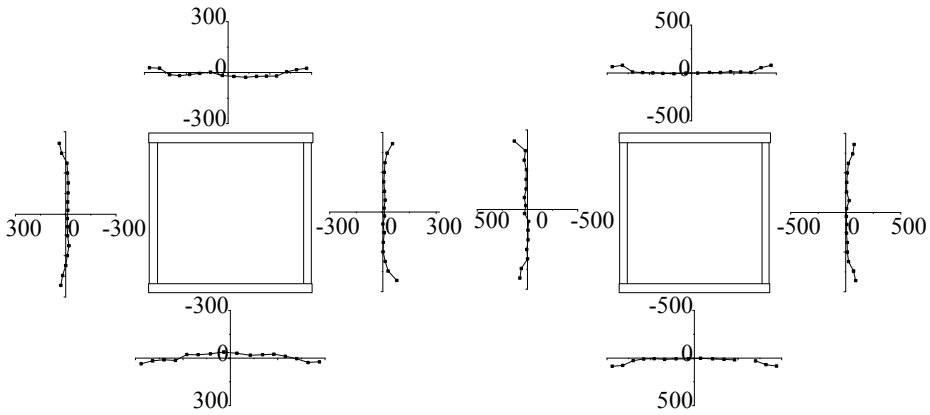

(g) After exposed to 600℃ (Q235 steel) (h) After exposed to 600℃ (Q460 steel)

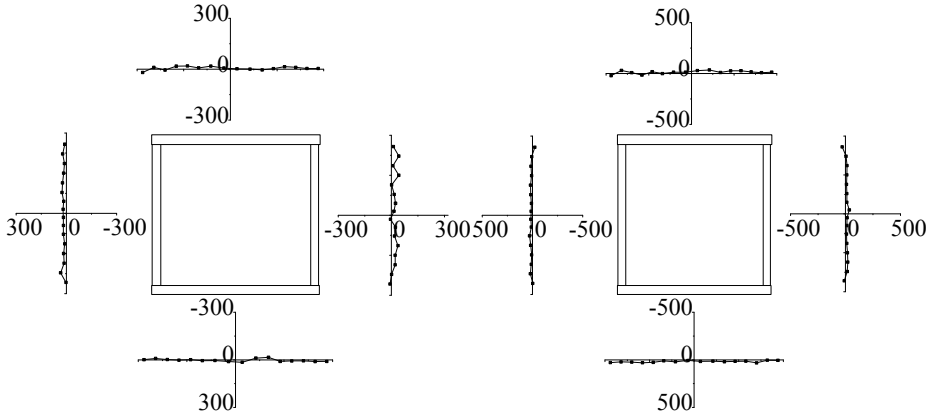

(i) After exposed to 800℃ (Q235 steel) (j) After exposed to 800℃ (Q460 steel)

Figure 7. Residual Stress in Q235 and Q460 Steel Welded Box-shaped Sections after Exposure to Different Temperature

4.2 Comparison of Residual Stress Ratio

In order to compare variation of residual stresses in Q235 and Q460 steel specimens, the ratio of maximum residual stress to nominal yield strength at room temperature and after exposure to 400℃ are plotted in Figure 8. This comparison clearly shows that, the ratio of maximum residual stress to nominal yield strength for Q235 steel is higher than that for Q460 steel. For example, the tensile residual stress ratio decreases from +1.10 to +0.94 for flanges and from +0.45 to +0.32 for webs at room temperature. It is well established that the residual stress to yield strength ratio, rather than the magnitude of residual stress, influence the global and local buckling behavior of steel members. Therefore, the member's ultimate capacity will benefit from the improvement in strength of steel. This conclusion was also reached in reported test results [3].

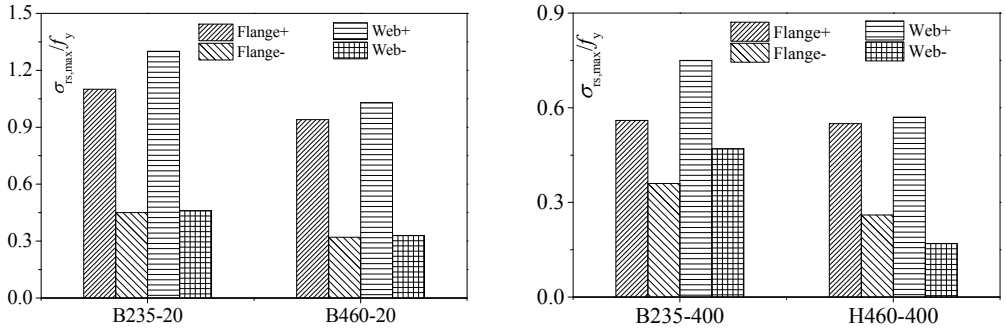

(a) At room temperature (b) After exposed to 400℃

Figure 8. Comparison of Ratio of Maximum Residual Stress to Nominal Yield Strength

4.3 Comparison of Reduction Factors

In order to evaluate the effect of fire exposure on the magnitude of residual stress in welded steel sections, reduction factor of residual stresses, α_1-α_4, are plotted in Figure 9. This reduction factor is defined as the ratio of maximum residual stress (corresponding to tensile or compressive residual stress in flange and web, respectively) after fire exposure to that at room temperature. Data in Figure9 indicate that the reduction factor for residual stress decreases with increased exposure temperature. Moreover, the magnitude of reduction factor in flange and web, for both types of steel, decrease in a similar trend. Taking the temperature of 600℃ as an example, the reduction factor is about 20% for both Q235 steel and Q460 steel specimens.

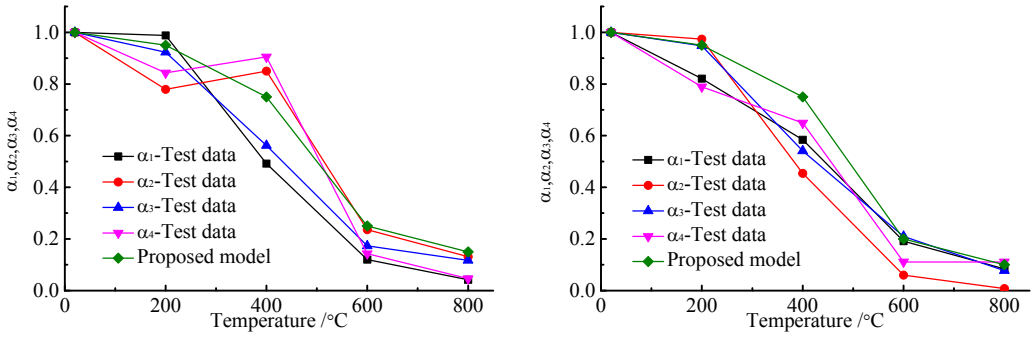

(a) Q235 steel (b) Q460 steel

Figure 9. Reduction Factor of Residual Stress in Welded Box-section

4.4 Comparison with Other Tests

Since direct comparison with the residual stress pattern for the welded box-section after fire exposure was not available, welding residual stress after heat treatment was tested by Jiang et al. [16]. In the test, the specimens made of RQT701 steel with nominal yield stress of 690MPa were put into a furnace for heat treatment. The temperature history during thermal treatment process for test specimens is shown in Figure 10. As can be seen from the figure, the maximum temperature attained in test specimen is approximate 600℃. Therefore, the residual stress of specimen after heat treatment is compared with the results of specimen after being exposed to 600℃ and it is plotted in Figure11. The comparison indicates that the reduction factor of residual stress after heat treatment (RQT701 steel) is higher than that after fire exposure to 600℃ (Q235 and Q460 steel). The can be

attributed to the fact that the welded steel plate used in the test by Jiang et al. [16] is 16mm in thickness, which much thicker than the 8 mm thick plate used in this paper. In addition, the comparison also indicates that the high temperature exposure is as effective to reduce residual stress as heat treatment.

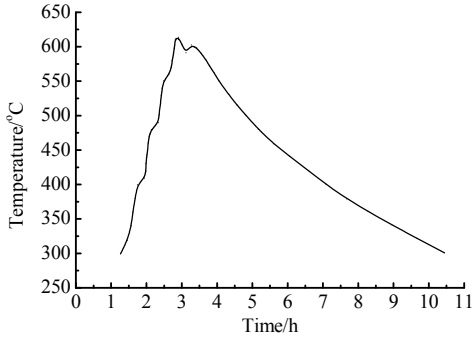

Figure10. Temperature History during Heat Treatment Process

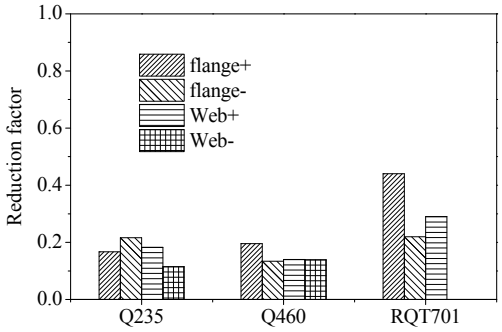

Figure 11. Comparison of Residual Stress after High Temperature Exposure and after Heat Treatment

The measured residual stresses in Q460 steel welded box-section at room temperature is also compared with the available residual stress reported in literature [4] for a similar section dimension, which is B150×150×10×13. The comparison in Figure 12 shows that the distribution patterns are quite similar between different thicknesses of steel plate. However, the maximum magnitude of residual stress for section B200×200×8×8 is higher than those for B150×150×10×13. This may be attributed to the fact that the filled weld leg is similar (8mm) even through plate thickness are different. For the thicker plate, the heat input during welding are relatively higher than that for thinner one. Consequently, it can be concluded that the thickness of plate and filled weld leg have significant effect on the maximum residual stress that develops.

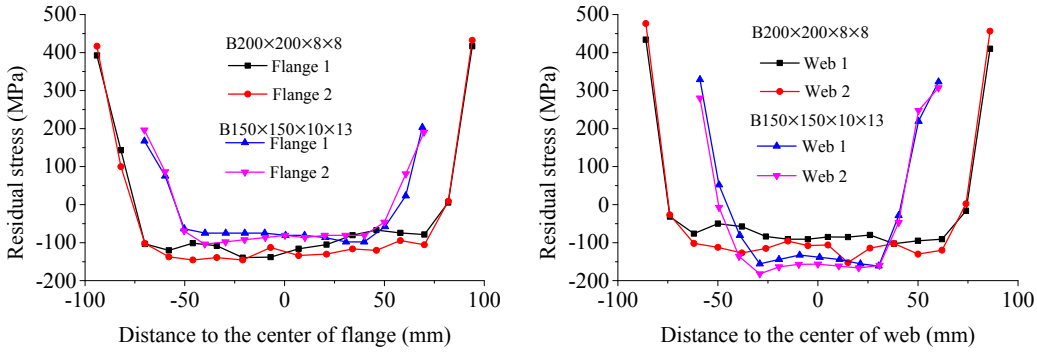

(a) Flange (b) Web

Figure 12. Comparison of Residual Stress in Welded Box Section with Different Plate Thickness

5. ROPOSED RESIDUAL STRESS RELATIONS

The above comparison clearly indicates that grade of steel and exposure temperature play a critical role in determining residual stress distribution in welded steel sections. Thus these two factors are to be accounted for in evaluating residual stress distribution. A simplified relation is developed for accounting these two critical factors in evaluating residual stress. Due to complexity and significant effort involved in undertaking tests at various temperatures for each specimen type, only one cross section was considered in the test. As discussed in section 4.4, the thickness of plate also has some moderate influence on the magnitude of residual stress. Therefore, the residual stress model proposed here is applicable only to box-shaped sections of comparative thicknesses used in the test. In practice, steel plates of 6 mm to 10 mm thickness are used.

5.1 Residual Stress Pattern

For developing simplified relations for temperature induced residual stress of welded steel sections, equation proposed by Ban et al. [4] for room temperature residual stress formed the basis and are modified to account for temperature dependent influencing factors. The distribution pattern is symmetrical about the two axes due to the equilibrium of both axial force and bending moment within the section (as shown in Figure 13). The magnitude of stresses was labeled as follows: constant tensile stress in flanges σ_{frt}, constant compressive stress in flange σ_{frc}, constant tensile stress in webs σ_{wrt} and constant compressive stress in web σ_{wrc}. The multiple stepped functions of the distribution shape in flanges $\sigma_{fr}(x)$ and webs $\sigma_{fr}(y)$ are described in Eq. 2 and Eq. 3, respectively.

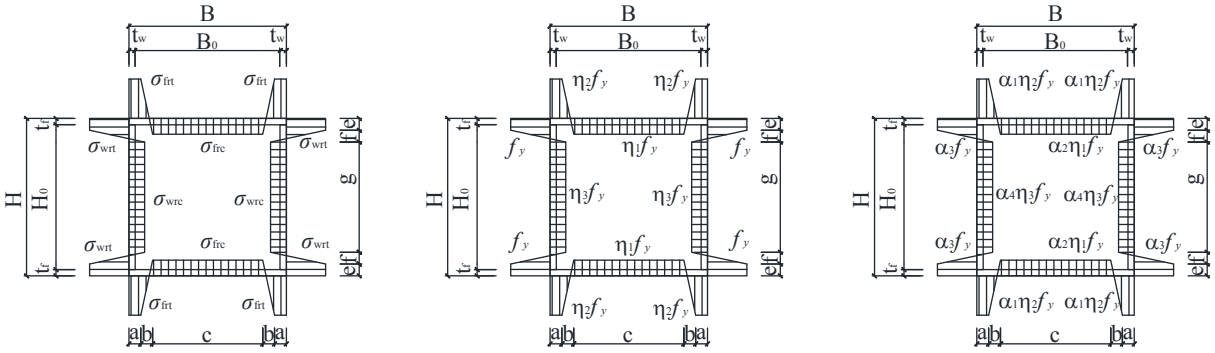

(a) Basic model (b) At room temperature (c) After high temperature exposure

Figure 13. Proposed Distribution Mode of Residual Stress

$$\sigma_{fr}(x)=\begin{cases}\sigma_{frt}, & 0\le x\le a\\ \sigma_{frt}+\dfrac{\sigma_{frc}-\sigma_{frt}}{f}(x-a), & a\le y\le a+b\\ \sigma_{frc}, & a+b\le y\le B/2\end{cases} \tag{2}$$

$$\sigma_{wr}(y)=\begin{cases}\sigma_{wrt}, & 0\le y\le e\\ \sigma_{wrt}+\dfrac{\sigma_{wrc}-\sigma_{wrt}}{f}(y-e), & e\le y\le e+f\\ \sigma_{wrc}, & e+f\le y\le H/2\end{cases} \tag{3}$$

where $a=t+B_0/20$; $c=B-2a-2b$; $d=t_w+6h_f$; $e=H_0/20$; $g=h_0-2e-2f$; $\sigma_{frc}=\eta_1 f_y$; $\sigma_{frt}=\eta_2 f_y$; $\sigma_{wrc}=\eta_3 f_y$; $\sigma_{wrt}=\eta_4 f_y$; For Q235 steel: $\eta_1=\eta_3=0.375$, $\eta_2=1.0$; For Q460 steel: $\eta_1=0.25$, $\eta_2=0.9$, $\eta_3=0.20$; *b and f* can be determined according to equilibrium of residual stress across the entire section.

To incorporate the fire exposure effects, the maximum magnitude of residuals stress at room temperature are modified to account for effect of fire exposure, through four coefficients α_1 toα_4. The results of test data reported in this paper were used to generate value of these coefficients for proposed models (as shown in Table 2).This way the proposed equation accounts for effects of steel type (Q235 and Q460) and temperature exposure (20-800℃). Then the modified equation is extended to predict residual stress by establishing an equivalency between room temperature and after high temperature exposure.

Table 2. Comparison of Measured Stress Coefficient from Proposed Model with Test Data for Specimens

Steel type	Exposure temperature /℃	α_1		α_2		α_3		α_4	
		Test	Model	Test	Model	Test	Model	Test	Model
Q235 steel	200℃	0.988	0.95	0.779	0.95	0.923	0.95	0.843	0.95
	400℃	0.492	0.75	0.850	0.75	0.562	0.75	0.905	0.75
	600℃	0.120	0.25	0.236	0.25	0.173	0.25	0.143	0.25
	800℃	0.042	0.15	0.131	0.15	0.117	0.15	0.046	0.15
Q460 steel	200℃	0.821	0.95	0.974	0.95	0.948	0.95	0.789	0.95
	400℃	0.584	0.65	0.454	0.65	0.541	0.65	0.649	0.65
	600℃	0.191	0.20	0.060	0.20	0.210	0.20	0.111	0.20
	800℃	0.084	0.10	0.008	0.10	0.077	0.10	0.111	0.10

5.2 Validation of Proposed Relations

In order to examine the validity of the above developed residual stress relation, the test data presented in this paper is selected for validation. Predicted residual stress in flange and web are compared against measured data on test specimens. Figure14 and Figure 15 present a comparison of predicted and measured residual stress for Q235 steel sections and Q460 steel sections, respectively. It can be clearly seen that there is a good agreement between the predicted and measured residual

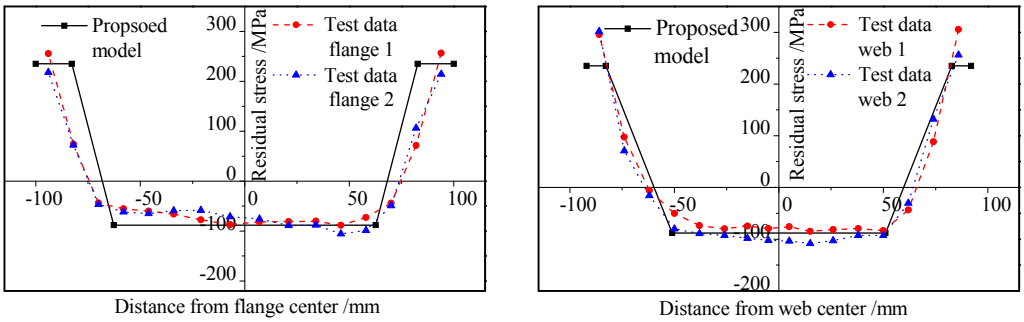

(a) At room temperature

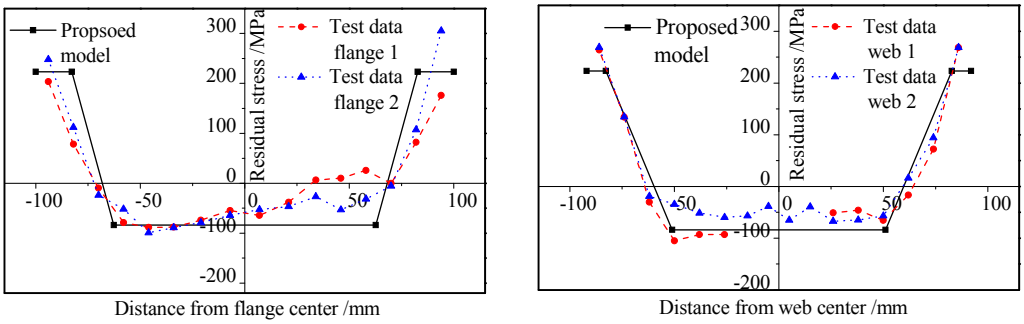

(b) After exposed to 200℃

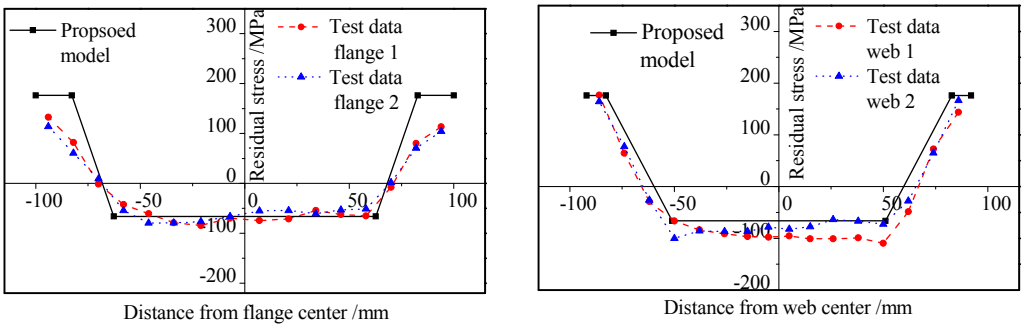

(c) After exposed to 400℃

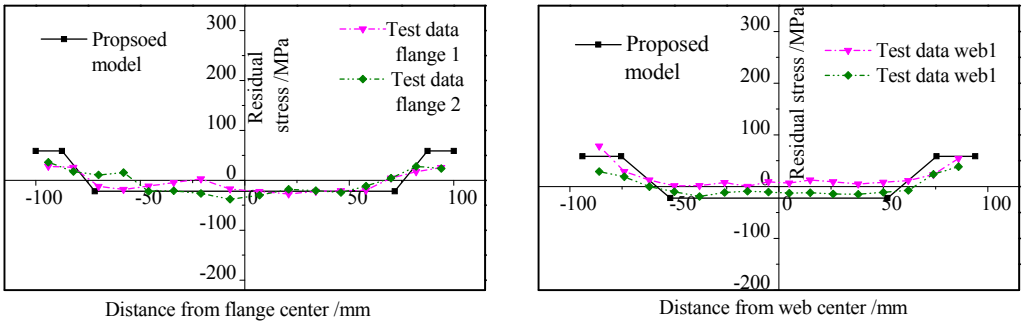

(d) After exposed to 600℃

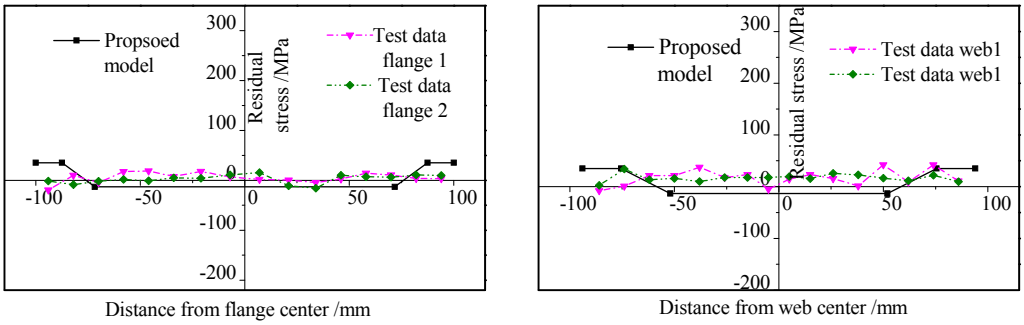

(e) After exposed to 800℃

Figure 14. Comparison of Residual Stress from Proposed Model with Test Data for Q235 Steel Box-section Stress

Hence, it can be inferred that the proposed residual stress relation is capable of reasonably capturing residual stress distribution in welded box-section, both at room temperature and after exposure to elevated temperatures.

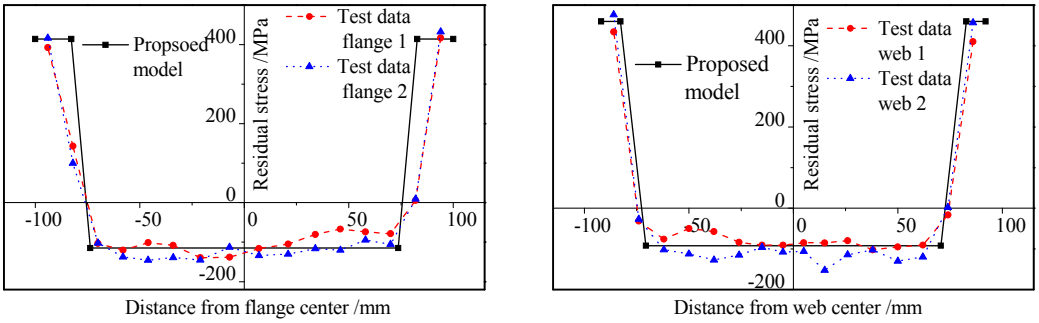

(a) At room temperature

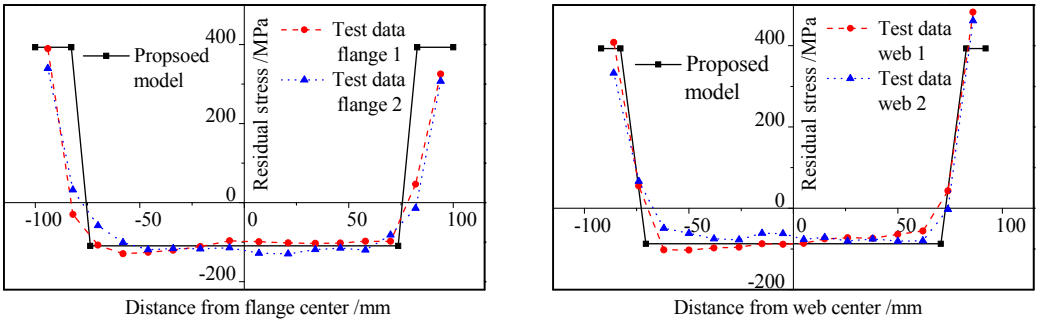

(b) After exposed to 200℃

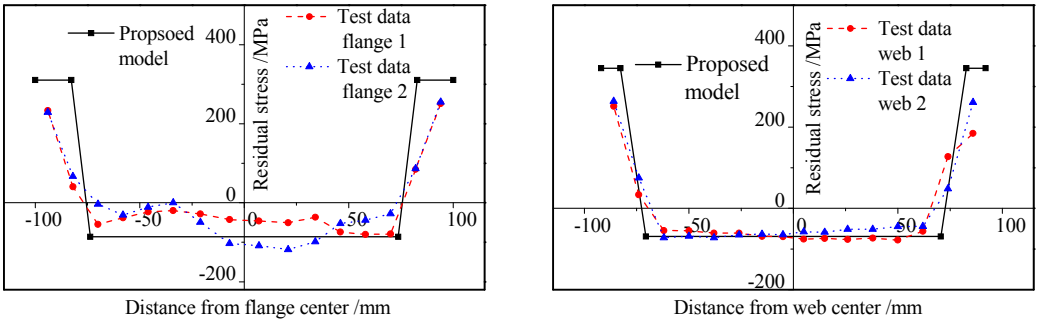

(c) After exposed to 400℃

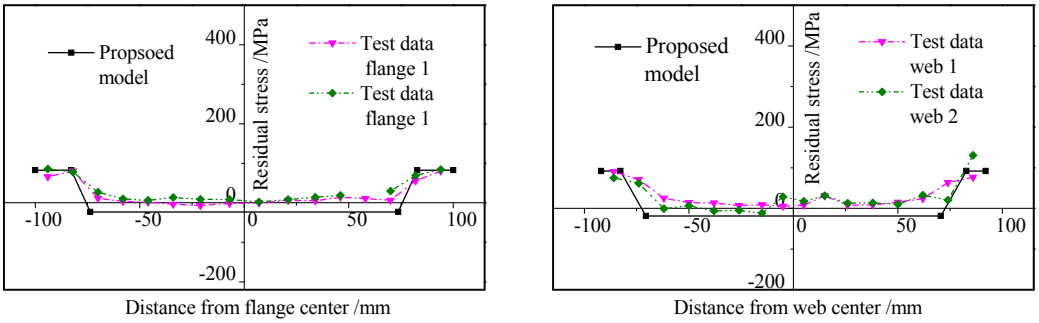

(d) After exposed to 600℃

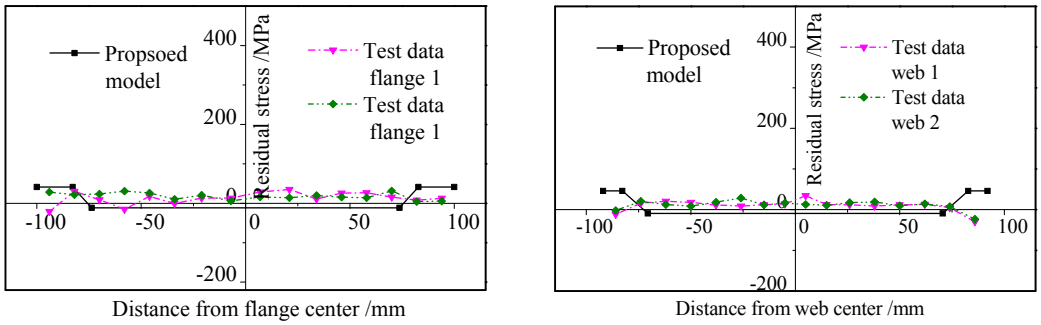

(e) After exposed to 800℃

Figure 15. Comparison of Residual Stress from Proposed Model with Test Data for Q460 Steel Box-section

6. CONCLUDING REMARKS

A total of 10 box-shaped stub columns, made of mild Q235 steel and high strength Q460 steel, were tested to evaluate residual stress at ambient and after high temperature exposure. The specimens were heated to a target temperature and then allowed to cool down naturally. Through these tests the residual stress in different specimens was evaluated. Based on the results from residual stress measurements, the following conclusions can be drawn.

(1) The exposure temperature has significant influence on the magnitude of welding residual stress, and the level of residual stress decrease with an increase in peak exposure temperature.

(2) The residual stress decreases sharply once the exposure temperature exceeds 400℃. Further, the residual stress decreases to 10% of that at ambient conditions when the exposure temperature reaches 800℃.

(3) The temperature induced residual stress in high strength steel (Q460) sections follow the same trend as that in mild steel (Q235) section.

(4) The proposed residual stress relations compares well with test data and can be used to predict temperature induced residual stress in box-sections with plate thickness varying from 6mm to 10mm.

ACKNOWLEDGEMENT

The authors wish to acknowledge the support from the Natural Science Foundation of China (Grant No.: 51678090), National Program on Key Research and Development Project (Grant No.: 2016YFC0701203), the Fundamental Research Funds for the Central Universities (Grant No.: 106112017CDJPT200003) and Michigan State University. Any opinions, findings, and conclusions or recommendations expressed in this paper are those of the authors and do not necessarily reflect the views of the sponsors.

REFERENCE

[1] Tebedge, N. and Tall, L., "Residual Stress in Structural Steel Shapes — A Summary of Measured Values", Fritz Laboratory Report, Lehigh University; 1973.

[2] Wang, W.Y., Liu, B. and Kodur, V.K.R., "Effect of Temperature on Strength and Elastic Modulus of High Strength Steel", Journal of Materials in Civil Engineering, 2013, Vol. 25, No. 2, pp. 174-182.

[3] Wang, Y.B., Li, G.Q. and Chen, S.W., "The Assessment of Residual Stresses in Welded High Strength Steel Box Sections", Journal of Constructional Steel Research, 2012, Vol. 76, pp.93-99.

[4] Ban, H.Y., Shi, G. and Shi, Y.J. et al., "Residual Stress of 460 MPa High Strength Steel Welded Box Section : Experimental Investigation and Modeling", Thin-walled Structures 2013, Vol. 64, pp. 73-82.

[5] Li, T.J., Li, G.Q. and Wang, Y.B., "Residual Stress Tests of Welded Q690 High-strength Steel Box- and H-sections", Journal of Constructional Steel Research, 2015, Vol. 115, pp.283-289.

[6] Ma, J.L., Chan, T.M. and Young, B., "Material Properties and Residual Stresses of Cold-formed High Strength Steel Hollow Sections", Journal of Constructional Steel Research, 2015, Vol. 109, pp. 152-165.

[7] Khan, M., Paradowska, A. and Uy, B., et al., "Residual Stresses in High Strength Steel Welded Box Sections", Journal of Constructional Steel Research, 2016, Vol. 116, pp. 55-64.

[8] Wang, W.Y., Li, G.Q. and Ge, Y., "Residual Stress Study on Welded Section of High Strength Q460 Steel after Fire Exposure", Advanced Steel Constructions, 2015, Vol. 11, No. 2, pp. 150-164.

[9] GB/T 2975-1998 Steel and Steel Products: Location and Preparation of Test Pieces for Mechanical Testing, Beijing: China Standard Press, 1998 (in Chinese).

[10] GB/T 228-2002 Metallic Materials: Tensile Testing at Ambient Temperature, Beijing: China Standard Press, 2002 (in Chinese).

[11] Wang, W.Y., Liu, T.Z. and Liu, J.P., "Experimental Study on Post-fire Mechanical Properties of High Strength Q460 Steel". Journal of Constructional Steel Research, 2015, Vol. 114, pp. 100–109.

[12] Zhang, Y.J., Zhu, Y., Zhao, S. and Hu, K.X., "Experimental Research on Mechanical Properties of Steel Cooled in Different Modes after High Temperature Treatment", Structural Engineers, 2009, Vol. 25, No. 5, pp. 104–109 (in Chinese).

[13] Cruise, R.B. and Gardner, L., "Residual Stress Analysis of Structural Stainless Steel Sections", Journal of Constructional Steel Research, 2008, Vol. 64, pp. 352–66.

[14] Tebedge, N., Alpsten, G. and Tall, L., "Residual-stress Measurement by the Sectioning Method", Exp. Mech., 1973, Vol. 13, pp. 88–96.

[15] JGJ81-2002, Technical Specification for Welding of Steel Structure of Building, Beijing: China Architecture & Building Press, 2002 (in Chinese).

[16] Jiang, J., Chiew, S.P., Lee, C.K. and Tiong, P.L.Y., "An Experimental Study on Residual Stresses of High Strength Steel Box Columns", Journal of Constructional Steel Research 2017, Vol. 130, pp. 12–21.

A CO-ROTATIONAL FRAMEWORK FOR QUADRILATERAL SHELL ELEMENTS BASED ON THE PURE DEFORMATIONAL METHOD

Y.Q. Tang, Y. P. Liu*, and S. L. Chan

Department of Civil and Environmental Engineering,
The Hong Kong Polytechnic University, Hong Kong, China;
**(Corresponding author: E-mail:yp.liu@polyu.edu.hk)*

Received: 18 August 2017; Revised: 10 October 2017; Accepted: 19 October 2017

ABSTRACT: In this paper, a novel co-rotational framework for quadrilateral shell element allowing for the warping effect based on the pure deformational method is proposed for geometrically nonlinear analysis. This new co-rotational framework is essentially an element-independent algorithm which can be combined with any type of quadrilateral shell element. As the pure deformational method is adopted, the quantities of the shell element can be reduced, such that it needs less computer storage and therefore enhances the computational efficiency. In the proposed framework, the geometrical stiffness is derived with a clear physical meaning and regarded as the variations of the nodal internal forces due to the motions and deformations of shell element. Furthermore, the warping effect of quadrilateral shell element is considered, and for this reason, the structures undergoing significant warping can be efficiently solved by the proposed formulation. Finally, several benchmark examples are used to verify the validation and accuracy of the proposed method for geometrically nonlinear analysis.

Keywords: element-independence, co-rotational method, flat quadrilateral shell element, pure deformation, geometrically nonlinear analysis, explicit tangent stiffness

DOI: 10.18057/IJASC. 2018.14.1.6

1. INTRODUCTION

Shell structures and steel frames made up of thin-wall members are commonly used in civil and structural engineering. Generally, it needs huge computer time to analyze a structure by finite shell elements compared with beam-column elements, especially in nonlinear analyses. Thus, the development of shell elements with high performance as well as the co-rotational framework with improved computational efficiency continuously attracts the attention of many researchers.

There are three common methods based on the Lagrangian kinematic description for geometrically nonlinear analyses, i.e. total Lagrangian (TL), updated Lagrangian (UL) and co-rotational approaches. The last method is latest and attracts more attention than the others recently due to its simplicity and efficiency. The basic idea of the co-rotational method is that the total motions of an element can be divided into two parts, including the rigid body motions and the pure deformations. To decompose them, a local frame is attached to and co-rotated with the element. Then, the translations and rotations of the local frame are taken as the rigid body movements, while the deformations of the element produced in the local frame are regarded as the pure deformations. In reality, the classification of the Lagrangian kinematic descriptions for geometrically nonlinear analysis is not absolute. The co-rotational approach can be incorporated with either the total Lagrangian (TL) or the updated Lagrangian (UL) formulations. In the following, some research works related to the co-rotational description are discussed.

The co-rotational approach was firstly introduced by Wempner [1] and further developed by authors (Belytschko and Hsieh [2]; Belytschko *et al.* [3]). After almost 50 years' development,

many versions of co-rotational approaches have been proposed for different kinds of finite elements. The difference of them lies in the treatment of large rotations, simplification of procedure, derivation of geometrical stiffness, definition of local coordinate system, consideration of large strains and so on. The concept of "element-independent co-rotational (EICR) formulation" was first introduced by Rankin and Brogan [4] in 1986. By this formulation, the existing linear finite elements can be easily extended to geometrically nonlinear analysis. Basically, the property of the element-independence comes from that the geometrical stiffness formulated by local coordinates and nodal internal forces at current configuration is explicit, so there is no need to conduct numerical integration over the element. The geometrical stiffness is independent of the local element and therefore any linear element can be extended to geometrically nonlinear analysis with this co-rotational algorithm. Rankin and Brogan [4] presented the EICR algorithm as a general framework, then authors (Rankin and Nour-Omid [5]; Nour-Omid and Rankin [6]) pointed out that the element-independent approach presented in reference (Rankin and Brogan [4]) cannot keep the internal force filed self-equilibrium and further proposed a projector operator to improve its performance. In addition, due to the non-additive nature of large rotations in a three-dimensional space, a pertaining transformation matrix was presented in reference (Nour-Omid and Rankin [6]). The detailed derivation of the EICR method also can be found in references (Crisfield [7]; Felippa and Haugen [8]), in which Felippa and Haugen [8] introduced several related techniques, such as the mathematics of finite rotations, the fitting methods to satisfy invariance to nodal ordering and so on. The pertaining studies and applications for shell elements also can be found in references (Pacoste [9]; Skallerud and Haugen [10]; Eriksson and Pacoste [11]; Battini and Pacoste [12]; Battini and Pacoste [13]). Another similar co-rotational procedure used for a flat triangular shell element was proposed by authors (Levy and his co-workers Levy and Gal [14]; Gal and Levy [15]; Levy and Spillers [16]), in which the derivation of the geometrical stiffness matrix is derived with the load perturbation of the linear equilibrium equations in its local coordinates system.

Crisfield and Moita [17] presented a unified co-rotational framework for solids, shells and beams, which has strong links with the work done by Nour-Omid and Rankin [6] and inherits the merit of element-independence. It can be regarded as a simplified version since some terms are omitted in the derivation of the internal forces and the tangent stiffness. In addition, Crisfield *et al.* [18] pointed out that the co-rotational technique is restricted in the local element with small strains and can be extended to problems with large strains, in which the local element adopted Biot-stress formulation. Similar to this simpler co-rotational framework, Izzuddin [19] defined a new local co-rotational system and adopted vectorial rotation for quadrilateral shell elements, through which not only the invariance to node ordering but also a symmetric tangent stiffness matrix can be achieved. Pertaining studies on shell elements with this co-rotational framework were also presented in references (Li and Vu-Quoc [20]; Li *et al.* [21]; Li *et al.* [22]; Li *et al.* [23]; Li *et al.* [24]; Izzuddin and Liang [25]; Li *et al.* [26]).

Also, the co-rotational concept can be integrated with the TL or UL formulation, in which the local tangent stiffness matrix is still obtained through the standard TL or UL formulation described by Bathe [27], while the internal forces are evaluated by the co-rotational approach. For example, based on the geometrically nonlinear flat triangular shell element proposed by Bathe and Ho [28] which is restricted to small rotations between two load steps, Hsiao Kuo-Mo [29] removed the restriction by using the co-rotational approach to eliminate the rigid body motions of the element and get the internal forces. The similar studies of the co-rotational TL or UL formulation for shell elements also can be found in references (Jiang *et al.* [30]; Hsiao [31]; Tang *et al.* [32]).

The pure deformational method, also called natural mode method, was firstly proposed by Argyris *et al.* [33] in the late 1960s, in which the pure deformation modes are separated from the rigid body movements of the local element. This method has substantial computational advantages, since,

when the rigid body movement is removed, the quantities based on the basic coordinate system are less and the formulation is simpler. The pure deformation method has been widely used in the derivations of beam-column elements. Taking a two-node beam-column element in a plane for example, it has three degrees of freedom (two rotations and one translation) per node and then produces a 6×6 singular stiffness matrix. However, if using the pure deformational method, the element only has three degrees of freedom (two rotations and one translation) and deduces a 3×3 non-singular matrix with simpler expression. Thus, the benefits of the pure deformational method are remarkable. Furthermore, it is an element-independent approach and can be applied to many kinds of beam-column elements. For instance, Chan [34] investigated a cubic beam-column element with second-order effect in the large deflection analysis; Chan and Zhou [35] proposed a fifth-order polynomial beam-column element with second-order effect; Tang *et al.* [36] presented a cubic beam-column element allowing for shear deformation and second order effect simultaneously; similarly, the stability function can be derived through the pure deformational element model as investigated by Chan and Gu [37]. The studies of the pure deformational method for shell elements are also useful, but rare, which motivates the authors to explore. And the related work for flat triangular shell elements was also proposed by authors (Tang *et al.* [38]).

In this paper, a novel pure deformational method for quadrilateral shell elements is proposed. Unlike beam-column elements, the pure deformational formulation becomes more complicated in shell elements. To construct a flat quadrilateral shell element, significant attention should be paid to the warping phenomenon which is taken into accounted in this study. In addition, a novel co-rotational framework for quadrilateral shell elements in the geometrically nonlinear analysis is proposed. This new framework belongs to the EICR algorithm and is consistent with the pioneering work done by authors (Nour-Omid and Rankin [6] and Levy and Gal [14]). Unlike the previous studies, the proposed co-rotational algorithm is on the basis of the proposed pure deformational method. The outline of the paper is arranged in the following. The pure deformational formulation of the flat quadrilateral shell element consisting of a membrane and a plate element is proposed in Section 2. Then, the novel EICR algorithm integrated with the pure deformational method is detailed in Section 3. Finally, Section 4 shows several benchmark problems to verify the accuracy of the proposed co-rotational framework with a typical flat quadrilateral shell element for geometrically nonlinear analysis.

2. PURE DEFORMATION SHELL ELEMENT MODEL

The pure deformational element model is constructed on the basic coordinate system and its stiffness matrix should get rid of the restrained degrees of freedom. To assemble the global stiffness matrix, it requires two-step transformations. The first step is the transformation from a basic coordinate system to a local coordinate system, while the second step is the transformation from a local coordinate system to a global coordinate system. The second transformation can follow a standard procedure in the literature or textbooks, while the first transformation is new and will be firstly introduced in this section.

2.1 Local and Basic Coordinate Systems

As shown in Figure 1, *XYZ* refers to the global coordinate system while *xyz* is the local coordinate system. In the local coordinate system, the origin is located at node 1, and the local *x*-axis is aligned to side 1-2 of the shell element, with the local *z*-axis being the normal of the plane 1-2-4. To consider the warping phenomenon, it is convenient to make the nodes 1, 2 and 4 coplanar and therefore the warpage happens at the node 3 only.

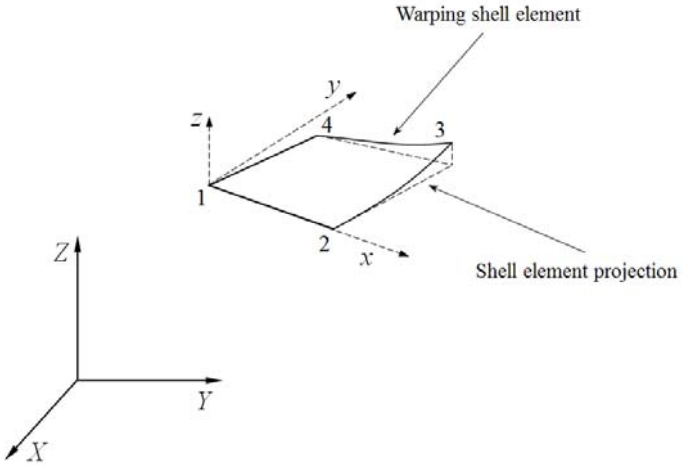

Figure 1. Local Coordinate System

With known the global coordinates of the 4 corner nodes of the shell element, $\boldsymbol{X}_i = \{X_i, Y_i, Z_i\}^T$, i=1,2,3,4, the three triad vectors of the local coordinate system can be given by,

$$\boldsymbol{e}_x = \frac{\boldsymbol{X}_2 - \boldsymbol{X}_1}{\|\boldsymbol{X}_2 - \boldsymbol{X}_1\|} \tag{1a}$$

$$\boldsymbol{e}_z = \frac{\boldsymbol{e}_x \times (\boldsymbol{X}_4 - \boldsymbol{X}_1)}{\|\boldsymbol{e}_x \times (\boldsymbol{X}_4 - \boldsymbol{X}_1)\|} \tag{1b}$$

$$\boldsymbol{e}_y = \boldsymbol{e}_z \times \boldsymbol{e}_x \tag{1c}$$

and then the transformation matrix from local to global system can be expressed as,

$$\boldsymbol{T} = \left[\boldsymbol{e}_x \ \boldsymbol{e}_y \ \boldsymbol{e}_z\right]^T \tag{2}$$

The local coordinates of the four corner nodes can be obtained as,

$$\boldsymbol{x}_i = \boldsymbol{T}\left(\boldsymbol{X}_i - \boldsymbol{X}_1\right) \tag{3}$$

in which $\boldsymbol{x}_i = \{x_i, y_i, z_i\}^T$, i=1,2,3,4. Although this definition of the local coordinate system brings nodal ordering dependency, it can be applied to many cases except for some stability problems with symmetry (Battini and Pacoste [12]). More importantly, this definition is convenient to establish the basic coordinate system corresponding to the pure deformational element model.

There is no difference in nodal coordinates between the local and basic coordinate systems. However, the displacement vector and the internal force vector should remove the entries related to rigid body motions when the shell element degenerates from the local coordinate system to the basic one.

According to Eq. (3) and considering warping phenomenon at the node 3, the nodal coordinates in both the local and basic coordinate systems are given by,

$$\boldsymbol{x}_1 = \{0,0,0\}^T,\ \boldsymbol{x}_2 = \{x_2,0,0\}^T,\ \boldsymbol{x}_3 = \{x_3,y_3,z_3\}^T,\ \boldsymbol{x}_4 = \{x_4,y_4,0\}^T \tag{4}$$

where the six zero entries in Eq. (4) mean that the corresponding degrees of freedom are restrained in the basic coordinate system.

The displacement vector $\boldsymbol{u}$ and the internal force vector $\boldsymbol{f}$ of the shell element in the local coordinate system are represented by,

$$\boldsymbol{u} = \{\boldsymbol{u}_1^T, \boldsymbol{u}_2^T, \boldsymbol{u}_3^T, \boldsymbol{u}_4^T\}^T \tag{5a}$$

$$\boldsymbol{f} = \{\boldsymbol{f}_1^T, \boldsymbol{f}_2^T, \boldsymbol{f}_3^T, \boldsymbol{f}_4^T\}^T \tag{5b}$$

$$\boldsymbol{u}_i = \{ux_i, uy_i, uz_i, \theta x_i, \theta y_i, \theta z_i\}^T \tag{5c}$$

$$\boldsymbol{f}_i = \{fx_i, fy_i, fz_i, mx_i, my_i, mz_i\}^T \tag{5d}$$

For the membrane element with drilling rotation, the displacement vector $\boldsymbol{e}_m$ and the corresponding internal force vector $\boldsymbol{p}_m$ in the basic coordinate system are defined by,

$$\boldsymbol{e}_m = \{ex_2, ex_3, ey_3, ex_4, ey_4, \varphi z_1, \varphi z_2, \varphi z_3, \varphi z_4\}^T \tag{6a}$$

$$\boldsymbol{p}_m = \{px_2, px_3, py_3, px_4, py_4, nz_1, nz_2, nz_3, nz_4\}^T \tag{6b}$$

For the plate element, the displacement vector $\boldsymbol{e}_p$ and the corresponding internal force vector $\boldsymbol{p}_p$ in the basic coordinate system are given by,

$$\boldsymbol{e}_p = \{ez_3, \varphi x_1, \varphi y_1, \varphi x_2, \varphi y_2, \varphi x_3, \varphi y_3, \varphi x_4, \varphi y_4\}^T \tag{7a}$$

$$\boldsymbol{p}_p = \{pz_3, nx_1, ny_1, nx_2, ny_2, nx_3, ny_3, nx_4, ny_4\}^T \tag{7b}$$

Note that each vector of the membrane and plate elements has only nine entries. Thus, the displacement vector $\boldsymbol{e}$ and the internal force vector $\boldsymbol{p}$ of the shell element defined in the basic coordinate system can be expressed as follows,

$$\boldsymbol{e} = \{\boldsymbol{e}_m^T, \boldsymbol{e}_p^T\}^T \tag{8a}$$

$$\boldsymbol{p} = \{\boldsymbol{p}_m^T, \boldsymbol{p}_p^T\}^T \tag{8b}$$

2.2 Transformation between Local and Basic Coordinate Systems

Focusing on the local coordinate system at first, the shell element has a virtual displacement vector $\delta\boldsymbol{u}$. Then, the variations of rigid body rotations of the element in the local coordinate system can be written as follows,

$$\delta\omega_x = \frac{\delta uz_4 - \delta uz_1}{y_4} - \frac{\delta uz_2 - \delta uz_1}{y_4}\frac{x_4}{x_2} \tag{9a}$$

$$\delta\omega_y = -\frac{\delta uz_2 - \delta uz_1}{x_2} \tag{9b}$$

$$\delta\omega_z = \frac{\delta uy_2 - \delta uy_1}{x_2} \tag{9c}$$

Thus, as shown in Figure 2, the variations of the pure deformations of the membrane element with boundary conditions can be given by,

$$\delta ex_2 = \delta ux_2 - \delta ux_1 \tag{10a}$$

$$\delta ex_3 = \delta ux_3 - \delta ux_1 + y_3\delta\omega_z - z_3\delta\omega_y \tag{10b}$$

$$\delta ey_3 = \delta uy_3 - \delta uy_1 - x_3\delta\omega_z + z_3\delta\omega_x \tag{10c}$$

$$\delta ex_4 = \delta ux_4 - \delta ux_1 + y_4\delta\omega_z \tag{10d}$$

$$\delta ey_4 = \delta uy_4 - \delta uy_1 - x_4\delta\omega_z \tag{10e}$$

$$\delta\varphi z_i = \delta\theta z_i - \delta\omega_z \quad (i=1,2,3) \tag{10f}$$

in which the warping in the node 3 is taken into account in Eqs. (10b, c).

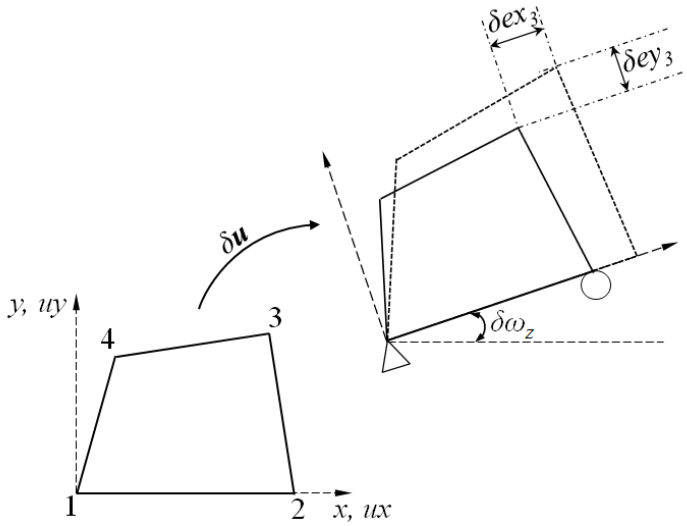

Figure 2. Deformations and Movements of Membrane Element

Then, the transformation matrix for the membrane element from local to basic coordinate system can be derived as,

$$\boldsymbol{L}_m = \frac{\partial \boldsymbol{e}_m}{\partial \boldsymbol{u}^T} \tag{11a}$$

$$\delta \boldsymbol{e}_m = \boldsymbol{L}_m \delta \boldsymbol{u} \tag{11b}$$

where $\boldsymbol{L}_m$ is a 9×24 matrix. By the principle of conjugation, the relationship of the internal force vectors between these two different systems can be given by

$$\boldsymbol{f} = \boldsymbol{L}_m^T \boldsymbol{p}_m \tag{12}$$

Similarly, as shown in Figure 3, the pure deformations of the plate element with boundary conditions to eliminate rigid body motions of the element can be deduced in the following,

$$\delta ez_3 = \delta uz_3 - \delta uz_1 - y_3 \delta \omega_x + x_3 \delta \omega_y \tag{13a}$$

$$\delta \varphi x_i = \delta \theta x_i - \delta \omega_x \quad (i=1,2,3,4) \tag{13b}$$

$$\delta \varphi y_i = \delta \theta y_i - \delta \omega_y \quad (i=1,2,3,4) \tag{13c}$$

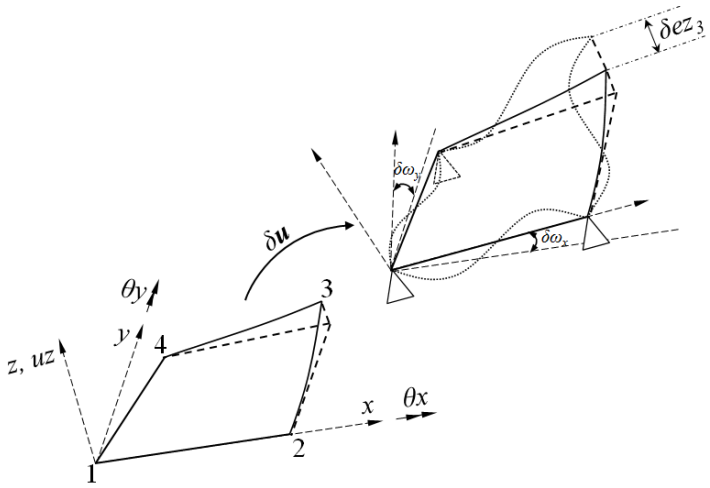

Figure 3. Deformations and Movements of Plate Element

As no out-of-plane restraint is assumed on the node 3 to allow for warping, there exists a vertical displacement at the node 3 given in Eq. (13a). The transformation matrix for the plate element from local to basic coordinate system can be expressed as follows,

$$\boldsymbol{L}_p = \frac{\partial \boldsymbol{e}_p}{\partial \boldsymbol{u}^T} \tag{14a}$$

$$\delta \boldsymbol{e}_p = \boldsymbol{L}_p \delta \boldsymbol{u} \tag{14b}$$

in which $\boldsymbol{L}_p$ is a 9×24 matrix as well as $\boldsymbol{L}_m$. Similar to the membrane element, the internal force vectors of the plate element in these two coordinate systems have the relationship as,

$$\boldsymbol{f} = \boldsymbol{L}_p^T \boldsymbol{p}_p \tag{15}$$

Combining the relationships of the membrane and plate elements together gives

$$\delta \boldsymbol{e} = \boldsymbol{L}\delta \boldsymbol{u} \tag{16a}$$

$$\boldsymbol{f} = \boldsymbol{L}^T \boldsymbol{p} \tag{16b}$$

$$\boldsymbol{L} = \begin{bmatrix} \boldsymbol{L}_m \\ \boldsymbol{L}_p \end{bmatrix} \tag{16c}$$

From the above, the relationships of the displacement vectors and the internal force vectors of the shell element between the local and basic coordinate systems have been presented. It is worth noting that the basic coordinate system corresponds to the warping shell element. However, in general, the membrane element and the plate element are derived based on the flat facet which is the projection of the warping shell element. Thus, the transformation between the projection and the warping shell element should be established. In this paper, the warping at the node 3 is regarded as an eccentricity, which can be treated as a rigid beam between the real node and the projected one. According to this assumption, the displacements of the membrane element have the equations as follows,

$$\delta ex_3^p = \delta ex_3 - z_3 \delta \varphi y_3 \tag{17a}$$

$$\delta ey_3^p = \delta ey_3 + z_3 \delta \varphi x_3 \tag{17b}$$

in which the superscript "p" refers to the projection of the warping shell element.

From Eqs. (16) and (17), the relationship between the projection and the local coordinate system can be written as follows,

$$\delta \boldsymbol{e}^p = \boldsymbol{E}\boldsymbol{L}\delta \boldsymbol{u} \tag{18a}$$

$$\boldsymbol{f} = \boldsymbol{L}^T \boldsymbol{E}^T \boldsymbol{p}^p \tag{18b}$$

$$\boldsymbol{E}_{i,i} = 1,\ i=1\sim 18;\quad \boldsymbol{E}_{2,16} = -z_3;\quad \boldsymbol{E}_{3,15} = z_3 \tag{18c}$$

where $\boldsymbol{E}$ represents the transformation matrix from the warping shell element to its projection. It should be pointed out the plate element is not affected by the warping effect. Thus, the pure deflection and rotations at the node 3 of the warping shell element are identical to those in its projection.

2.3 Linear Stiffness Matrix in Local Coordinate System

As shown in Figures 2 and 3, the stiffness matrix of the projection of the warping shell element without rigid body motions is a 18×18 non-singular matrix and can be expressed as,

$$\delta \boldsymbol{p}^p = \boldsymbol{k}_b^p \delta \boldsymbol{e}^p \tag{19}$$

where the subscript "p" means that the stiffness matrix $\boldsymbol{k}_b^p$ is the basic linear stiffness of the shell element on the projection plane. Because the pure deformational method is element-independent,

the shell linear stiffness matrix $\boldsymbol{k}_b^p$ can be formulated by any 4-node membrane element and plate element. Also, the material nonlinearity can be conveniently considered in $\boldsymbol{k}_b^p$ in the basic coordinate system.

From Eqs. (18) and (19), the stiffness matrix of the warping shell element in the local coordinate system can be derived as follows,

$$\begin{aligned}\delta \boldsymbol{f} &= \boldsymbol{L}^T \boldsymbol{E}^T \boldsymbol{k}_b^p \boldsymbol{E}\, \boldsymbol{L}\, \delta \boldsymbol{u} + \delta\left(\boldsymbol{L}^T \boldsymbol{E}^T\right) \boldsymbol{p}^p \\ &= \boldsymbol{k}_l\, \delta \boldsymbol{u} + \boldsymbol{k}_g\, \delta \boldsymbol{u}\end{aligned} \tag{20a}$$

$$\boldsymbol{k}_l = \boldsymbol{L}^T \boldsymbol{E}^T \boldsymbol{k}_b^p \boldsymbol{E}\, \boldsymbol{L} \tag{20b}$$

where $\boldsymbol{k}_l$ is the stiffness matrix of the warping shell element in the local coordinate system and is a 24×24 singular stiffness matrix in the local coordinate system. The local geometrical stiffness (initial stress) matrix $\boldsymbol{k}_g$ used in geometrically nonlinear analysis will be discussed in the next section.

To sum up, the 18×18 stiffness matrix $\boldsymbol{k}_b^p$ has a simpler expression and less dimensions compared with the 24×24 stiffness matrix $\boldsymbol{k}_l$, which saves the computer storage and improves the computational efficiency.

3. CO-ROTATIONAL ALGORITHM

In this section, a novel co-rotational algorithm for quadrilateral shell elements considering warping effect based on pure deformational method is proposed. Before the derivation of this algorithm, the relationship between the global and basic coordinate systems should be established. Through Eq. (18b), we have known the expression of the internal force vector in the local coordinate system, and therefore the one in the global coordinate system can be written as

$$\boldsymbol{F} = \boldsymbol{T}_8^T \boldsymbol{L}^T \boldsymbol{E}^T \boldsymbol{p}^p \tag{21a}$$

$$\boldsymbol{F} = \{\boldsymbol{F}_1^T, \boldsymbol{F}_2^T, \boldsymbol{F}_3^T, \boldsymbol{F}_4^T\}^T \tag{21b}$$

$$\boldsymbol{F}_i = \{FX_i, FY_i, FZ_i, MX_i, MY_i, MZ_i\}^T \tag{21c}$$

in which the matrix $\boldsymbol{T}_8$ is composed of eight matrices $\boldsymbol{T}$ given in Eq. (2) along diagonal.

Similarly, the corresponding displacement vector can be written as,

$$\boldsymbol{U} = \{\boldsymbol{U}_1^T, \boldsymbol{U}_2^T, \boldsymbol{U}_3^T, \boldsymbol{U}_4^T\}^T \tag{21d}$$

$$\boldsymbol{U}_i = \{UX_i, UY_i, UZ_i, \Theta X_i, \Theta Y_i, \Theta Z_i\} \tag{21e}$$

Thus, the relationships between these different systems by making use of the previous equations can be concluded in Figure 4 as follows,

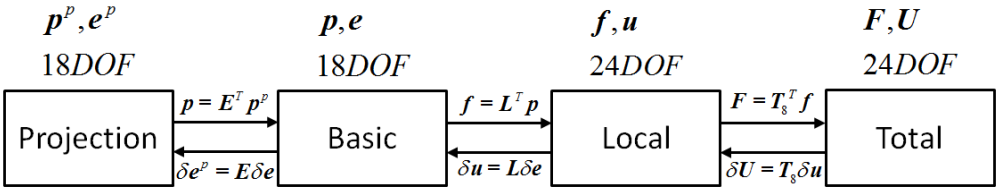

Figure 4. Relationships between Different Coordinate Systems

The conventional co-rotational algorithm needs to consider the non-additive property of 3D large rotations such as references (Nour-Omid and Rankin [6]; Felippa and Haugen [8]) and therefore an additional transformation matrix is required in Eq. (21a). However, this property can be omitted since the pure deformational rotations are small and can be regarded as vectorial parameters. In addition, it can be seen that the warping effect has been taken into account in Eq. (21a), which will contribute to a part of the geometrical stiffness matrix.

According to the derivation process of the EICR algorithm framework presented in references (Nour-Omid and Rankin [6]; Felippa and Haugen [8]) to obtain the tangent stiffness matrix, by taking variation of Eq. (21a), we have,

$$\delta \boldsymbol{F} = \boldsymbol{T}_8^T \boldsymbol{L}^T \boldsymbol{E}^T \delta \boldsymbol{p}^p + \delta \boldsymbol{T}_8^T \boldsymbol{L}^T \boldsymbol{E}^T \boldsymbol{p}^p + \boldsymbol{T}_8^T \delta \boldsymbol{L}^T \boldsymbol{E}^T \boldsymbol{p}^p + \boldsymbol{T}_8^T \boldsymbol{L}^T \delta \boldsymbol{E}^T \boldsymbol{p}^p \tag{22}$$

where the first term yields the linear stiffness matrix and the last three terms produce the geometrical stiffness matrix using the internal forces at current configuration.

Referring to the derivation process by authors (Nour-Omid and Rankin [6]; Felippa and Haugen [8]), it is strict to continuously take variations of these transformation matrices shown in Eq. (22) following standard mathematical flow. However, based on the pure deformational model, a novel and simpler derivation of the EICR algorithm can be proposed, in which the geometrical stiffness matrix is derived by the load perturbation of the linear equilibrium equations in its local coordinates system.

Moreover, Eq. (22) can be rewritten as follows,

$$\delta \boldsymbol{F} = \boldsymbol{T}_8^T \left(\boldsymbol{k}_l + \boldsymbol{k}_g^r + \boldsymbol{k}_g^m + \boldsymbol{k}_g^p + \boldsymbol{k}_g^w \right) \boldsymbol{T}_8 \delta \boldsymbol{U} \tag{23}$$

in which the subscript "*l*" means linear stiffness matrix and the subscript "*g*" means geometrical stiffness matrix; $\boldsymbol{k}_l$ is the linear stiffness matrix considering warping effect given in Eq. (20b) and corresponds to the first term in Eq. (22); $\boldsymbol{k}_g^r$ is due to the rigid body motions of the element and corresponds to the second term in Eq. (22); $\boldsymbol{k}_g^m$ and $\boldsymbol{k}_g^p$ are caused by the dimension changes of the membrane and plate elements respectively and reflect the third term in Eq. (22) together; $\boldsymbol{k}_g^w$ is due to the warping and corresponds to the last terms in Eq. (22). The details of each geometrical stiffness matrix will be introduced as follows.

3.1 Geometrical Stiffness due to Rigid Body Motions

On the basis of the local coordinate system, the variation of the internal force vector at node *i* due to a small rotation is given by Goldstein Goldstein [39] as

$$\delta \boldsymbol{f}_i^f = \delta\boldsymbol{\omega} \times \boldsymbol{f}_i^f = -\mathbf{Spin}(\boldsymbol{f}_i^f)\delta\boldsymbol{\omega} \tag{24a}$$

$$\delta \boldsymbol{f}_i^m = \delta\boldsymbol{\omega} \times \boldsymbol{f}_i^m = -\mathbf{Spin}(\boldsymbol{f}_i^m)\delta\boldsymbol{\omega} \tag{24b}$$

where $\boldsymbol{f}_i^f = \{fx_i, fy_i, fz_i\}^T$ and $\boldsymbol{f}_i^m = \{mx_i, my_i, mz_i\}^T$ are the translational internal force vector and rotational internal moment vector at the node *i* respectively; $\delta\boldsymbol{\omega} = \{\delta\omega_x, \delta\omega_y, \delta\omega_z\}^T$ is the variation of rigid body rotation vector shown in Eq. (9) defined in the local coordinate system. The operational symbol **Spin(·)** can transfer a three-dimensional vector into a skew-symmetric spin tensor, for example,

$$\mathbf{Spin}(\boldsymbol{f}_i^f) = \begin{bmatrix} 0 & -fz_i & fy_i \\ fz_i & 0 & -fx_i \\ -fy_i & fx_i & 0 \end{bmatrix} \tag{25}$$

Through Eqs. (5), (9) and (24), we have,

$$\delta \boldsymbol{f} = \boldsymbol{-A}\cdot\boldsymbol{G}\,\delta\boldsymbol{u} = \boldsymbol{k}_g^r \delta\boldsymbol{u} \tag{26a}$$

$$\boldsymbol{A} = \begin{bmatrix} \mathbf{Spin}(\boldsymbol{f}_1^f) \\ \mathbf{Spin}(\boldsymbol{f}_1^m) \\ \mathrm{M} \\ \mathbf{Spin}(\boldsymbol{f}_4^f) \\ \mathbf{Spin}(\boldsymbol{f}_4^m) \end{bmatrix} \tag{26b}$$

in which the matrix $\boldsymbol{G}$ is used to connect the variation of the rigid body rotation vector to the variation of the nodal displacement vector and can be expressed as follows,

$$\boldsymbol{G} = \frac{\partial\boldsymbol{\omega}}{\partial\boldsymbol{u}^T} = \begin{bmatrix} \frac{\partial\boldsymbol{\omega}}{\partial\boldsymbol{u}_1^T} & \frac{\partial\boldsymbol{\omega}}{\partial\boldsymbol{u}_2^T} & \frac{\partial\boldsymbol{\omega}}{\partial\boldsymbol{u}_3^T} & \frac{\partial\boldsymbol{\omega}}{\partial\boldsymbol{u}_4^T} \end{bmatrix} \tag{27}$$

Taking use of Eqs. (5a) and (9), the submatrices of $\boldsymbol{G}$ can be detailed as,

$$\frac{\partial\boldsymbol{\omega}}{\partial\boldsymbol{u}_1^T} = \begin{bmatrix} 0 & 0 & (x_4 - x_2)/x_2 y_4 & \\ 0 & 0 & 1/x_2 & \mathbf{0}_{3\times3} \\ 0 & -1/x_2 & 0 & \end{bmatrix} \tag{28a}$$

$$\frac{\partial\boldsymbol{\omega}}{\partial\boldsymbol{u}_2^T} = \begin{bmatrix} 0 & 0 & -x_4/x_2 y_4 & \\ 0 & 0 & -1/x_2 & \mathbf{0}_{3\times3} \\ 0 & 1/x_2 & 0 & \end{bmatrix} \tag{28b}$$

$$\frac{\partial\boldsymbol{\omega}}{\partial\boldsymbol{u}_3^T} = \mathbf{0}_{3\times6} \tag{28c}$$

$$\frac{\partial \boldsymbol{\omega}}{\partial \boldsymbol{u}_4^T} = \begin{bmatrix} 0 & 0 & 1/y_4 & \\ 0 & 0 & 0 & \mathbf{0}_{3\times 3} \\ 0 & 0 & 0 & \end{bmatrix} \tag{28d}$$

From the above, the geometrical stiffness matrix of the warping shell element due to rigid body rotations in the local coordinate system, $\boldsymbol{k}_g^r$, has been presented. Note that the internal forces used in Eq. (26b) belong to the warping shell element at current configuration.

3.2 Geometrical Stiffness due to Dimension Changes

As the flat quadrilateral shell element consists of a membrane part and a plate part, the corresponding geometrical stiffness matrices will be discussed separately. First, the geometrical stiffness due to the dimension changes of a membrane element will be detailed.

Based on the pure deformational membrane element model with three degrees of freedom restrained (as shown in Figure 5), the internal forces at the free degrees of freedom can be regarded as action forces which will be kept unchanged after deformation. In the meantime, the internal forces at the constraints can be regarded as the reaction forces and will vary after deformation to keep the self-equilibrium of the element. Thus, the gradients of the reaction forces due to the deformation can be used to deduce the geometrical stiffness of the membrane part directly.

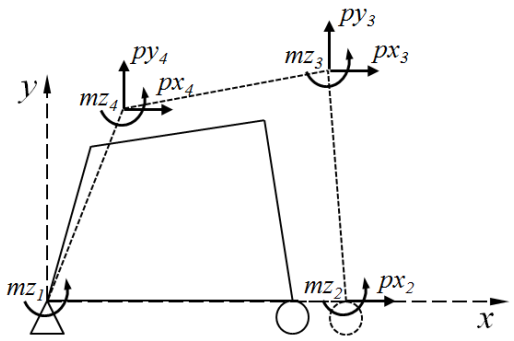

Figure 5. Pure Deformational Membrane Element

Based on the initial configuration of the membrane element, the equilibrium equations can be written as,

$$\sum fx = 0: \; fx_1 + px_2 + px_3 + px_4 = 0 \tag{29a}$$

$$\sum fy = 0: \; fy_1 + fy_2 + py_3 + py_4 = 0 \tag{29b}$$

$$\sum mz = 0 \, at \, the \, node 1: \quad fy_2 x_2 - px_3 y_3 + py_3 x_3 - px_4 y_4 + py_4 x_4 + \sum_{i=1}^{4} nz_i = 0 \tag{29c}$$

After deformation, the action forces shown in Figure 5 keep identical, while the three reaction forces fx_1, fy_1 and fy_2 change to $fx_1^{'}$, $fy_1^{'}$ and $fy_2^{'}$ respectively. Then, the equilibrium equations become

$$\sum fx = 0: \; fx_1' + px_2 + px_3 + px_4 = 0 \tag{30a}$$

$$\sum fy = 0: \; fy_1' + fy_2' + py_3 + py_4 = 0 \tag{30b}$$

$$\sum mz = 0 \; at \; the \; node 1: \\ fy_2^{'}x_2^{'} - px_3y_3^{'} + py_3x_3^{'} - px_4y_4^{'} + py_4x_4^{'} + \sum_{i=1}^{4} nz_i = 0 \tag{30c}$$

in which $x_i^{'} = x_i + \delta ex_i, i = 2,3,4$; $y_i^{'} = y_i + \delta ey_i, i = 3,4$; $fx_1^{'} = fx_1 + \delta fx_1$, $fy_1^{'} = fy_1 + \delta fy_1$ and $fy_2^{'} = fy_2 + \delta fy_2$.

Substituting Eq. (29) into Eq. (30) and omitting the high order variations, the variations of the reaction forces yield,

$$\delta fx_1 = 0 \tag{31a}$$

$$\delta fy_1 = \frac{1}{x_2}(px_3\delta ey_3 - py_3\delta ex_3 + px_4\delta ey_4 - py_4\delta ex_4 - fy_2\delta ex_2) \tag{31b}$$

$$\delta fy_2 = -\delta fy_1 \tag{31c}$$

Eq. (31) can also be further rewritten as follows,

$$\begin{Bmatrix} \delta fy_1 \\ \delta fy_2 \end{Bmatrix} = \frac{1}{x_2}\begin{bmatrix} fy_2 & py_3 & px_3 & py_4 & -px_4 \\ -fy_2 & -py_3 & -px_3 & -py_4 & px_4 \end{bmatrix} \mathbf{0}_{2\times 4} \delta \boldsymbol{e}_m \\ = \frac{1}{x_2}\begin{bmatrix} fy_2 & py_3 & px_3 & py_4 & -px_4 \\ -fy_2 & -py_3 & -px_3 & -py_4 & px_4 \end{bmatrix} \mathbf{0}_{2\times 4} \boldsymbol{L}_m \delta \boldsymbol{u}_m \\ = \boldsymbol{k}_g^{\%} \delta \boldsymbol{u}_m \tag{32}$$

in which $\boldsymbol{k}_g^{\%}$ is the 2×12 matrix in the basic coordinate system due to the dimension changes of the membrane element. This matrix needs to be simply expanded to the 24×24 geometrical stiffness matrix $\boldsymbol{k}_g^m$ shown in Eq. (23). Also, it should be noted that the warping effect does not influence the equilibrium of the pure deformational membrane element.

Following the same way by finding the variations of the reaction forces, the geometrical stiffness due to the dimension changes of the plate element can be obtained. However, the warping effect should be considered in the plate element. As shown in Figure 6, the nodal vertical displacements are constrained except node 3. The reaction forces are the shear forces $\{fz_1, fz_2, fz_4\}^T$ at the three restrained nodes. To consider the warping at the node 3, the in-plane translational forces must be

taken into account. Unlike the other nodes, the shear force at the node 3 will be kept unchanged after deformation.

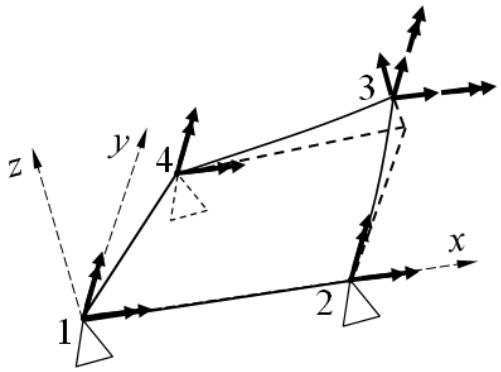

Figure 6. Pure Deformational Plate Element

For the pure deformational plate element at the initial configuration shown in Figure 6, the equilibrium equations can be established as

$$\sum fz = 0:\ fz_1 + fz_2 + fz_4 + pz_3 = 0 \tag{33a}$$

$$\sum mx = 0:\ pz_3 y_3 - py_3 z_3 + fz_4 y_4 + \sum_{i=1}^{4} nx_i = 0 \tag{33b}$$

$$\sum my = 0: - pz_3 x_3 + px_3 z_3 - fz_2 x_2 - fz_4 x_4 + \sum_{i=1}^{4} ny_i = 0 \tag{33c}$$

After deformation, the equilibrium equations become

$$\sum fz = 0:\ fz_1' + fz_2' + fz_4' + pz_3 = 0 \tag{34a}$$

$$\sum mx = 0:\ pz_3 y_3' - py_3 z_3' + fz_4' y_4' + \sum_{i=1}^{4} nx_i = 0 \tag{34b}$$

$$\sum my = 0:\ - pz_3 x_3' + px_3 z_3' - fz_2' x_2' - fz_4' x_4' + \sum_{i=1}^{4} ny_i = 0 \tag{34c}$$

in which $x_i' = x_i + \delta ex_i, i = 2,3,4$; $y_i' = y_i + \delta ey_i, i = 3,4$; $z_3' = z_3 + \delta ez_3$; $fz_i' = fz_i + \delta fz_i$, i=1,2,4.

Considering Eqs. (33) and (34) and omitting the high order variations, we have,

$$\delta fz_4 = \frac{1}{y_4}\left(py_3 \delta ez_3 - pz_3 \delta ey_3 - fz_4 \delta ey_4\right) \tag{35a}$$

$$\delta fz_2 = \frac{1}{x_2}(-fz_2 \delta ex_3 - fz_4 \delta ex_4 - pz_3 \delta ex_3 + px \delta ez_3 - \delta fz_4 x_4) \tag{35b}$$

$$\delta fz_3 = -\delta fz_2 - \delta fz_4 \tag{35c}$$

Then, it can be rewritten as follows,

$$\begin{Bmatrix} \delta fz_1 \\ \delta fz_2 \\ \delta fz_3 \end{Bmatrix} = \begin{bmatrix} \frac{fz_2}{x_2} & \frac{pz_3}{x_2} & \frac{pz_3(x_2-x_4)}{x_2y_4} & \frac{fz_4}{x_2} & \frac{fz_4(x_2-x_4)}{x_2y_4} & \frac{py_3(-x_2+x_4)-px_3y_4}{x_2y_4} \\ -\frac{fz_2}{x_2} & -\frac{pz_3}{x_2} & \frac{pz_3x_4}{x_2y_4} & -\frac{fz_4}{x_2} & \frac{fz_4x_4}{x_2y_4} & \frac{px_3y_4-py_3x_4}{x_2y_4} \\ 0 & 0 & -\frac{pz_3}{y_4} & 0 & -\frac{fz_4}{y_4} & \frac{py_3}{y_4} \end{bmatrix} \begin{Bmatrix} \delta ex_2 \\ \delta ex_3 \\ \delta ey_3 \\ \delta ex_4 \\ \delta ey_4 \\ \delta ez_3 \end{Bmatrix} = \mathbf{k}_g^{p\prime} \delta \mathbf{u} \tag{36}$$

where $\mathbf{k}_g^{p\prime}$ is the 3×12 geometrical stiffness matrix in the basic coordinate system due to the dimension changes of the plate element and needs to be expanded to the 24×24 geometrical stiffness matrix $\mathbf{k}_g^p$ shown in Eq. (23).

3.3 Geometrical Stiffness due to Warping Effect

The moments on the node allowing for warping varies with the change of eccentricity (ez_3) and therefore the load perturbation will deduce a part of geometrical stiffness. The virtual displacements and rotations at the node 3 of the warping shell element and its projection have the relationship given in Eq. (17). Thus, the corresponding forces and moments in these two different points have the relationship as,

$$nx_3 = z_3\, py_3 + nx_3^p \tag{37a}$$

$$ny_3 = -z_3\, px_3 + ny_3^p \tag{37b}$$

Similar to the previous derivations, the forces and moments at the free DOF of the projection can be regarded as the action forces and moments and keep unchanged after deformation. However, the moments at the warping node 3 vary after deformation and their variations can be expressed as,

$$\delta nx_3 = \delta ez_3\, py_3 \tag{38a}$$

$$\delta ny_3 = -\delta ez_3\, px_3 \tag{38b}$$

Thus, the variation of the internal force vector of the shell element due to warping phenomenon based on the basic coordinate system can be rewritten through Eq. (38) as,

$$\delta \mathbf{p} = \mathbf{k}_g^{p\prime} \delta \mathbf{e} \tag{39a}$$

in which the $\mathbf{k}_g^{p\prime}$ is a 18×18 matrix and the non-zero entries $\mathbf{k}_g^{p\prime}(15,10) = py_3$, $\mathbf{k}_g^{p\prime}(16,10) = px_3$. Then, transferring it into the local coordinate system, we have,

$$\delta \mathbf{f} = \mathbf{L}^T \mathbf{k}_g^{p\prime} \mathbf{L}\, \delta \mathbf{u} \tag{39b}$$

$$\boldsymbol{k}_g^w = \boldsymbol{L}^T \boldsymbol{k}_g^0 \boldsymbol{L} \tag{39c}$$

For now, each part of the tangential stiffness matrix shown in Eq. (23) has been obtained.

3.4 Determination of Internal Forces

The key issue in the determination of internal forces of the shell element is how to extract the pure deformations from the total deformations. After that, the internal forces $\boldsymbol{p}^p$ at the projection can be computed using the linear stiffness matrix of the shell element and further transferred to the global coordinate system through Eq. (21).

For the iteration step j, the incremental nodal displacements and rotations of the shell element in the global coordinate system can be given by,

$$\Delta \boldsymbol{U} = \{\Delta \boldsymbol{U}_1^T, \Delta \boldsymbol{U}_2^T, \Delta \boldsymbol{U}_3^T, \Delta \boldsymbol{U}_4^T\}^T \tag{40a}$$

$$\Delta \boldsymbol{U}_i = \{\Delta UX_i, \Delta UY_i, \Delta UZ_i, \Delta \Theta X_i, \Delta \Theta Y_i, \Delta \Theta Z_i\}^T \tag{40b}$$

The information of the examined shell element at the last iteration step j-1 are denoted as: the global and local coordinates ${}^{j-1}\boldsymbol{X}_i$, ${}^{j-1}\boldsymbol{x}_i$, (i=1,2,3,4); the local to global transformation matrix ${}^{j-1}\boldsymbol{T}$; and the internal forces ${}^{j-1}\boldsymbol{p}^p$ at the projection for pure deformational element. Thus, the next procedure is how to update these data with the known incremental global displacements and rotations shown in Eqs. (40).

The global coordinates of the shell element at the iteration step j can be updated as,

$${}^{j}\boldsymbol{X}_i = {}^{j-1}\boldsymbol{X}_i + \{\Delta UX_i, \Delta UY_i, \Delta UZ_i\}^T \tag{41}$$

Then, the local to global coordinate transformation matrix ${}^{j}\boldsymbol{T}$ and the local coordinates ${}^{j}\boldsymbol{x}_i$ of the shell element can be computed through Eqs. (2) and (3) respectively. In addition, the incremental translations of the pure deformational shell element considering warping effect can be obtained by using the local coordinates ${}^{j-1}\boldsymbol{x}_i$ and ${}^{j}\boldsymbol{x}_i$ as,

$$\Delta ex_2 = {}^{j}x_2 - {}^{j-1}x_2 \tag{42a}$$

$$\Delta ex_3 = {}^{j}x_3 - {}^{j-1}x_3, \quad \Delta ey_3 = {}^{j}y_3 - {}^{j-1}y_3, \quad \Delta ez_3 = {}^{j}z_3 - {}^{j-1}z_3 \tag{42b, c, d}$$

$$\Delta ex_4 = {}^{j}x_4 - {}^{j-1}x_4, \quad \Delta ey_4 = {}^{j}y_4 - {}^{j-1}y_4 \tag{42e, f}$$

To extract the incremental pure rotations of the shell element from the incremental global rotations with considering the non-vectorial properties of 3D large rotations, the Rodrigues-Cayley rotation tensor is adopted here, which is defined with a rotation angle θ about an unit pseudo-vector $\boldsymbol{n} = \{n_1, n_2, n_3\}^T$. The rotation matrix can be written as,

$$\boldsymbol{R}(\boldsymbol{n},\theta) = \boldsymbol{I}_3 + \boldsymbol{N}\sin\theta + \boldsymbol{N}^2(1-\cos\theta) \tag{43a}$$

$$\boldsymbol{N} = \mathbf{Spin}(\boldsymbol{n}) = \begin{bmatrix} 0 & -n_3 & n_2 \\ n_3 & 0 & -n_1 \\ -n_2 & n_1 & 0 \end{bmatrix} \tag{43b}$$

where $\theta = \sqrt{\theta_x^{\,2} + \theta_y^{\,2} + \theta_z^{\,2}}$, and the rotation vector corresponding to the rotation tensor is

$$\boldsymbol{\theta} = \theta\mathbf{n} = \begin{Bmatrix} \theta x \\ \theta y \\ \theta z \end{Bmatrix} \tag{43c}$$

Through Eq. (43), the incremental rotations $\Delta\boldsymbol{\Theta}_i = \{\Delta\Theta x_i, \Delta\Theta y_i, \Delta\Theta z_i\}^T$ at the node *i* in the global coordinate system can be expressed with the Rodrigues-Cayley rotation tensor as,

$$\Delta\boldsymbol{R}_i = \boldsymbol{R}(\boldsymbol{n}_i, \Delta\boldsymbol{\Theta}_i) \quad (i=1,2,3,) \tag{44a}$$

in which

$$\boldsymbol{n} = \{\Delta\Theta x_i / \Delta\Theta_i, \Delta\Theta y_i / \Delta\Theta_i, \Delta\Theta z_i / \Delta\Theta_i\}^T \tag{44b}$$

$$\Delta\Theta_i = \sqrt{\Delta\Theta x_i^{\,2} + \Delta\Theta y_i^{\,2} + \Delta\Theta z_i^{\,2}} \tag{44c}$$

To remove rigid body rotations of the element, the incremental rotation matrix at the node *i* for the pure deformational state can be given by

$$\Delta\boldsymbol{r}_i = {}^{j-1}\boldsymbol{T}\,\Delta\boldsymbol{R}_i\,{}^{j}\boldsymbol{T}^T \tag{45}$$

Then, the pertaining incremental rotations of the rotation matrix given in Eq. (45) can be deduced by the equation in the following,

$$\Delta\boldsymbol{\theta}(\Delta\boldsymbol{r}_i) = \begin{Bmatrix} \Delta\theta x_i \\ \Delta\theta y_i \\ \Delta\theta z_i \end{Bmatrix} = \frac{\Delta\theta}{2\sin\Delta\theta}\begin{Bmatrix} \Delta r_i^{32} - \Delta r_i^{23} \\ \Delta r_i^{13} - \Delta r_i^{31} \\ \Delta r_i^{21} - \Delta r_i^{12} \end{Bmatrix} = \frac{\arcsin\Delta\tau}{2\Delta\tau}\begin{Bmatrix} \Delta r_i^{32} - \Delta r_i^{23} \\ \Delta r_i^{13} - \Delta r_i^{31} \\ \Delta r_i^{21} - \Delta r_i^{12} \end{Bmatrix} \tag{46a}$$

in which, $\Delta\tau = \sqrt{(\Delta r_i^{32} - \Delta r_i^{23})^2 + (\Delta r_i^{13} - \Delta r_i^{31})^2 + (\Delta r_i^{21} - \Delta r_i^{12})^2}$ and Δr_i^{pq} (p, q=1,2,3) is the entry of rotation matrix $\Delta\boldsymbol{r}_i$.

Note that the range of $\Delta\theta$ in Eq. (46a) is [0, 90] and the numerical instability would occur when $\Delta\theta$ is closed to zero. Thus, the Taylor series of Eq. (50a) is adopted when θ is close to 0. For $\Delta\theta \le 0.05$, the coefficient in Eq. (46a) becomes

$$\frac{\Delta\theta}{2\sin\Delta\theta} \approx \frac{1}{2} + \frac{1}{12}\Delta\theta^2 + \frac{7}{720}\Delta\theta^4 \tag{46b}$$

Thus, by taking advantage of Eq. (46), we can get the pure deformational rotations of the warping shell element in the local coordinate system. As the rotations in the basic coordinate system are identical to those in the local coordinate system, we have,

$$\Delta\varphi x_i = \Delta\theta x_i, \quad \Delta\varphi y_i = \Delta\theta y_i, \quad \Delta\varphi z_i = \Delta\theta z_i \quad (i=1,2,3) \tag{47a, b, c}$$

From the above, the 18 entries of the incremental displacement vector $\Delta\boldsymbol{e}$ in the basic coordinate system can be obtained and then transferred to the projection through Eq. (17) as,

$$\Delta\boldsymbol{e}^p = {}^j\boldsymbol{E}\Delta\boldsymbol{e} \tag{48}$$

where the matrix ${}^j\boldsymbol{E}$ is calculated by using the local coordinates at current configuration.

Further, the incremental internal force vector of the projection can be determined through Eq. (19) as,

$$\Delta\boldsymbol{p}^p = {}^0\boldsymbol{k}_b^p\Delta\boldsymbol{e}^p \tag{49}$$

in which ${}^0\boldsymbol{k}_b^p$ is the initial stiffness matrix of the shell element at the projection calculated on the basis of initial configuration and used all the time. Thus, this matrix can be stored at the beginning of geometrically nonlinear analysis for all elastic problems. It is clear that this 18×18 stiffness matrix based on the pure deformation element model needs only 57% storage of the conventional 24×24 stiffness matrix.

Then, the internal force vector of the projection at the iteration step *j* can be updated by,

$${}^j\boldsymbol{p}^p = {}^{j-1}\boldsymbol{p}^p + \Delta\boldsymbol{p}^p \tag{50}$$

Finally, the internal force vector of the warping shell element in the global coordinate system at the current time can be obtained through Eq. (21). It should be noted that the procedures mentioned above imply that the pure deformational rotations are vectorial and additive according to the assumption of small rotations satisfy the classical plate theory.

4. NUMERICAL EXAMPLES

In this section, several benchmark examples are presented to illustrate the accuracy and robustness of the proposed EICR formulation based on the pure deformation method. In this study, a quadrilateral shell element formed by the membrane element with drilling rotations proposed by Ibrahimbegovic *et al.* [40] and the DKQ plate element proposed by Batoz and Tahar [41] is adopted for demonstration. The shell element was also extended into the geometrically nonlinear analysis by authors (Tang *et al.* [32]; Tang *et al.* [42]) and obtained success. In fact, any membrane and plate element can be employed in the proposed co-rotational framework. For example, to account for transverse shear deformation, the RDKQM plate element proposed by Chen and Cheung [43] can be used instead of the DKQ element.

In all examples, the 8-point two-dimensional integration is adopted. The convergent criterion is taken the norm of unbalanced forces not greater than 0.1% of the norm of the applied load.

4.1 Cantilever Plate Subjected to End Moment

A cantilever plate subjected to a concentrated end moment M at its tip is shown in Figure 7. It is a classical problem for examination of the performance of an element undergoing large rotations. In this example, there is no membrane stress and the cantilever beam will roll up into a complete circle when $M = 2\pi EI / L$. The input data are given in Figure 7.

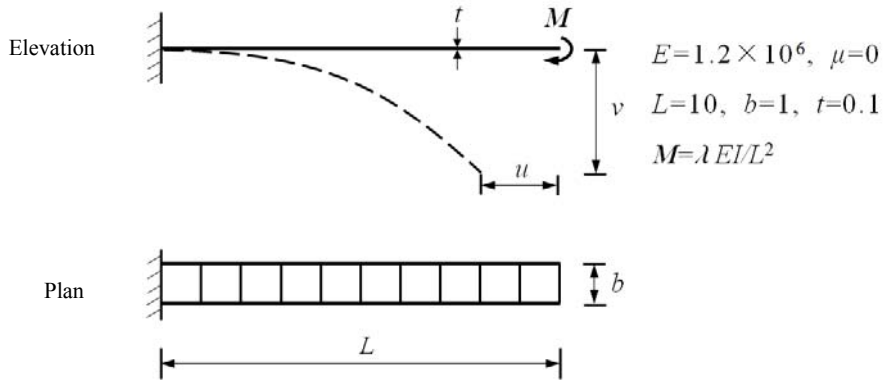

Figure 7. Cantilever Plate Subjected to End Moment

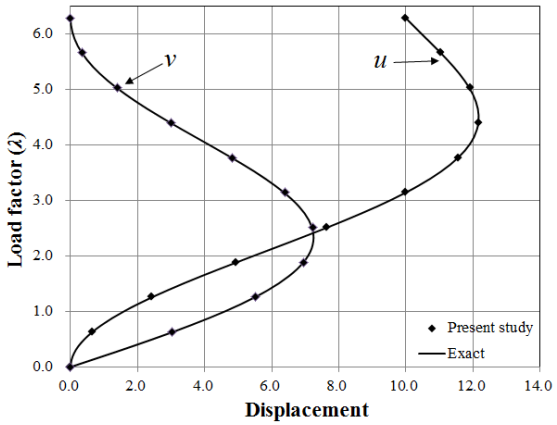

Figure 8. Load-displacement Curves of Cantilever Plate Subjected to An End Moment

The cantilever plate is divided into 10 quadrilateral flat shell elements. The load-displacement curves at the free end are plotted in Figure 8 which shows that these points have a very good agreement with the exact solutions.

4.2 Cantilever Beam Subjected to Shear Forces

A cantilever beam is subjected to two equal point loads at the free ends as shown in Figure 9. This example aims to verify the capability of the proposed co-rotational algorithm undergoing large deflections. The configuration and the material of the structure are the same as the first example except for the applied loading and Poisson's ratio μ.

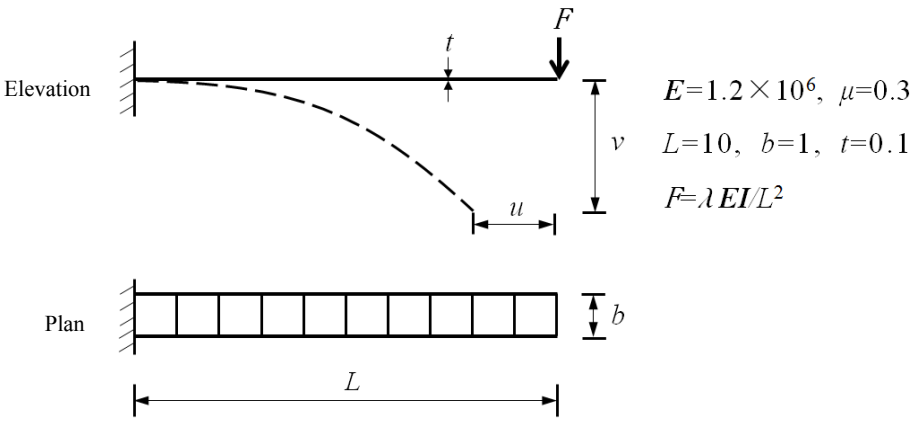

Figure 9. Cantilever Plate Subjected to Shear Forces

The predicted load-displacement curves are plotted against the results using 10 beam-column elements proposed by Tang *et al.* [36] in Figure 10. It can be seen that the results from the present study agree well with those by Tang *et al.* [36].

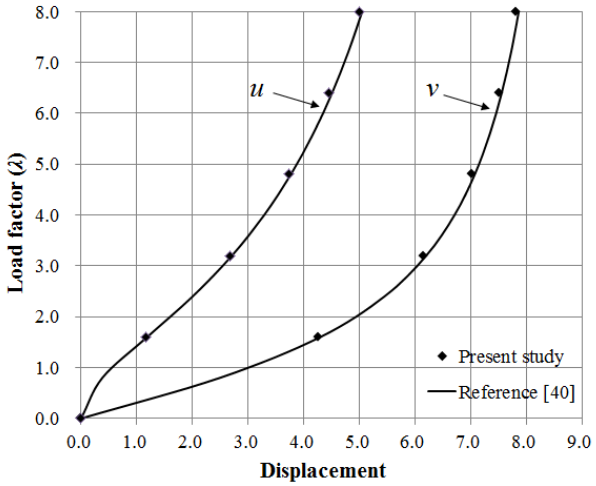

Figure 10. Load-displacement Curves of Cantilever Plate Subjected to Shear Forces

4.3 Pinched Hemispherical Shell with A Hole

The studied example is a hemispherical shell with an 18˚ hole at the top, as seen in Figure 11. This shell structure is subjected to two inward and two outward forces at the quarter points of its open edge. In this example, severely warping effect occurs for quadrilateral flat shell elements. Due to the symmetry of this problem, only a quarter of the hemisphere uses a 16×16 mesh of the proposed shell element.

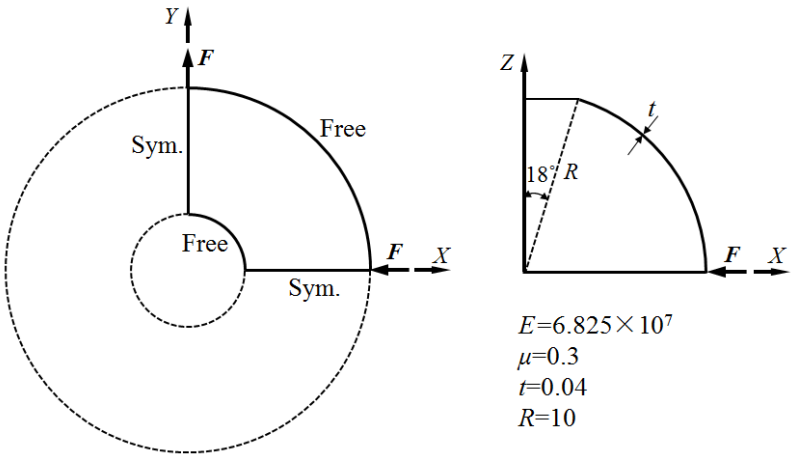

Figure 11. Pinched Hemispherical Shell with A Hole

The load-displacement curves at the quarter points obtained by the flat quadrilateral shell element based on the novel EICR formulation are plotted in Figure 12, while the results from the models by 16×16 Shell 181 elements in ANSYS and 12×12 MITC3+ (Jeon *et al.* [44]) elements are also provided for comparison. In general, the present study has the same trends as the others. The proposed method is slightly stiffer than the Shell 181 but softer than the MITC3+ element.

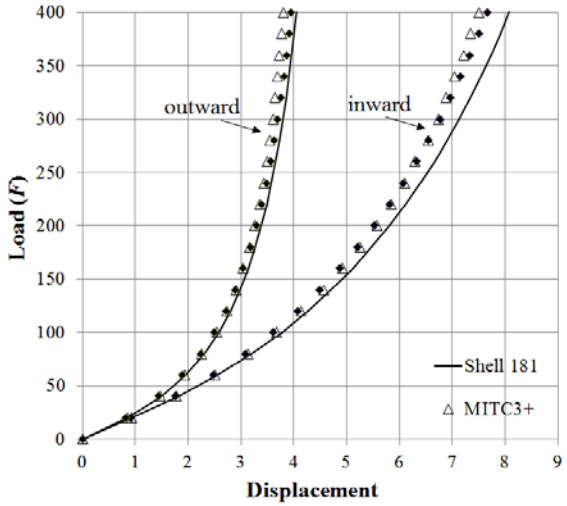

Figure 12. Load-displacement Curves of Pinched Hemispherical Shell

4.4 Cylindrical Shell Segment

A shallow cylinder shell is pinned along its longitudinal edges and free at its curved edges, with a concentrated load at its centre as shown in Figure 12. It is a well-known problem used to check the ability of an element against instability behaviour. Its equilibrium path exhibits a snap-through response with two limit points. Following the previous studies, two different thicknesses of 6.35 and 12.7 are considered respectively in this example. The detailed dimensions and material properties are shown in Figure 12. Due to symmetric nature, only a quarter of the structure is meshed with 4×4 shell elements. In addition, the arc-length method is adopted to trace the full equilibrium path of this problem.

The predicted results are plotted in Figure 13 against those of the shell 181 element in ANSYS and Surana [45]. It can be seen that the proposed algorithm shows a good agreement with the other elements.

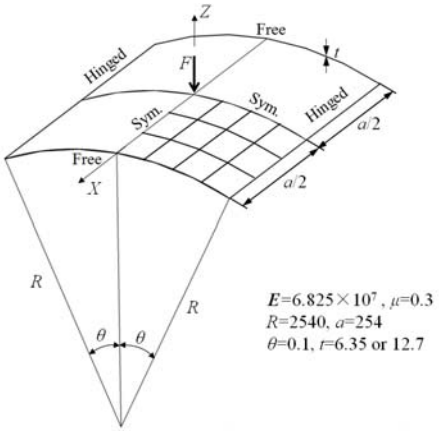

Figure 13. Cylindrical Shell Segment

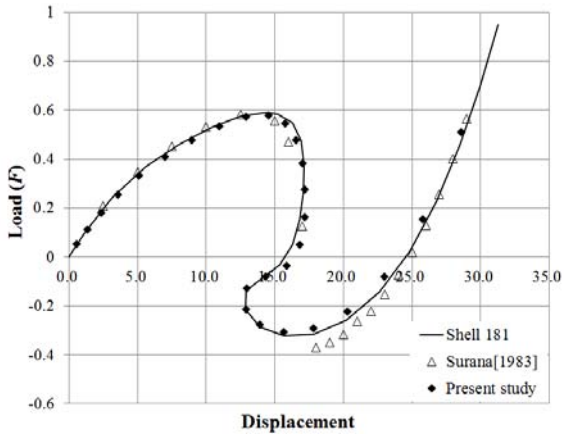

(a) t=6.35

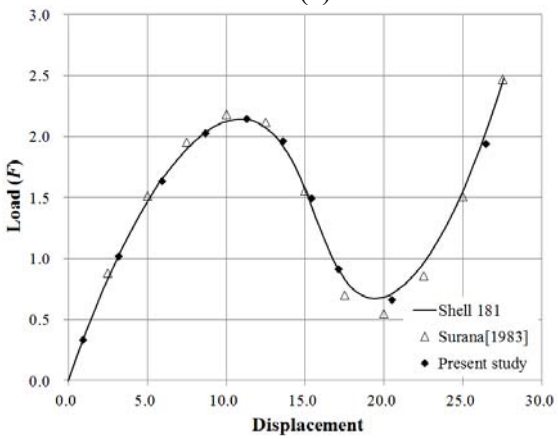

(b) t=12.7

Figure 14. Load-displacement Curves of Pinched Hemispherical Shell

5. CONCLUSION

In this paper, a novel co-rotational algorithm for quadrilateral shell element allowing for warping phenomenon based on pure deformational method is proposed for geometrically nonlinear analysis. This new co-rotational framework is essentially an element-independent algorithm which can be applied to any type of quadrilateral shell element constructed by different displacement interpolations. As the quantities of shell element are reduced by the pure deformational method, it leads to less computer storage and enhances the computational efficiency. Also, the co-rotational framework can consider the warping effect and therefore has a good convergence rate when warping occurs. The numerical examples presented in this paper demonstrate that the proposed method is accurate and robust. From this study, many previous works related to linear 4-node quadrilateral shell element can be conveniently extended to geometrically nonlinear analysis based on the proposed co-rotational framework.

ACKNOWLEDGEMENT

The authors are grateful to the financial supports by the Research Grant Council of the Hong Kong SAR Government on the projects “Second-Order Analysis of Flexible Steel Cable Nets Supporting Debris (PolyU 152008/15E)” and “Second-order and Advanced Analysis of Arches and Curved Structures (PolyU 152012/14E)”, the Hong Kong Branch of Chinese National Engineering Research Centre for Steel Construction supported by The Innovation and Technology Fund of the Hong Kong SAR Government for the project “Advanced Numerical Analyses for Building Structures Using High Performance Steel Materials” and by the Innovative Technology Fund for the project “Advanced design of flexible barrier systems by large deflection theory (ITS/032/14)”.

REFERENCES

[1] Wempner, G., "Finite Elements, Finite Rotations and Small Strains of Flexible Shells", International Journal of Solids and Structures, 1969, Vol. 5, No. 2, pp. 117-153.

[2] Belytschko, T. and Hsieh, B., "Non-linear Transient Finite Element Analysis with Convected Co-ordinates", International Journal for Numerical Methods in Engineering, 1973, Vol. 7, No. 3, pp. 255-271.

[3] Belytschko, T., Schwer, L. and Klein, M., "Large Displacement, Transient Analysis of Space Frames", International Journal for Numerical Methods in Engineering, 1977, Vol. 11, No. 1, pp. 65-84.

[4] Rankin, C. C. and Brogan, F. A., "An Element Independent Corotational Procedure for the Treatment of Large Rotations", Journal of pressure vessel technology, 1986, Vol. 108, No. pp. 165-174.

[5] Rankin, C. and Nour-Omid, B., "The Use of Projectors to Improve Finite Element Performance", Computers & Structures, 1988, Vol. 30, No. 1, pp. 257-267.

[6] Nour-Omid, B. and Rankin, C., "Finite Rotation Analysis and Consistent Linearization Using Projectors", Computer Methods in Applied Mechanics and Engineering, 1991, Vol. 93, No. 3, pp. 353-384.

[7] Crisfield, M., "Advanced Topics, Volume 2, Non-Linear Finite Element Analysis of Solids and Structures", Wiley, 1997.

[8] Felippa, C. and Haugen, B., "A Unified Formulation of Small-strain Corotational Finite Elements: I. Theory", Computer Methods in Applied Mechanics and Engineering, 2005, Vol. 194, No. 21, pp. 2285-2335.

[9] Pacoste, C., "Co-rotational Flat Facet Triangular Elements for Shell Instability Analyses", Computer Methods in Applied Mechanics and Engineering, 1998, Vol. 156, No. 1, pp. 75-110.
[10] Skallerud, B. and Haugen, B., "Collapse of Thin Shell Structures-stress Resultant Plasticity Modelling within a Co-rotated ANDES Finite Element Formulation", International Journal for Numerical Methods in Engineering, 1999, Vol. 46, No. 12, pp. 1961-1986.
[11] Eriksson, A. and Pacoste, C., "Element Formulation and Numerical Techniques for Stability Problems in Shells", Computer Methods in Applied Mechanics and Engineering, 2002, Vol. 191, No. 35, pp. 3775-3810.
[12] Battini, J. M. and Pacoste, C., "On the Choice of Local Element Frame for Corotational Triangular Shell Elements", Communications in Numerical Methods in Engineering, 2004, Vol. 20, No. 10, pp. 819-825.
[13] Battini, J. M. and Pacoste, C., "On the Choice of the Linear Element for Corotational Triangular Shells", Computer Methods in Applied Mechanics and Engineering, 2006, Vol. 195, No. 44, pp. 6362-6377.
[14] Levy, R. and Gal, E., "Geometrically Nonlinear Three-noded Flat Triangular Shell Elements", Computers & Structures, 2001, Vol. 79, No. 26, pp. 2349-2355.
[15] Gal, E. and Levy, R., "Geometrically Nonlinear Analysis of Shell Structures using a Flat Triangular Shell Finite Element", Archives of Computational Methods in Engineering, 2006, Vol. 13, No. 3, pp. 331-388.
[16] Levy, R. and Spillers, W. R. “Analysis of Geometrically Nonlinear Structures”, Springer Science & Business Media, 2013.
[17] Crisfield, M. and Moita, G., "A Unified Co-rotational Framework for Solids, Shells and Beams", International Journal of Solids and Structures, 1996, Vol. 33, No. 20, pp. 2969-2992.
[18] Crisfield, M., Moita, G., Lyons, L. and Jelenić, G., "Enhanced Lower-order Element Formulations for Large Strains", Computational mechanics, 1995, Vol. 17, No. 1-2, pp. 62-73.
[19] Izzuddin, B., "An Enhanced Co-rotational Approach for Large Displacement Analysis of Plates", International Journal for Numerical Methods in Engineering, 2005, Vol. 64, No. 10, pp. 1350-1374.
[20] Li, Z. and Vu-Quoc, L., "An Efficient Co-rotational Formulation for Curved Triangular Shell Element", International Journal for Numerical Methods in Engineering, 2007, Vol. 72, No. 9, pp. 1029-1062.
[21] Li, Z., Izzuddin, B. and Vu-Quoc, L., "A 9-node Co-rotational Quadrilateral Shell Element", Computational Mechanics, 2008, Vol. 42, No. 6, pp. 873-884.
[22] Li, Z., Liu, Y., Izzuddin, B. and Vu-Quoc, L., "A Stabilized Co-rotational Curved Quadrilateral Composite Shell Element", International Journal for Numerical Methods in Engineering, 2011, Vol. 86, No. 8, pp. 975-999.
[23] Li, Z., Zhuo, X., Vu-Quoc, L., Izzuddin, B. and Wei, H., "A Four-node Corotational Quadrilateral Elastoplastic Shell Element using Vectorial Rotational Variables", International Journal for Numerical Methods in Engineering, 2013, Vol. 95, No. 3, pp. 181-211.
[24] Li, Z., Zheng, T., Vu-Quoc, L. and Izzuddin, B., "A 4-node Co-rotational Quadrilateral Composite Shell Element", International Journal of Structural Stability and Dynamics, 2016, Vol. 16, No. 9, Vol. 1550053.
[25] Izzuddin, B. and Liang, Y., "Bisector and Zero-macrospin Co-rotational Systems for Shell Elements", International Journal for Numerical Methods in Engineering, 2016, Vol. 105, No. 4, pp. 286-320.
[26] Li, Z., Izzuddin, B., Vu-Quoc, L., Rong Z. and Zhuo X.. "A 3-node Co-rotational Triangular Elasto-plastic Shell Element using Vectorial Rotational Variables." Advanced Steel Construction, 2017, Vol. 13, No. 3, pp. 206-240.
[27] Bathe, K. J. “Finite Element Procedures”, Klaus-Jurgen Bathe, 2006.

[28] Bathe, K. J. and Ho, L. W., "A Simple and Effective Element for Analysis of General Shell Structures", Computers & Structures, 1981, Vol. 13, No. 5-6, pp. 673-681.
[29] Kuo, M, H., "Nonlinear Analysis of General Shell Structures by Flat Triangular Shell Element", Computers & structures, 1987, Vol. 25, No. 5, pp. 665-675.
[30] Jiang, L., Chernuka, M. W. and Pegg, N. G., "A Co-rotational, Updated Lagrangian Formulation for Geometrically Nonlinear Finite Element Analysis of Shell Structures", Finite Elements in Analysis and design, 1994, Vol. 18, No. 1-3, pp. 129-140.
[31] Hsiao, K. M., "Nonlinear Analysis of General Shell Structures by Flat Triangular Shell Element", Computers & structures, 1987, Vol. 25, No. 5, pp. 665-675.
[32] Tang, Y. Q., Zhou, Z. H. and Chan, S. L., "Geometrically Nonlinear Analysis of Shells by Quadrilateral Flat Shell Element with Drill, Shear and Warping", International Journal for Numerical Methods in Engineering, 2016, Vol. 108, No. 10, pp.1248-1272
[33] Argyris, J. H., Balmer, H., Doltsinis, J. S., Dunne, P. C., Haase, M., Kleiber, M., Malejannakis, G. A., Mlejnek, H. P., Müller, M. and Scharpf, D. W., "Finite Element Method - the Natural Approach", Computer Methods in Applied Mechanics and Engineering, 1979, Vol. 17, pp. 1-106.
[34] Chan, S. L., "Large Deflection Kinematic Formulations for Three-dimensional Framed Structures", Computer Methods in Applied Mechanics and Engineering, 1992, Vol. 95, No. 1, pp. 17-36.
[35] Chan, S. L. and Zhou, Z. H., "Pointwise Equilibrating Polynomial Element for Nonlinear Analysis of Frames", Journal of Structural Engineering, 1994, Vol. 120, No. 6, pp. 1703-1717.
[36] Tang, Y. Q., Zhou, Z. H. and Chan, S. L., "Nonlinear Beam-column Element under Consistent Deformation", International Journal of Structural Stability and Dynamics, 2015, Vol. 15, No. 5, pp. 1450068.
[37] Chan, S. L. and Gu, J. X., "Exact Tangent Stiffness for Imperfect Beam-column Members", Journal of Structural Engineering, 2000, Vol. 126, No. 9, pp. 1094-1102.
[38] Tang, Y. Q., Y. P. Liu, and S. L. Chan. "Element-independent Pure Deformational and Co-rotational Methods for Triangular Shell Elements in Geometrically Nonlinear Analysis", International Journal of Structural Stability and Dynamics, 2017, Vol. 18, No. 5, pp. 1850065.
[39] Goldstein, H., "Classical Mechanics", Mass: Addison-Wesley, 1950
[40] Ibrahimbegovic, A., Taylor, R. L. and Wilson, E. L., "A Robust Quadrilateral Membrane Finite Element with Drilling Degrees of Freedom", International Journal for Numerical Methods in Engineering, 1990, Vol. 112, No. 11, pp. 1519-1538.
[41] Batoz, J. L. and Tahar, M. B., "Evaluation of a New Quadrilateral Thin Plate Bending Element", International Journal for Numerical Methods in Engineering, 1982, Vol. 18, No. 11, pp. 1655-1677.
[42] Tang, Y. Q., Zhou, Z. H. and Chan, S. L., "A Simplified Co-rotational Method for Quadrilateral Shell Elements in Geometrically Nonlinear Analysis", International Journal for Numerical Methods in Engineering, 2017, Vol. 15, No. 5, pp. 1450068.
[43] Chen, W. J. and Cheung, Y., "Refined Quadrilateral Element based on Mindlin/Reissner Plate Theory", Int. J. Numer. Meth. Eng., 2000, Vol. 47, No. 1-3, pp. 605-627.
[44] Jeon, H.M., Lee, Y., Lee, P. S. and Bathe, K. J., "The MITC3+ Shell Element in Geometric Nonlinear Analysis", Computers & Structures, 2015, Vol. 146, pp. 91-104.
[45] Surana, K. S., "Geometrically Nonlinear Formulation for the Curved Shell Elements", International Journal for Numerical Methods in Engineering, 1983, Vol. 19, No. 4, pp. 581-615.

SECOND ANNOUNCEMENT AND CALL FOR PAPERS

NINTH INTERNATIONAL CONFERENCE ON ADVANCES IN STEEL STRUCTURES (ICASS 2018)

5-7 December 2018 - Hong Kong, China

Jointly organised by

The Hong Kong Institute of Steel Construction
&
Department of Civil and Environmental Engineering
The Hong Kong Polytechnic University

This will be the ninth in the international conference series on Advances in Steel Structures, with the first, second, third and sixth of the conferences series held in Hong Kong, fourth in Shanghai, fifth in Singapore, seventh in Nanjing and eighth in Portugal. As with the eight previous successful conferences, this conference is intended to provide a forum for researchers and professionals to discuss and disseminate recent advances in analysis, behaviour, design and construction of steel, aluminium and composite steel-concrete structures.

Those wishing to participate in the conference are invited to submit short 200-400 word abstracts for papers related to the general topics of the conference, which are: Aluminium and Glass Structures, Analysis Method, Cold-Formed Steel, Composite Construction, Connections, Design, Experiment, Expert Systems, Fatigue and Fracture, Frames, Offshore Platforms, Performance-based Structural Design, Prefabricated Construction, Scaffolding, Seismic-resistant Structures, Stability Design, Steel, Steel Structures, Structural Health Monitoring, Structural Optimisation, Structural Stability and Sustainability. Selected papers will also be published in the International Journal of Advances in Steel Construction which carries a mission of technology transfer and is widely circulated among the engineering and building professionals.

Please use the template to prepare an abstract and send it to ICASS2018@outlook.com. Abstracts and papers will be peer-reviewed by the Scientific Committee.

香港鋼結構學會 Hong Kong Institute of Steel Construction
THE HONG KONG POLYTECHNIC UNIVERSITY 香港理工大學
DEPARTMENT OF CIVIL AND ENVIRONMENTAL ENGINEERING 土木及環境工程學系 CEE

INTERNATIONAL SCIENTIFIC COMMITTEE

F.G. Albermani (Australia)
R. Beale (UK)
F.S.K. Bijlaard (Netherlands)
R. Bjorhovde (USA)
M.A. Bradford (Australia)
D. Camotim (Portugal)
J.M. Castro (Portugal)
T.H.T. Chan (Australia)
W.F. Chen (USA)
Y.Y. Chen (China)
S.P. Chiew (Singapore)
Y.S. Choo (Singapore)
G.G. Deierlein (USA)
S.L. Dong (China)
D. Dubina (Romania)
L. Gardner (UK)
H.B. Ge (Japan)
Y. Goto (Japan)
Y.L. Guo (China)
L.H. Han (China)
G.J. Hancock (Australia)
T. Helwig (USA)
S. Herion (Germany)
B.A. Izzuddin (UK)
J.P. Jaspart (Belgium)
S.A. Jayachandran (India)
T.L. Karavasilis (UK)
S.E. Kim (Korea)
S. Kitipornchai (Australia)
K. Kwok (Australia)
D. Lam (UK)
S.S. Law (China)
W. Li (China)
G.Q. Li (China)
J.Y.R. Liew (Singapore)
D. Lignos (Switzerland)
L.R.O. de Lima (Brazil)
T.H. Lip (Australia)
E.M. Lui (USA)
Y.L. Mo (USA)
D.A. Nethercot (UK)
J.G. Nie (China)
J.A. Packer (Canada)
J.L. Peng (Taiwan)
X.D. Qian (Singapore)
K. Rasmussen (Australia)
J. Ricles (USA)
J.M. Rotter (UK)
R. Sause (USA)
P. Schaumann (Germany)
N.E. Shanmugam (Singapore)
Y.J. Shi (China)
G. Shi (China)
G.P. Shu (China)
X.P. Shu (China)
L.S.da Silva (Portugal)
N. Silvestre (Portugal)
G.S. Tong (China)
N.S. Trahair (Australia)
K.C. Tsai (Taiwan)
C.M. Uang (USA)
B. Uy (Australia)
M. Veljkovic (Netherlands)
P.C.G. da S. Vellasco (Brazil)
A. Wadee (UK)
F. Wald (Czech)
A. Walicka (Poland)
E. Walicki (Poland)
L.J. Wang (China)
W. Wang (China)
Y.C. Wang (UK)
C.M. Wang (Australia)
D. White (USA)
E. Yamaguchi (Japan)
Y.B. Yang (China)
Q.R. Yue (China)
R. Zandonini (Italy)
X.L. Zhao (Australia)
X.H. Zhou (China)
R.D. Ziemian (USA)

IMPORTANT DATES

First call for paper:	1 January 2018
Abstract submission deadline:	1 March 2018
Notification of abstract acceptance:	1 April 2018
Full paper submission:	1 June 2018
Notification of full paper acceptance:	1 August 2018
Early bird registration:	on or before 1 September 2018
Announcement of programme:	1 October 2018

REGISTRATION FEE

The conference registration fee is US$750 (Early bird registration before 1st September 2018)/US$850, which covers conference proceedings, conference banquet, lunches and refreshments.

OFFICIAL LANGUAGE

English will be the official language of the Conference for both oral and written presentations.

PROCEEDINGS

The proceedings of the conference will be published by the Hong Kong Institute of Steel Construction.

ORGANISING COMMITTEE

Siu-Lai Chan (Chair) Tak-Ming Chan (Co-Chair) Songye Zhu (Co-Chair)
Yaopeng Liu Siwei Liu

LOCAL SCIENTIFIC COMMITTEE

Francis.T.K. Au	Goman.W.M. Ho	Y.Q. Ni	A.S. Usmani
C.M. Chan	Eddie S.S. Lam	S.J. Pan	Y. Xia
W.T. Chan	Paul H.F. Lam	Derek K.L. So	Jackie Yau
Edward S.C. Chan	C.K. Lau	Andrew K.W. So	Ben Young
W.K. Chow	Andy Lee	Ray K.L. Su	W.K. Dominic Yu
Reuben Chu	Y.S. Liu	J.G. Teng	S.W. Yuen
J.G. Dai	S.H. Lo	Ben Tse	Z.H. Zhou

SUPPORTING INSTITUTIONS

ASCE HONG KONG SECTION
HKIE THE HONG KONG INSTITUTION OF ENGINEERS 香港工程師學會 — Civil, Fire and Structural Divisions
RCATISE Research Centre for Advanced Technology in Structural Engineering, The Hong Kong Polytechnic University

SUPPORTING JOURNAL

ADVANCED STEEL CONSTRUCTION an international journal

ORGANIZING PARTNER

NIDA®

For further information, please contact:
Carol Deng - Conference Secretary
E-mail: icass2018@outlook.com
Address: International Journal of Advanced Steel Construction, CEE, The Hong Kong Polytechnic University, Hong Kong, China.

CONFERENCE WEBSITE:
http://www.icass2018.com

ORDER FORM

ISSN 1816-112X

Advanced Steel Construction, an international journal

Indexed by the Science Citation Index Expanded, Materials Science Citation Index and ISI Alerting Services

From: _____

To: ***Secretariat, Advanced Steel Construction, an international journal***
Fax: (852) 2334-6389

I/ We would like to enter a subscription to the ***International Journal of Advanced Steel Construction (IJASC)*** *published by The Hong Kong Institute of Steel Construction.*

Please complete the form and send to:

International Journal of Advanced Steel Construction
c/o Department of Civil and Environmental Engineering
The Hong Kong Polytechnic University
Hunghom, Kowloon, Hong Kong

Fax: (852) 2334-6389 Email: ceslchan@polyu.edu.hk

Published by : The Hong Kong Institute of Steel Construction
Website: http://www.hkisc.org/

Please tick the appropriate box

- ❑ Please enter my hard-copy subscription **(4 issues per year)**.
- ❑ Please send me a complimentary copy of the *Advanced Steel Construction, an International Journal (IJASC).*

Please tick the appropriate box(es)

	Print	**On-line is free**
Personal	❑ US$ 125	
Institutional	❑ US$ 280	

Total Amount **US$** _____

Methods of payment *(please tick the appropriate box(es))*

- ❑ Please invoice me
- ❑ Cheque enclosed for US$ _____ payable to Hong Kong Institute of Steel Construction Limited (No personal cheque accepted)

Ship to

Name (Prof./ Dr./ Mr./ Ms.) _____
Address _____
_____
_____
City/ State/ Postal Code _____
Country _____
Email _____ Fax _____